INSTRUMENTED BUILD PLATE FOR IN-SITU STRESS MONITORING AND CRACK DETECTION DURING THE LASER POWDER BED FUSION ADDITIVE MANUFACTURING PROCESS

by

Samuel Ludwig

A thesis submitted to the faculty of
The University of North Carolina at Charlotte
in partial fulfillment of the requirements
for the degree of Master of Science in
Mechanical Engineering

Charlotte

2020

Approved by:

_____
Dr. Chris Evans

_____
Dr. Angela Davies

_____
Dr. Harish Cherukuri

ABSTRACT

SAMUEL LUDWIG. Instrumented Build Plate for In-situ Stress Monitoring and Crack Detection During the Laser Powder Bed Fusion Additive Manufacturing Process. (Under the direction of DR. CHRIS EVANS)

The goal of this project is to develop a new method of in-situ monitoring of the laser powder bed fusion (LPBF) additive manufacturing (AM) process. An instrumented build plate was designed, fabricated and installed in the NIST Additive Manufacturing Metrology Testbed (AMMT). An ultrasonic sensor attached to the bottom of the build plate detects acoustic emissions (AE) while the laser beam is scanning across the powder bed. Initial experiments with single powder layers showed a clear distinction in the RMS of the AE signal between environmental noise, the laser actively scanning and cracking events. Due to excessive cracking across the entire process map however, a build plate heater was incorporated along with a tilting mechanism for better powder spreading. Subsequent heated and unheated experiments showed no cracking at all, which is attributed to differences in powder composition. A thermal camera, coaxial with the laser beam, captured images of the laser melt pool in-situ. Another optical camera was used post-process to image powder denudation. Bolts with embedded strain sensors constrain the build plate and were intended to monitor the amount of residual stress as a 3D part is manufactured. Preliminary frequency-domain analysis of AE signals was carried out, leading to recommendations for future investigation.

ACKNOWLEDGEMENTS

I am grateful to my advisor Chris Evans for his continuing guidance and support. Many thanks to my committee members Angela Davies and Harish Cherukuri, as well as John Ziegert and Stuart Smith for their advice. I appreciate the support provided by Brian Dutterer, Joe Dalton and many other faculty members at UNCC.

I would like to thank Alkan Donmez for hosting me at NIST, Brandon Lane for providing invaluable support and guidance, Steve Fick and Eric Whitenton for sharing their expertise and many other NIST researchers for their contributions.

I’m thankful for the assistance and input from my fellow grad students at UNCC.

TABLE OF CONTENTS

LIST OF TABLES

LIST OF FIGURES

LIST OF ABBREVIATIONS

AM	additive manufacturing
AMMT	additive manufacturing metrology testbed
CMOS	complementary metal-oxide-semiconductor
CTE	coefficient of thermal expansion
FBG	fiber Bragg grating
LPBF	laser powder bed fusion
MARSE	measured area of the rectified signal envelope
MHL	message handler loop
NIR	near infrared
NIST	National Institute of Standards and Technology
P/V	power/velocity
PSD	power spectral density
SAM	Simple AM
SCFH	standard cubic feet per hour
SWLI	scanning white light interferometer
Ti64	Titanium alloy Ti-6Al-4V
UI	user interface
QMH	queued message handler

CHAPTER 1: INTRODUCTION

The goal of this project is to develop a new method of in-situ monitoring of the laser powder bed fusion (LPBF) metal additive manufacturing (AM) process. Metal powder bed fusion has been reviewed in detail, including the various types and sources of defects that can occur during the LPBF process (Grasso and Colosimo 2017). As subsequent layers of metal powder are fused by laser-melting and re-solidification, large thermal gradients are present in the cooling metal. Recently melted metal shrinks in volume as it cools, resulting in residual stress throughout the part as well as in the build plate it is attached to (Mercelis and Kruth 2006). One type of defect is cracks that can form due to the rapid cooling rate as soon as the laser has passed (Harrison, Todd, and Mumtaz 2015).

Acoustic emissions (AE) from the LPBF process have not been studied extensively but some measurement approaches include microphones (Kouprianoff et al. 2017), acoustic spectroscopy (Smith et al. 2016) and fiber Bragg grating sensors (Wasmer et al. 2018). Only a few studies i.e. (Eschner et al. 2018) involve mounting a piezoelectric ultrasonic transducer to the bottom of the build platform and General Electric has been awarded patents for this method (Gold and Spears 2017) but has not yet commercialized it. However, the piezoelectric sensor itself is a mature technology, instrumentation is widely available and crack detection with this method as well as time- and frequency-domain analysis techniques have been well-documented.

In this work, instrumented bolts constraining the build plate will be used to monitor the residual stress and an ultrasonic piezoelectric sensor will be used to record acoustic emissions due to crack formation. Instead of supplying energy to the object

under examination, non-destructive AE testing listens for energy released by the object, as demonstrated in FIGURE 1. First, there is a redistribution of stress due to changes in external load, pressure or temperature. Second, an internal source such as a crack initiating or growing releases energy in the form of acoustic waves. Third, the spherical acoustic waves propagate outward through the bulk material to the surface where the AE sensor detects them.

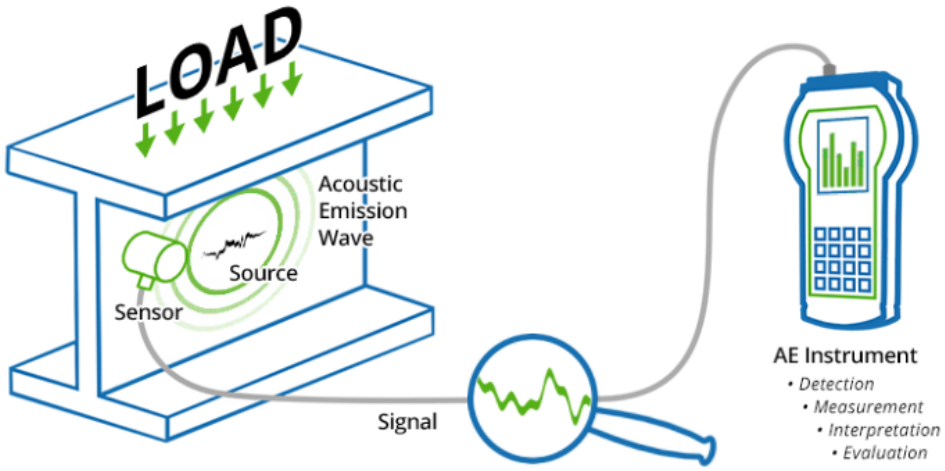

FIGURE 1: Acoustic emission source and acquisition chain (MISTRAS Group n.d.).

Once the AE signal is being acquired it can be processed in many ways due to its multiple features, shown in FIGURE 2. A common method for commercial software is to apply a threshold and count “hits”, or threshold crossings, to quantify the number of AE events. Often, multiple parameters are combined to provide better information about the shape of the signal, such as the Measured Area of the Rectified Signal Envelope (MARSE).

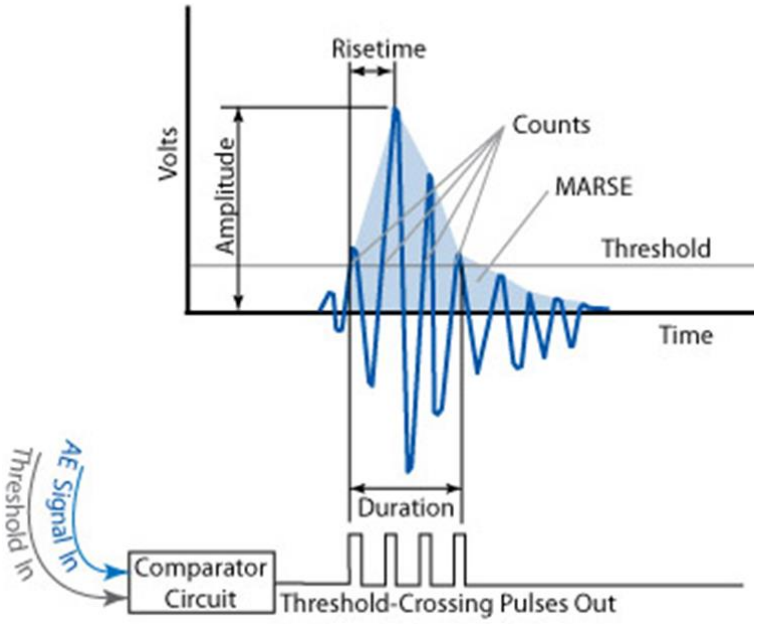

FIGURE 2: AE signal features for analysis (Iowa State University 2001).

As shown in FIGURE 3, a literature review revealed a range of sensor bandwidths used to detect acoustic emissions from cracking or other sources, often during welding. Acoustic emission sensors for use in this work were evaluated based on their availability, required operating conditions, noise levels and bandwidths.

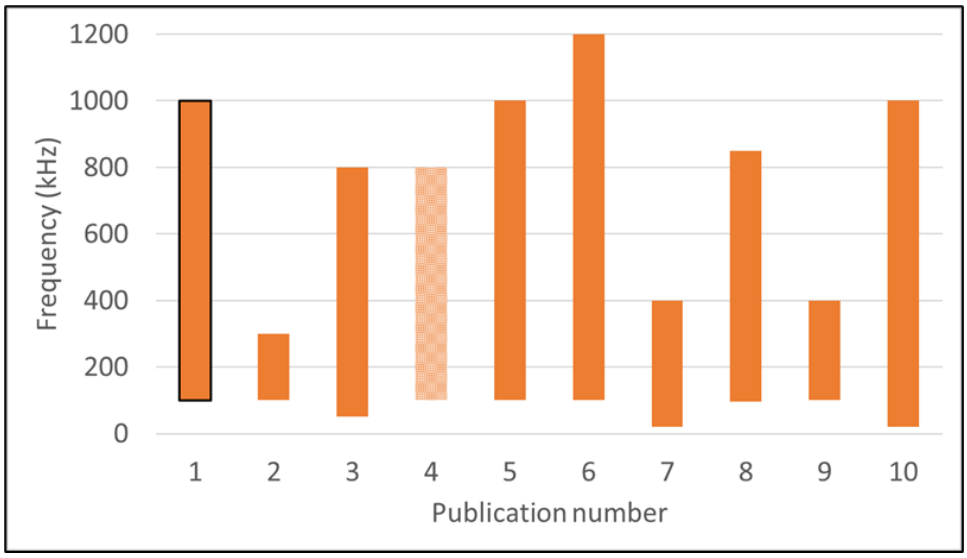

FIGURE 3: Range of sensor bandwidths for various AE experiments.

TABLE 1: Publications containing the information presented in FIGURE 3.

Publication	Description	Author
1	Acoustic emission monitoring during continuous welding	ASTM E749-96
2	Acoustic emission testing guide for metallic objects	Vallen Systeme
3	Crack propagation in 7075 Aluminum	Kordatos, 2011
4*	Crack propagation in additively manufactured Ti64	Stranza, 2017
5	Acoustic emissions in laser processing	Li, 2002
6	Crack propagation in steel and welded steel	Roberts, 2002
7	AE source localization in aluminum plates	Ebrahimkhanlou, 2017
8	AE monitoring during sheet steel forming	Behrens, 2017
9	Crack growth in 316 stainless steel and welds	Chai, 2017
10	Stress corrosion cracking in 304 stainless steel	Kovac, 2015

A differential acoustic sensor with a bandwidth of 100-900 kHz was chosen to detect the acoustic emission signals along with an oscilloscope module to acquire and process these signals, taking advantage of its digitizer's high sampling rate, bandwidth and data streaming rate along with its customizable FPGA for high-speed calculations. For residual stress measurements, two bolts with embedded fiber optic strain sensors were selected due to the sensors' immunity to electromagnetic interference. Two more bolts with embedded traditional foil strain gages were chosen so the performance of the two types of strain sensors can be compared.

A custom instrumentation rig was fabricated from stainless steel to be compatible with the NIST Additive Manufacturing Metrology Testbed (AMMT) (B Lane et al. 2016) located on NIST's campus in Gaithersburg, MD, which is the site of our experimental work. Each build plate is 150 mm wide x 250 mm long x 25.4 mm thick and is made of nominally the same material as the powder used in the AM process to keep the acoustic impedance consistent from the ultrasonic sensor face on the bottom of the build plate to the highest layer on top of the plate.

Chapter 2 of this work discusses the considerations that guided the selection and testing of sensors and electronics, the physical constraints imposed by the AMMT and the first design iterations of the instrumented build plate and the data acquisition software.

Chapter 3 discusses the design of and results from the first round of experiments conducted at NIST during the summer of 2018. These results inspired several modifications to the build plate and data acquisition software, described in Chapter 4. Multiple subsequent experiments discussed in Chapter 5 were conducted in the summer of 2019 using a new batch of Ti64 powder. Chapter 6 summarizes findings, discusses preliminary analysis work and presents multiple recommendations for future experiments and investigations.

CHAPTER 2: DESIGN AND FABRICATION

2.1 Instrumentation selection

The Physical Acoustics WD sensor was selected for its noise-reducing differential operating mode (Apogee Instruments Inc 2019), its high-temperature operating capability and its bandwidth of 100-900 kHz to detect a broad range of acoustic emissions. A Rigol DP712 power supply provides the Physical Acoustics 2/4/6 C pre-amplifier for the AE sensor with the required power. Per vendor recommendation[1], Permatex Blue RTV (Permatex 2018) was used initially as a couplant between the sensor and build plate, later changed to liquid glycerin for ease of removal and finally Magnaflux Sono 600 (Magnaflux 2018) for high-temperature operation.

To detect residual stress in the build plate, and therefore in the AM part, all four bolts constraining the build plate are instrumented. Two fiber optic Brainy Bolt™ inserts with Fiber Bragg gratings (FBGs) from Cleveland Electric Labs were selected due to the sensors' immunity to electromagnetic interference (Cleveland Electric Laboratories, n.d.) and ease of installation. Two more ½" bolts with embedded foil strain gages from Strainsert were selected to compare performance of the two types of sensors, shown in FIGURE 4. Both types of sensors have built-in temperature compensation, and all four bolts will be threaded into the underside of the build plate to prevent the wires attached to the bolt heads from interfering with the recoater blade.

[1] David Sinay, Physical Acoustics Corporation, david.sinay@mistrasgroup.com

FIGURE 4: Bolts with FBG (left) and foil strain gage (right). (Cleveland Electric Laboratories, n.d.) and (Strainsert, n.d.)

All data collected from the sensors is acquired using National Instruments (NI) equipment with custom LabVIEW programs. The NI PXIe-5170 4-channel oscilloscope module was chosen to acquire and eventually pre-process the acoustic emission signals because of its high sampling rate, bandwidth and data streaming rate along with its FPGA for high-speed calculations. The PXIe-6361 multi-I/O module was chosen to acquire signals from the foil-gaged bolts, communicate with the RTD chips and control the heater. Both previously listed modules are installed in a PXIe-1082 chassis fitted with a PXIe-8840 controller running Windows 7 and LabVIEW 2017. In addition, the PXIe-4844 fiber optic interrogator module was selected for acquiring signals from the Brainy Bolts™ during future 3D builds.

2.2 Initial testing

Because only an estimate of the build plate dimensions was known at this point, a mockup build plate was machined from stainless steel for mounting and testing of the sensors. An aluminum frame, shown in FIGURE 5, was assembled to allow access to the bottom of the plate and placed on rubber damping pads for external vibration isolation.

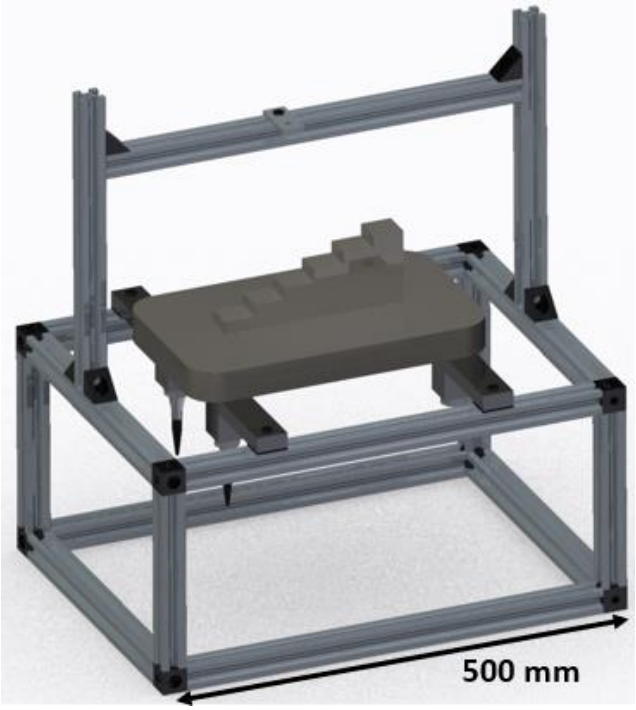

FIGURE 5: AE testing frame with build plate mockup.

The AE sensor was mounted to the underside of the plate using Permatex Blue RTV as both adhesive and couplant. The sensor response was tested by performing Hsu-Nielsen pencil-lead break (PLB) tests on the plate in accordance with the ASTM E976-99 standard (ASTM 1999). A step structure, shown in FIGURE 6, was attached to the top of the plate to allow PLBs and metal ball impacts to be performed at different effective plate thicknesses.

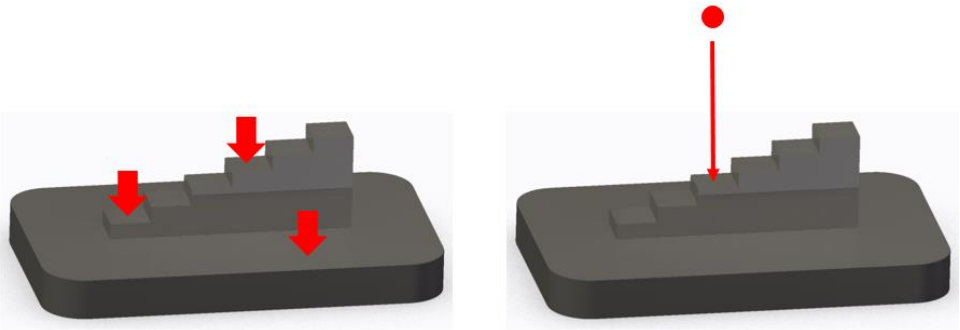

FIGURE 6: Example test locations for PLB (left) and ball impact (right).

PLBs and ball impacts were first performed without the step structure but at increasing distances from the center of the plate where the AE sensor was mounted. FIGURE 7 and FIGURE 8 show examples of the sensor response to AE generated directly above the sensor, with the energy of the acoustic event, estimated as the MARSE, represented by the shaded area in the figures. The MARSE is calculated using trapezoidal approximation from the beginning of the signal to the point where the envelope crosses a threshold that is 5% of the maximum amplitude. Note that the initial amplitude of the ball impact response is several times higher than that of the PLB.

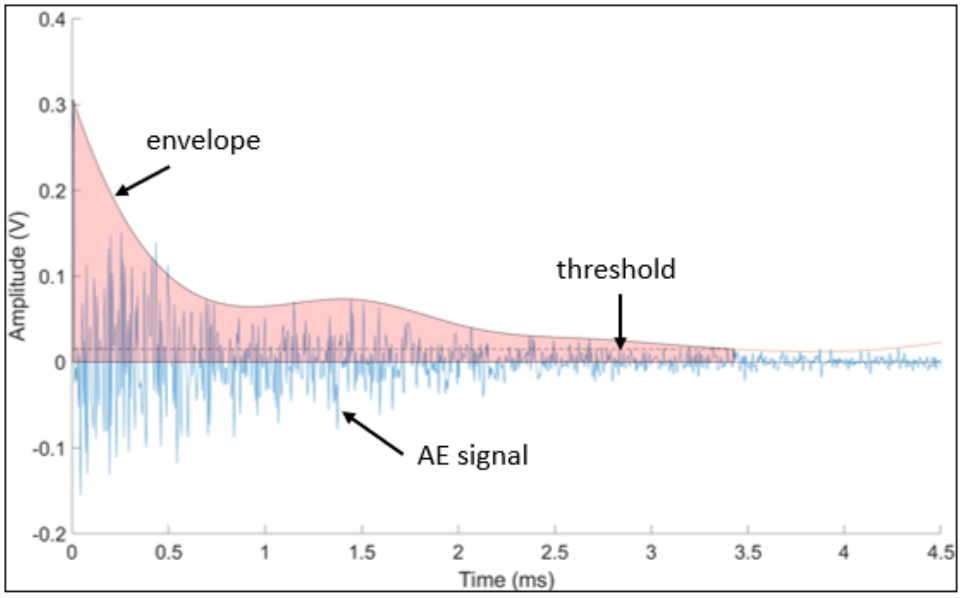

FIGURE 7: AE sensor response to PLB.

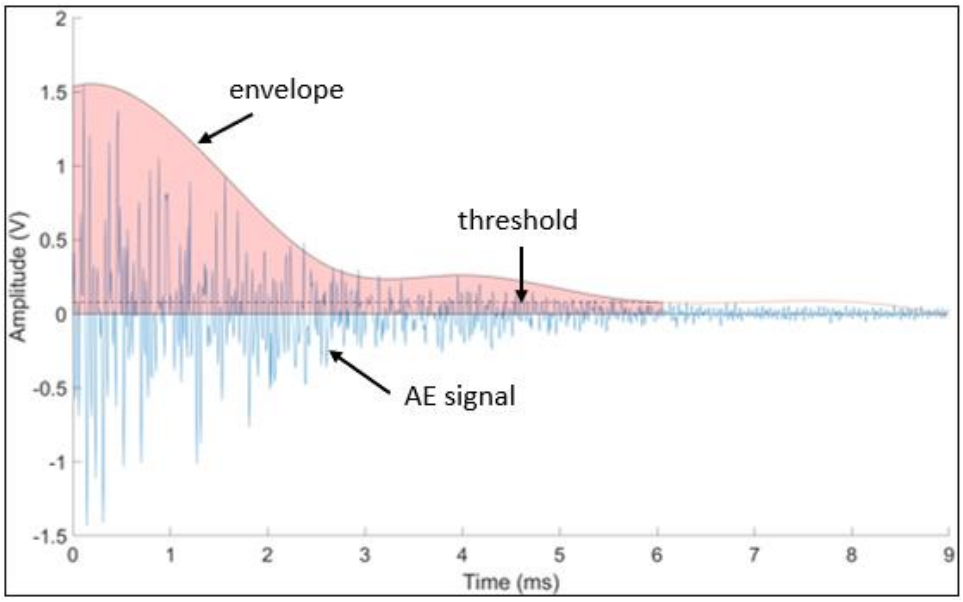

FIGURE 8: AE sensor response to steel ball impact.

Three PLBs at each location on top of the plate were averaged, and a slight decrease in both max amplitude and RMS of the AE signal as distance from the sensor increases is shown in FIGURE 9. From this data, a loss of 0.14% per mm distance from the AE sensor can be expected in the RMS. While this loss may need to be taken into consideration, the time delay of about 0.2 μs per mm in stainless steel is negligible and does not require shifting AE signals from different locations on the build plate.

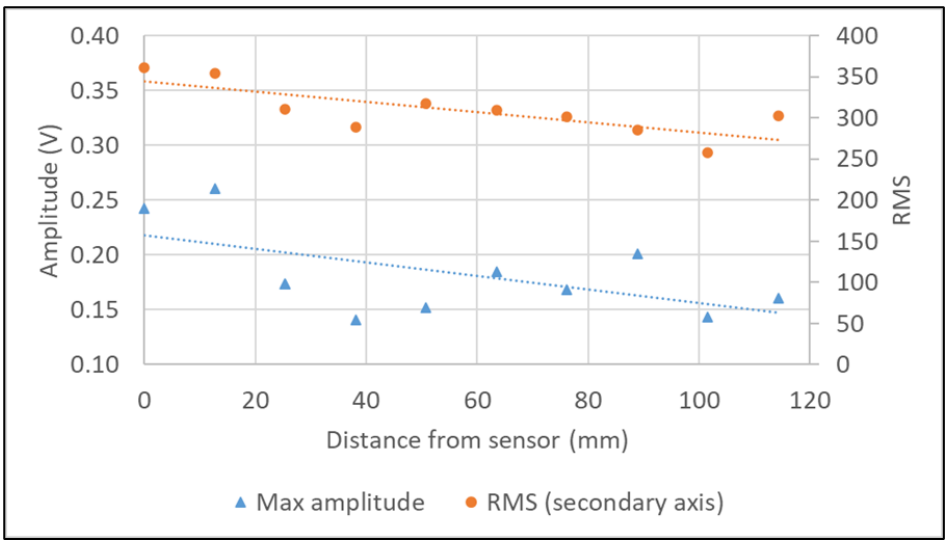

FIGURE 9: Characteristics of sensor response to PLBs on top of the build plate.

An adjustable tab with a small hole attached to the top of the frame in FIGURE 5: AE testing frame with build plate mockup. makes the free-falling 8-mm-diameter steel ball's impacts more repeatable. The theoretical energy of the impacts can be calculated based on known drop heights using the well-known gravitational potential energy equation, which is *mass* x *acceleration due to gravity* x *height*. The ball's theoretical impact energy can then be compared to the energy calculated from AE data using the MARSE. Theoretical energy values in Joules were calculated for the steel ball falling from 250, 150 and 50 mm. Three ball impacts were averaged after being carried out at selected locations and heights. The same slightly decreasing trend from the PLBs can be seen in FIGURE 10, especially for h = 250.

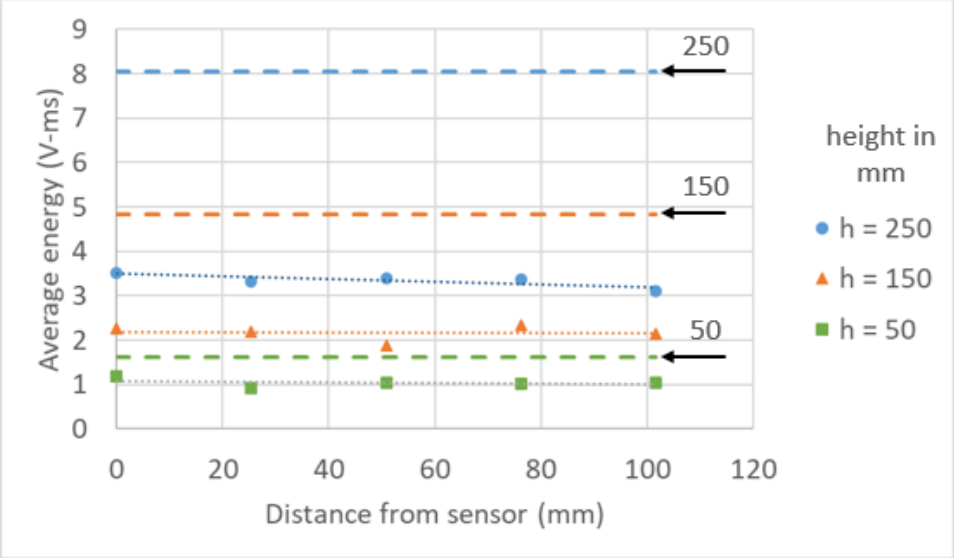

FIGURE 10: Experimental and theoretical (dashed lines) energy of ball impacts.

Deviation of experimental from theoretical values, denoted by dotted lines, increases with drop height. The deviations indicate losses due to attenuation, but these initial tests demonstrated that the AE measurement setup is sufficiently sensitive to AE sources through a 1" thick build plate.

2.3 Mechanical design

The number one requirement for any integrated sensor configuration is full compatibility with the AMMT, the custom-built laser powder bed fusion metal additive manufacturing machine shown in FIGURE 11 and owned by NIST.

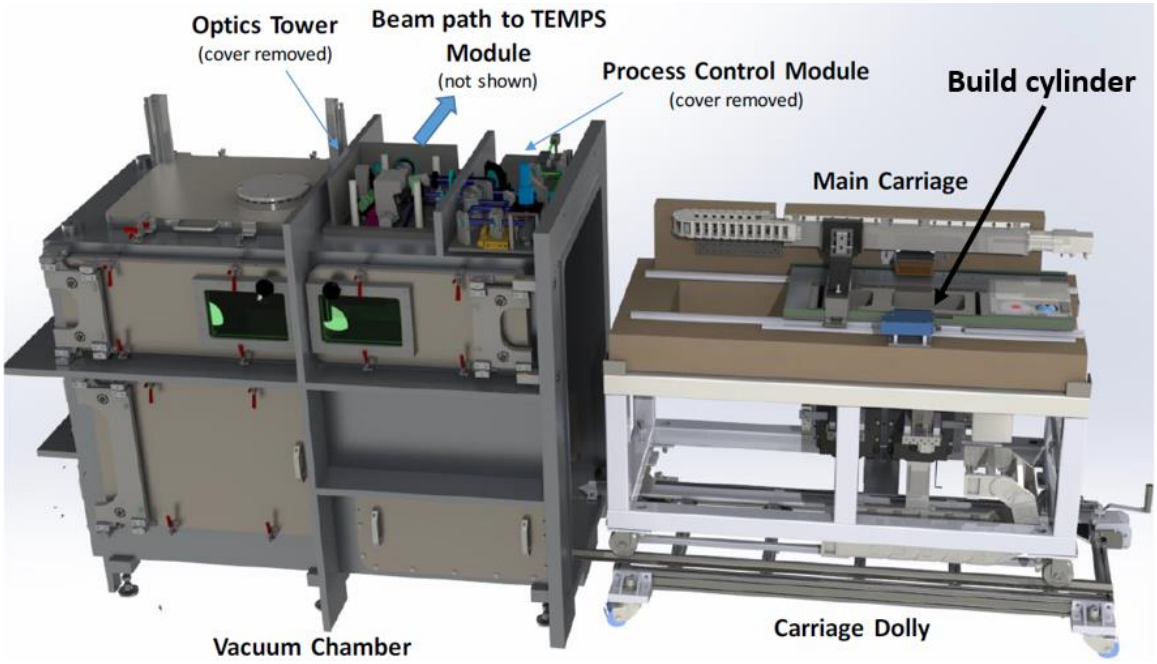

FIGURE 11: Solid model assembly of the AMMT with the main carriage removed from the vacuum chamber to show build cylinder location (B Lane et al. 2016).

The AMMT was first assessed in CAD and in-person to explore suitable design concepts. Immediate limitations included the size of the build plate (150 x 250 mm), depth of the build cylinder (~200 mm), availability of cable feedthroughs and the need for vacuum-rated hardware. In addition, the existing recoater blade seen in FIGURE 12a can only be raised and lowered about 10 millimeters, and the motion stage to which the build stack is attached has a vertical travel range limited to 200 mm.

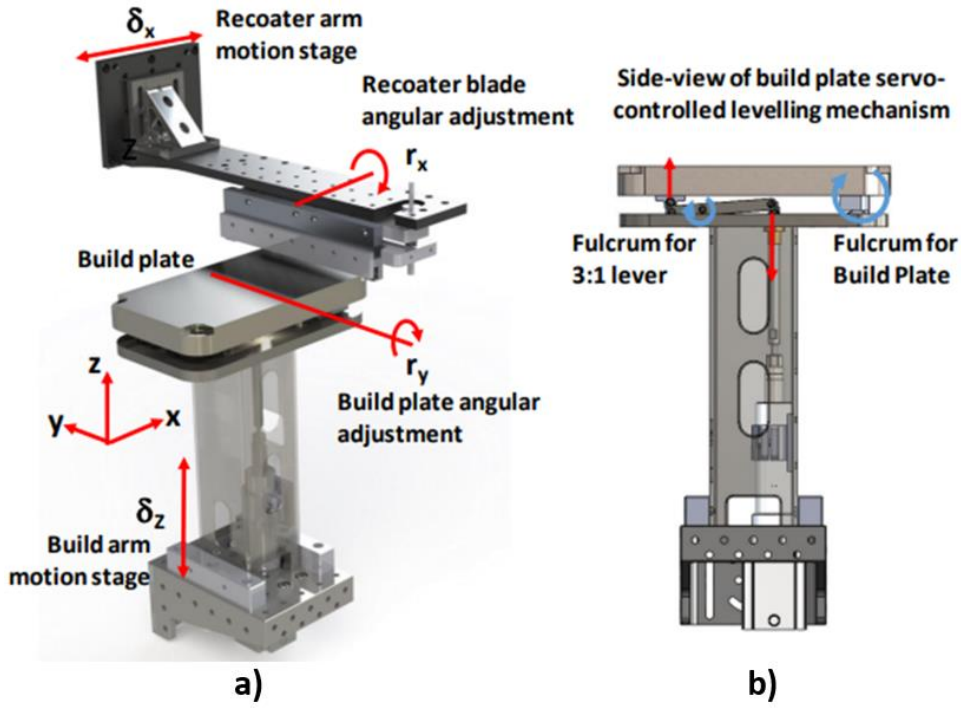

FIGURE 12: Details of the original build stack in the AMMT (B Lane et al. 2016).

The design of the instrumentation rig was inspired by an instrumentation "vault" (Dunbar et al. 2016) built to keep measurement equipment from becoming contaminated with metal powder. FIGURE 13a demonstrates the need to install the instrumented bolts from the bottom of the build plate to keep the top surface clear for the recoater blade. FIGURE 13b shows how the bolts could interfere with the leveling mechanism, and the final enclosed vault or rig concept to protect the sensors and allow cable management can be seen in FIGURE 13c.

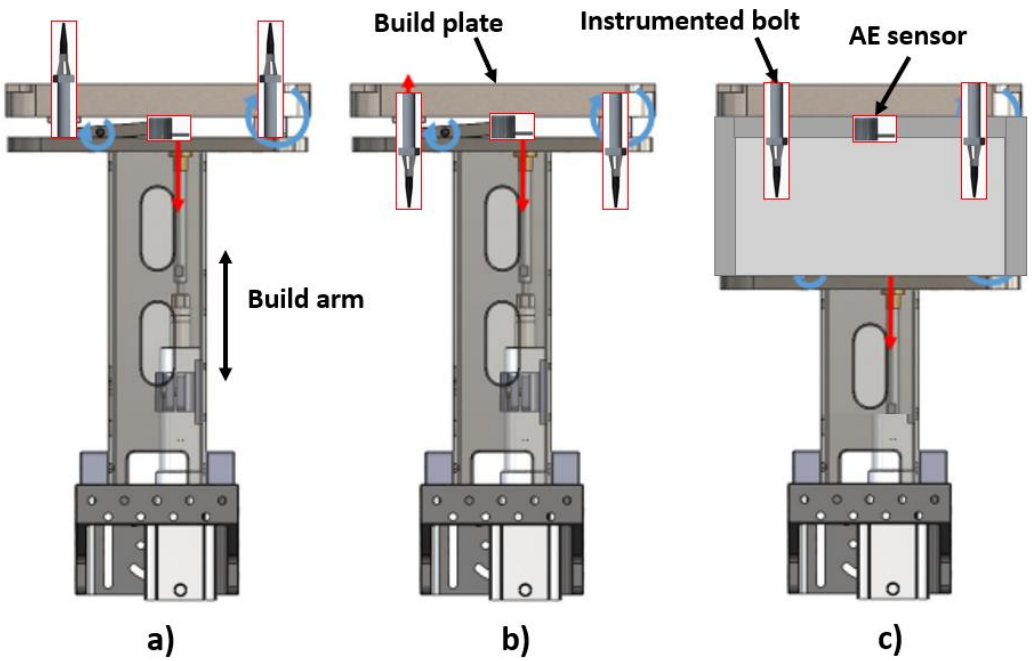

FIGURE 13: Possible sensor configurations overlaid on original build stack.

Not shown in the original build stack in FIGURE 13 are two components that were added to the AMMT later during its development, including a seal assembly to keep powder from falling down the build cylinder and a heater installed underneath the build plate. To build the instrumentation rig shown in FIGURE 14, the original felt seal assembly was replicated, then modified to accommodate instrumented bolts and AE sensor installation from the bottom. The intent was to use the original heater with ceramic insulating plate, but it was completely removed because it could not be modified and occupied too much vertical space.

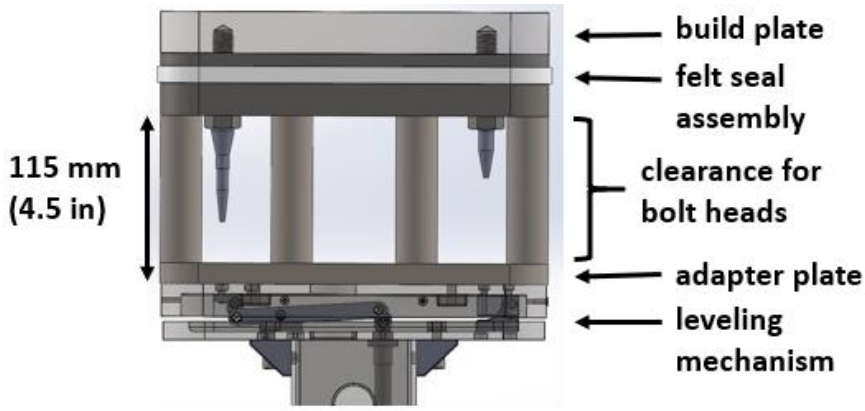

FIGURE 14: Side view of instrumentation rig attached to original leveling mechanism.

The first version of the instrumentation rig is shown in FIGURE 15 without the build plate, and with the seal assembly and plastic dust shroud made transparent to reveal the locations of the AE sensor and instrumented bolts.

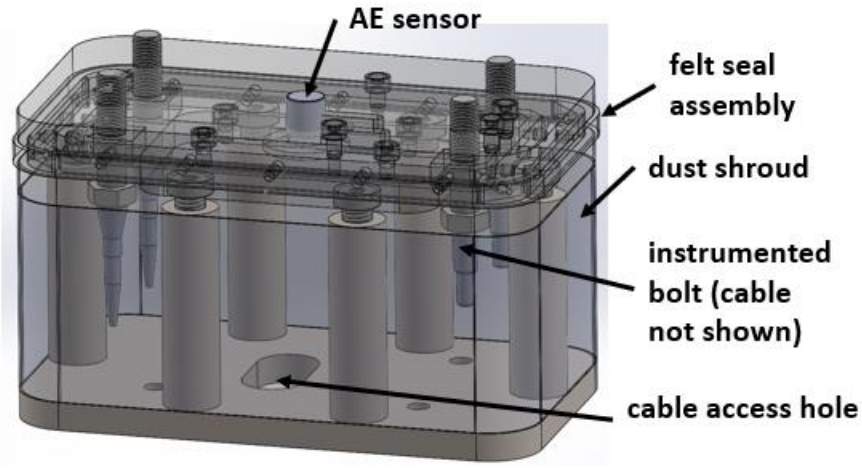

FIGURE 15: Solid model of instrumentation rig v1 (build plate not visible).

The AE sensor is pressed against the bottom of the build plate by a spring against its back side designed to apply a force at least that of commercially available magnetic sensor holders (Vallen 2006). The instrumented bolts are threaded into the bottom of the build plate and all cables are routed through the access hole, down the build arm and are then connected to the data acquisition hardware via feedthroughs in the walls of the AMMT vacuum chamber.

For early experiments requiring only a single layer of powder and a smaller build area, a second build plate, shown in FIGURE 16, was designed to accept smaller 4” x 4” substrates that are attached top-down for easy removal.

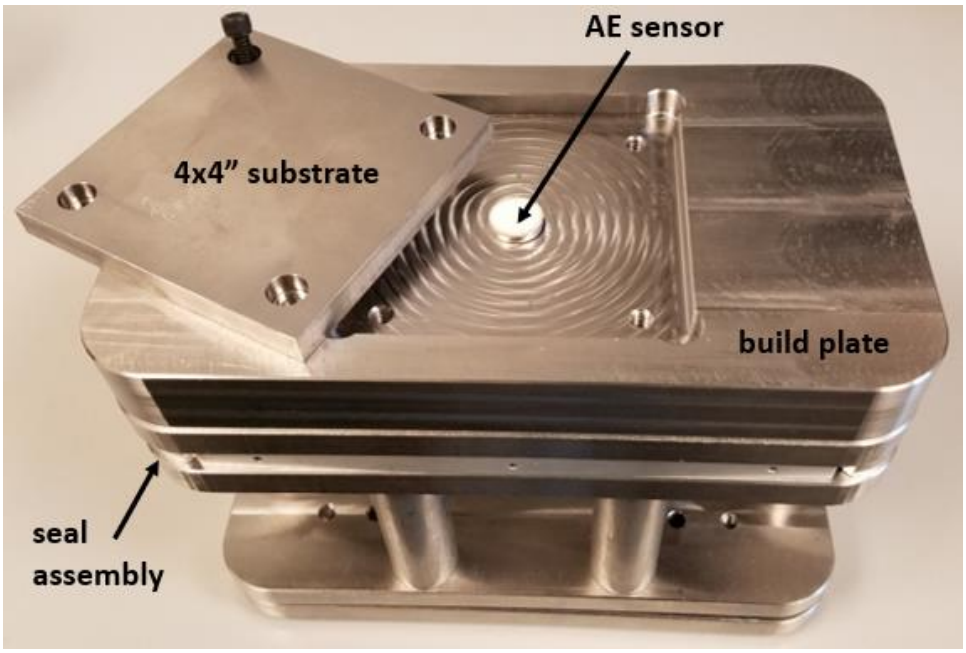

FIGURE 16: Instrumentation rig with top-mounted removable substrate.

This configuration allows multiple experiments to be performed sequentially by swapping out substrates quickly without the need to replace or regrind an entire solid build plate. Counterbored screw holes on the substrate prevent interference with the powder recoater blade. The AE sensor was moved upwards into the build plate to contact the bottom of the substrate directly and for easy couplant reapplication.

2.4 Fabrication

Most of the components in the instrumentation rig are made from 304 stainless steel. This material was chosen because structural rigidity is needed to make consistent strain measurements. Additionally, stainless steel is resistant to corrosion from cleaning products and threads are not easily damaged during repeated assembly and disassembly. Since experimental results need to be analyzed before designing the next experiment and

access to the AMMT is in high demand, the rig was assembled and installed in the AMMT, then uninstalled, disassembled and thoroughly cleaned after each experiment. Except for the leveling mechanism and bolts, all components shown in FIGURE 14 were fabricated according to TABLE 2.

TABLE 2: Instrumentation rig component fabrication.

Component	Method	Material
Build plates	3-axis CNC mill	304, 17-4 PH, 316L
Top seal plate	3-axis CNC mill	304 stainless steel
Center seal plate	4-axis CNC machining center	6061 aluminum
Seal spring plates	4-axis CNC machining center	6061 aluminum
Bottom seal plate	3-axis CNC mill	304 stainless steel
Adapter plate	3-axis CNC mill	304 stainless steel
Vault pillars	Manual lathe	304 stainless steel
AE sensor cover	3-axis CNC mill	6061 aluminum
Vault enclosure	Manual cutting	CPVC
Felt seal	Provided by NIST	felt

Aluminum was chosen for the center seal plate due to its complex geometry, shown in FIGURE 17. This component is necessary to press the felt seal around the rig against the walls of the build cylinder to prevent metal powder from falling into the bottom of the machine. With the help of UNCC machinists, the existing NIST design was duplicated and modified to allow the AE sensor to contact the bottom of the build plate.

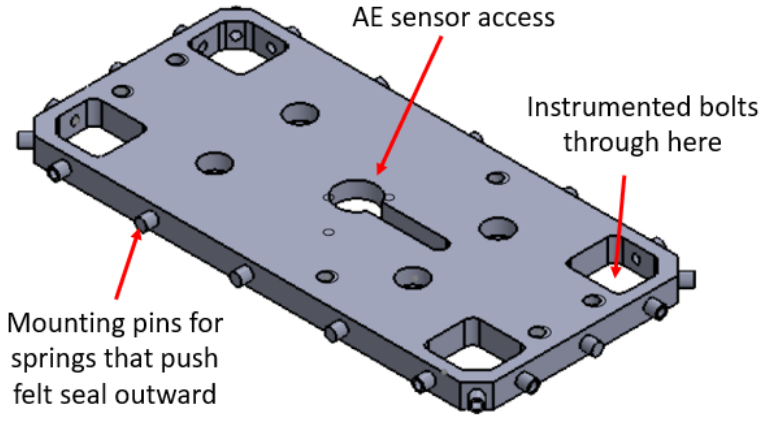

FIGURE 17: CAD model of modified center seal plate (3.6” x 7.6”).

2.5 Software

The most expedient way to acquire data from any NI instrument is to understand and then modify an existing LabVIEW program. Due to the AMMT's scheduling limitations and time constraints, the "niScope EX Save to File - HWS Low Level - Single Channel Stream" VI was chosen for its simpler "one-shot" method of data acquisition. This VI was modified to record data from two oscilloscope channels simultaneously at 10 MHz for a predetermined amount of time. Acquisition time is limited by the oscilloscope's 750 MB onboard memory to 12 seconds of continuous recording, but this seemed to be sufficient for simple single-layer experiments which were predicted to last from 0.5 to 7 seconds per set of tracks or pads.

Acquisition is triggered by monitoring the AMMT's laser trigger signal. This signal is routed from the AMMT's controller to one of the oscilloscope channels where it is monitored and recorded to synchronize with the AE dataset. When the laser trigger activates the laser for the first time at the beginning of the first track, acquisition on both oscilloscope channels is immediately started for the predetermined amount of time. Additionally, the AMMT's controller records actual laser position from the encoders attached to the actuators moving the mirrors that direct the laser beam. Laser power is also recorded by the AMMT's controller at the same 100 kHz rate. FIGURE 18 shows where the recorded data originates along with future data acquisition capabilities.

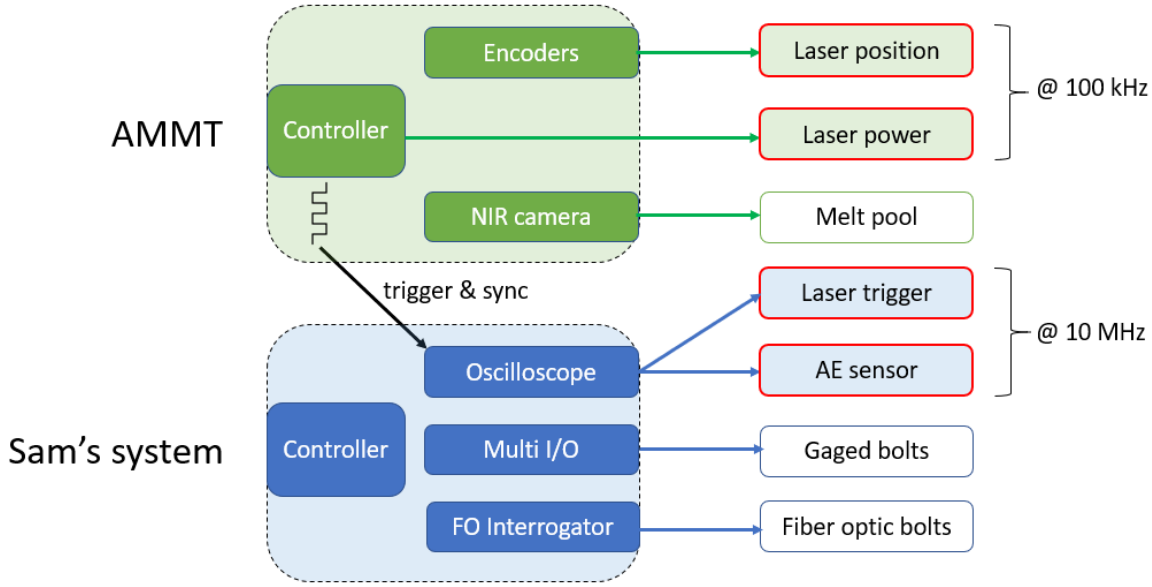

FIGURE 18: Data acquisition diagram (recorded data types outlined in red).

Manually creating code for the laser scan path consists of several steps. After a scan pattern is chosen, G-code for x- and y-positioning is written line by line in Excel, with the desired laser power and scan speed in the last two columns. This file is processed in the custom NIST-developed Simple AM (SAM) software (Yeung et al. 2018) along with a parameter file that determines settings like laser modes and trigger behavior. The SAM software outputs an instruction file compatible with the AMMT software which is then converted one more time into lower-level code for the FPGA-based AMMT controller. Files containing code processed in this way have a size limit, so the chosen scan pattern was often broken into smaller pieces for the single-layer experiments.

CHAPTER 3: INITIAL EXPERIMENTS (2018)

3.1 Preparation

The entire original build stack in the AMMT was removed, including the leveling mechanism due to the weight of the instrumentation rig. The rig was installed directly on top of the build arm and leveled using plastic shims. Since 3D builds are not planned until later, only the AE sensor was installed in the rig, with generic Grade 5 bolts replacing the instrumented bolts for ease of assembly. The face of the spring-loaded AE sensor was cleaned and two drops of glycerin couplant were applied each time a new substrate was installed.

The laser beam's D4σ diameter, also referred to as spot size in this work, was adjusted to be nominally 85 μm at the top surface of the substrate. This is achieved by first moving the build stack vertically until the top surface of the substrate coincides with a predefined focal plane. To accomplish this, the previously calibrated Keyence laser displacement sensor measures the vertical position of the middle of the substrate from above. Spot size can then be adjusted by moving the build stack to the corresponding vertical position given by the calibration curve. The D4σ diameter is calculated from the second moment of the beam profile and is four times the standard deviation of the distribution of intensity along the major and minor axis of the beam. (Thériault 2018) This parameter is commonly used to define laser beam diameter and is recommended by ISO 11146-1:2005.

3.2 Preliminary scans

To test the instrumentation setup and data acquisition software, a NIST-designed scan pattern was chosen for preliminary single-layer experiments. This pattern, shown in

FIGURE 19, allows laser scan performance to be evaluated in both axes together and separately, across most of the 100 x 100 mm substrate's available area.

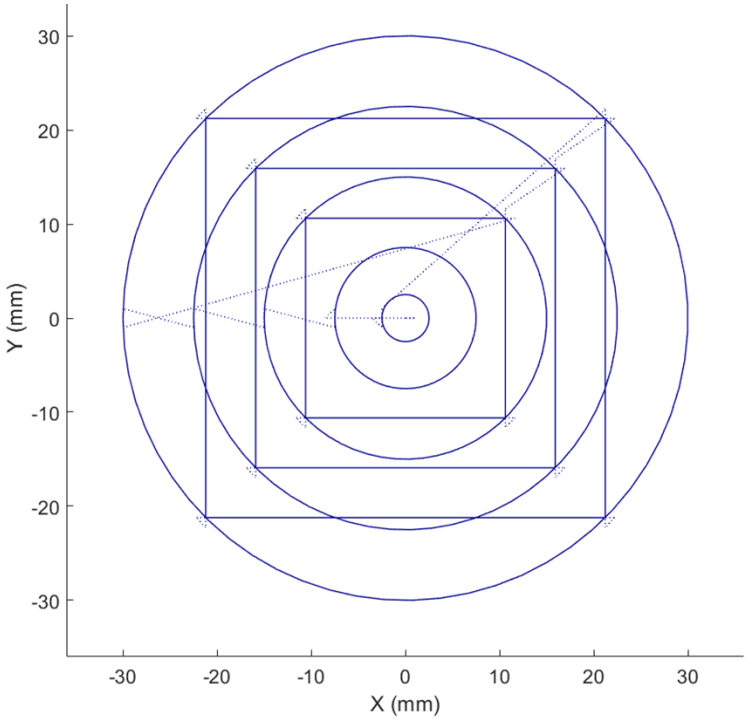

FIGURE 19: Preliminary scan pattern.

Two powder batches contained 17-4 stainless steel and Ti64 with 5% Cu, the latter of which was chosen for its high cracking susceptibility (Yadroitsev et al. 2010). The three types of substrate materials are 316L stainless steel, 17-4 stainless steel and Ti64, the latter two to match the powder as closely as possible. The scan pattern was first run on bare substrates, then with single layers of the powders listed above. Before running the laser scans, a plexiglass enclosure with interior dimensions of about 300 x 300 x 400 mm was placed over the build plate and filled with argon gas to prevent oxidization during laser melting.

According to the scan code for this pattern, the four outer circles are scanned first, followed by the squares from smallest to largest, and finally the smallest circle. After overlaying the RMS of the recorded AE data on the laser power and position data as

shown in FIGURE 20, distinct peaks can be seen when the laser turns off at the end of each circle or straight line.

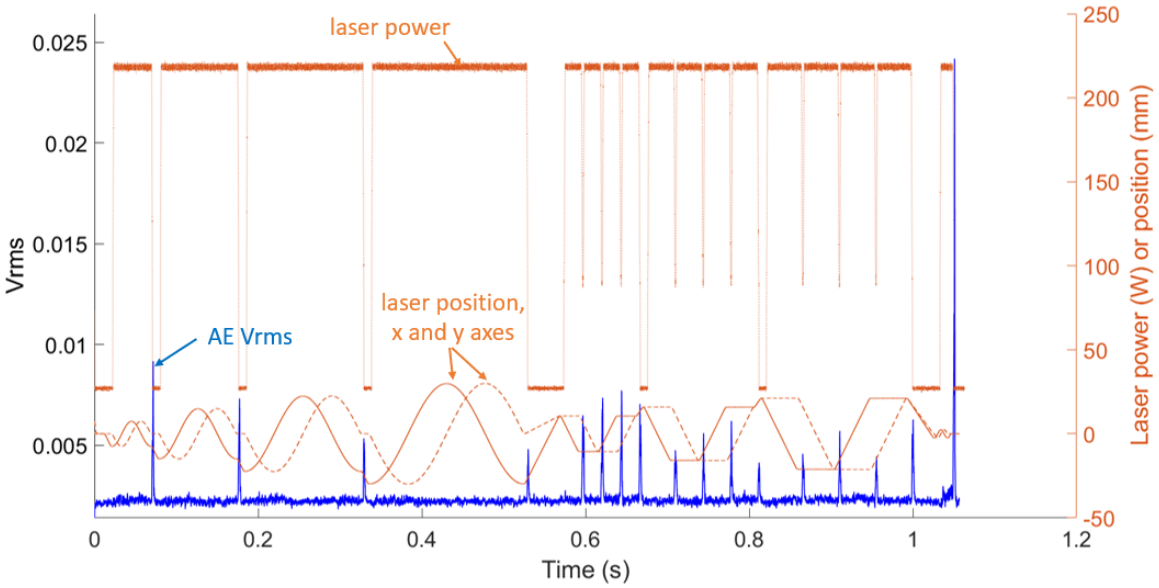

FIGURE 20: Synchronized data from bare Ti64 substrate.

A small adjustment was made by scaling the AMMT time vector to align these peaks consistently with the moment the laser turns off, resulting in an actual AMMT sampling rate of 99.4 kHz. This scaling is applied to all future datasets in the next experiment to ensure that noisier data is still synchronized properly. When a single layer of powder is introduced, the peaks are indistinguishable from the additional AE generated by the process, as shown in FIGURE 21. Note that the maximum RMS of the recorded AE signal increases by a factor of almost five.

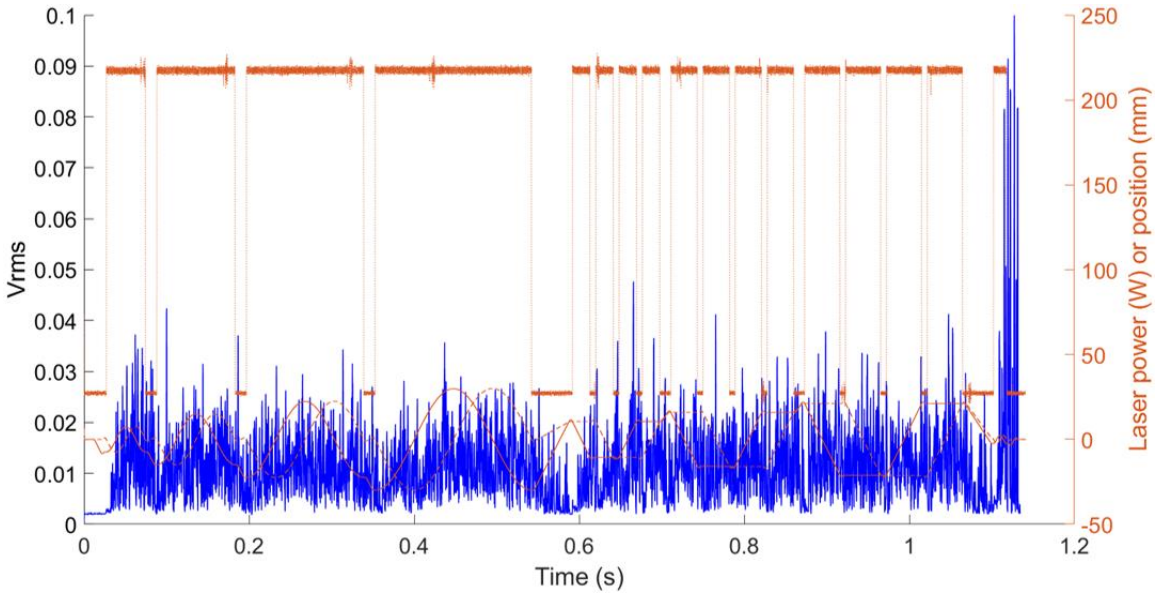

FIGURE 21: Synchronized data from Ti with 5% Cu powder.

Closer inspection of the raw AE signal from the single powder layer scan reveals distinct, individual AE events occurring about 6 ms after the laser turns on, around 0.327 seconds. FIGURE 22 shows the beginning of this raw AE signal.

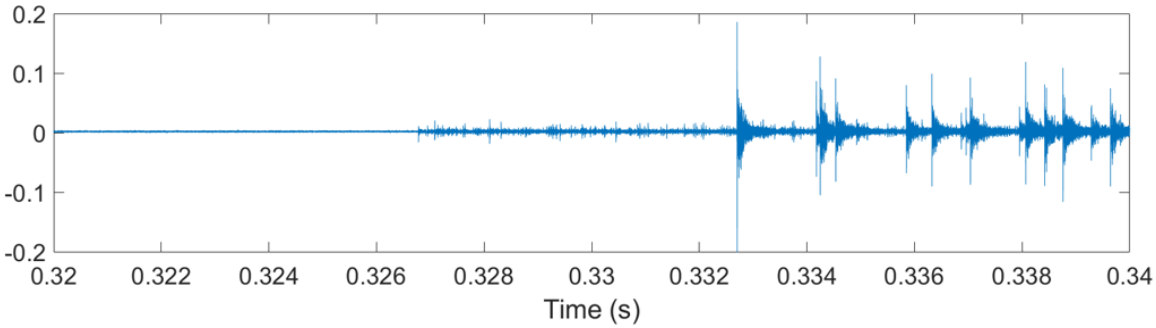

FIGURE 22: Raw AE from beginning of scan using Ti with 5% Cu powder.

These events are not present in the AE signal from the bare substrate scans, leading to the hypothesis that they are a result of introducing powder to the process. The peaks from FIGURE 20, while proving useful to align the datasets, are caused by using the Exact Stop laser mode when generating the scan code. In Exact Stop mode, the laser beam travels to the end of the track and stops before turning off. The AE signal spikes because the linear energy density is very high when the velocity is zero. The peaks were

no longer present when using Constant Build Speed mode in future scans. With Constant Build Speed mode, the laser accelerates to the desired scanning speed before switching the beam on at the beginning of the track and decelerates after the laser turns off at the end of the track. This results in a constant linear energy density along the entire track.

3.3 Process map

The preliminary experiments show that the measurement setup has an appropriate resolution and noise level that allows detection of distinct AE events during laser melting. The next set of experiments consists of single-layer tracks made using different process parameters, with the goal of determining whether features can be extracted from the AE signal to correlate with surface defects or identify different modes of melting. Two major process parameters in the LPBF process are laser power and laser scan speed, which both strongly affect the build quality, especially concerning porosity. (Gong et al. 2014) Laser power and scan speed parameter combinations for the next experiments were chosen based on an existing process window, or map, for Ti64 powder shown in FIGURE 23.

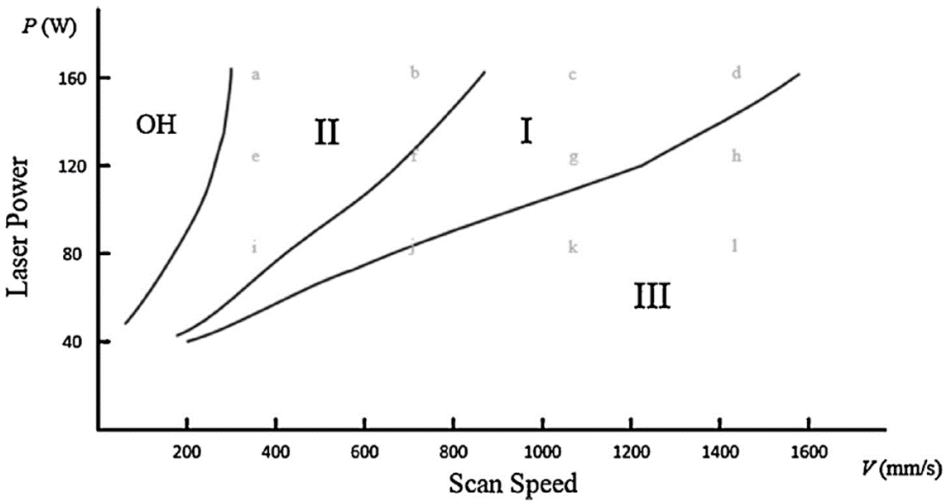

FIGURE 23: Process map for Ti64 with four melting zones. (Gong et al. 2014)

This process map is divided into four zones: “fully dense” (Zone I), “over melting” (Zone II), “incomplete melting” (Zone III), and “over heating” (Zone OH). The zones were determined experimentally by measuring the densities and observing the top surface topologies of samples made with various process parameter combinations. (Gong et al. 2014)

Gong’s process map was extended to meet the AMMT’s 400 W max laser power capacity and to push the laser scanning speed toward what commercial machines are currently capable of. Each circular dot in FIGURE 24 represents a process parameter combination that will be used to create individual tracks from a single layer of powder.

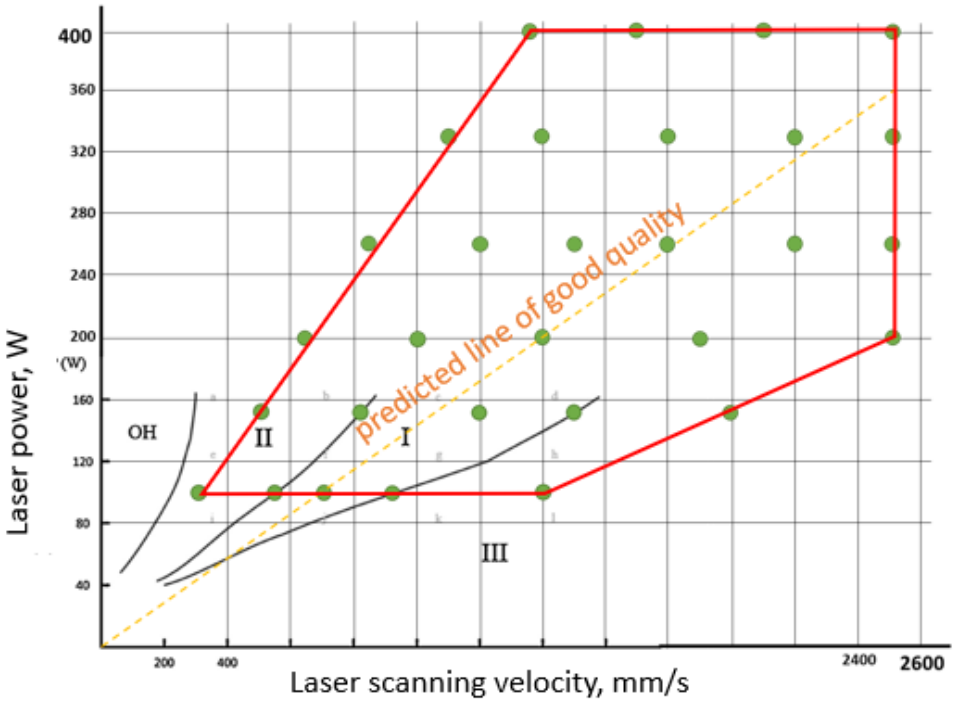

FIGURE 24: Parameter space chosen for the Ti64 process map.

The parameter combinations were arranged on either side of a line of predicted optimal parameters in order to create tracks of good and bad quality, while avoiding the extreme overheating zone on the far left. The line is based on the hypothesis that uniform

linear energy density, or laser power over scanning speed, will result in a similar track quality. This hypothesis was later proven to be wrong.

3.4 Experiment A design

The 30 different parameter combos were used to create sets of 30 individual tracks, each 15 mm long because “the melt pool length of single scan lines typically stabilizes within 1 mm to 2 mm of the start of the scan”. (Heigel and Lane 2018) A single scan direction was chosen to prevent residual heat buildup that could influence the quality of the adjacent track. The tracks are spaced 0.5 mm apart to prevent denudation effects, which are common during LPBF, from overlapping. (Matthews et al. 2016) Tracks are grouped by laser power and are created in sets so that each parameter combo is scanned three times for averaging purposes. These sets are oriented close to one edge of the substrate, which would make it easier to EDM a section through the tracks for future polishing, etching and inspection of the track cross sections.

In addition to the single-direction individual tracks, pads were designed that consist of multiple closely spaced tracks with alternating scan direction. Each pad contains at least 20 adjacent tracks to ensure that steady-state conditions are achieved after the 7^{th} track. (Heigel and Lane 2017) FIGURE 25 shows the final layout and TABLE 3 lists the process parameter combinations for every track or pad in each set.

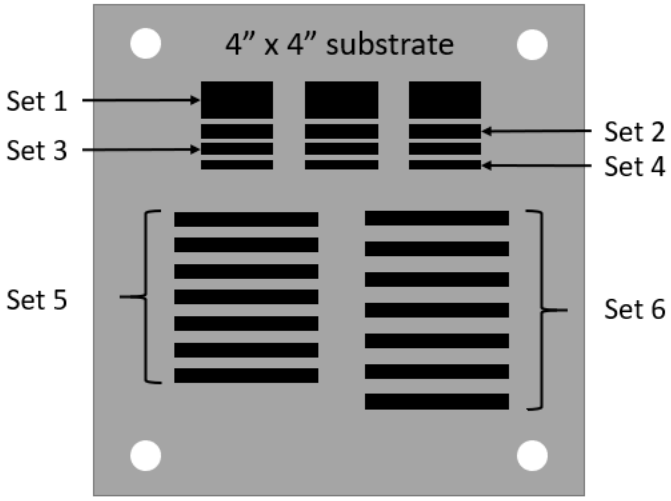

FIGURE 25: Track and pad layout on Ti64 substrate.

TABLE 3: Experiment A process parameters (laser power in W, scan speed in mm/s).

Set 1		Set 2			
Power	**Speed**	**Power**	**Speed**		
100	300	260	850	**Set 4**	
100	550	260	1200	**Power**	**Speed**
100	700	260	1500	400	1350
100	920	260	1800	400	1700
100	1400	260	2200	400	2100
150	500	260	2500	400	2500
150	820				
150	1200	**Set 3**		**Set 5**	
150	1500	**Power**	**Speed**	**Power**	**Speed**
150	2000	330	1100	150	820
200	650	330	1400		
200	1000	330	1800	**Set 6**	
200	1400	330	2200	**Power**	**Speed**
200	1900	330	2500	150	1200
200	2500				

Because lack-of-fusion porosity scales with the overlap depth between adjacent melt pools (Cunningham et al. 2017), each of the seven pads from Sets 5 and 6 have varying overlap depths to create pads of varying quality. For the LPBF process, the overlap depth between adjacent melt pools is determined by hatch spacing, or the center

to center distance from one track to the next. The hatch spacing for Sets 5 and 6 varies from 70% to 100% of the average track width in increments of 5%.

3.5 Experiment A process

Fine leveling adjustment was not available because the leveling mechanism had to be removed due to the weight of the instrumentation rig. Therefore, the automated recoater mechanism could not be used to spread the powder. After installing the substrate, plastic shims 80 μm thick were attached to two edges of the substrate, as shown in FIGURE 26.

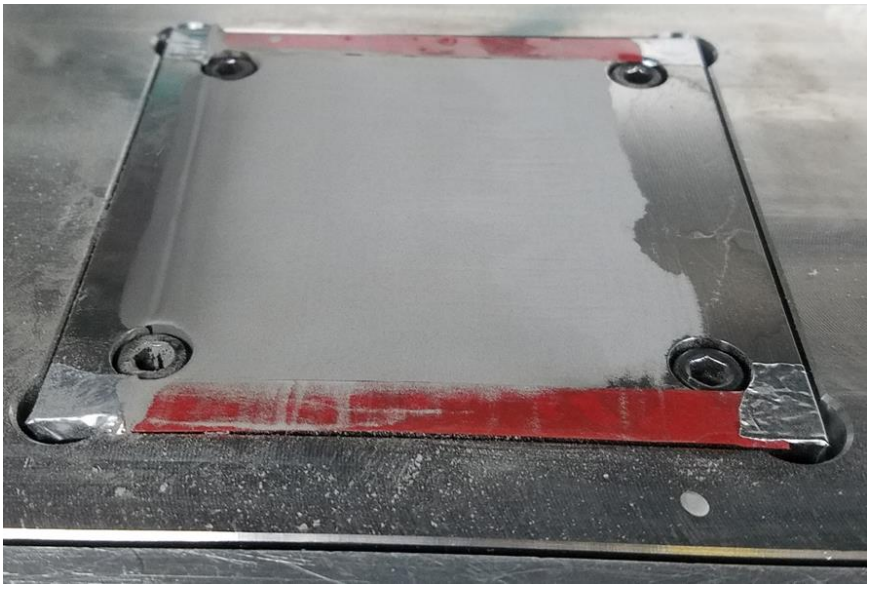

FIGURE 26: Manually spread, single layer of Ti64 powder ready for scanning.

An appropriate amount of powder was deposited on one side of the substrate, and a spare recoater blade was used to spread the powder by dragging the blade across the substrate by hand while maintaining contact with the shims on either side. After several unsuccessful attempts to create a smooth, uniform powder layer, isopropanol was mixed with the powder in a small container (suggested by NIST guest researcher Ivan Zhirnov) The resulting slurry was then poured onto the substrate and quickly spread using the

spare recoater blade. The alcohol evaporated completely within several minutes, leaving behind a uniform powder layer.

As shown in FIGURE 27, the build plate with substrate (1) is covered by the plexiglass enclosure (2) described in section 3.2 and argon is injected through a hose (3) at 30 scfh to the inside of the enclosure through a diffuser (4). After most of the oxygen inside the enclosure is flushed out and replaced by argon, the laser is aimed down through a special window (5), scanning according to the commanded pattern to melt the powder which then rapidly cools to create solid tracks.

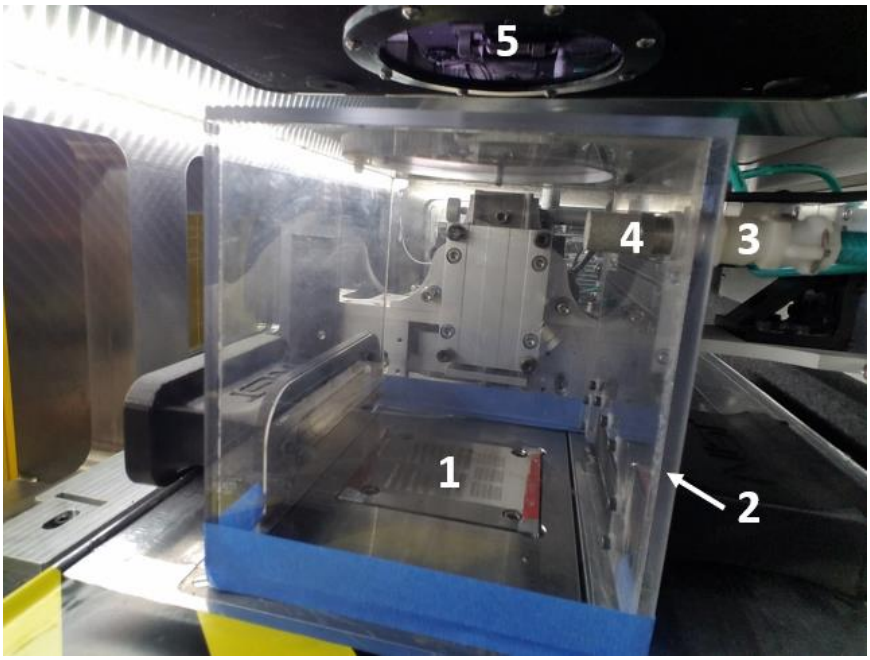

FIGURE 27: Enclosure for argon environment inside the AMMT.

3.6 Experiment A results

Like in the preliminary experiment, distinct AE events were detected during laser operation, as shown in FIGURE 28. AE events can also be seen outside the 15 mm long track, where the laser is inactive and repositioning to scan the next track.

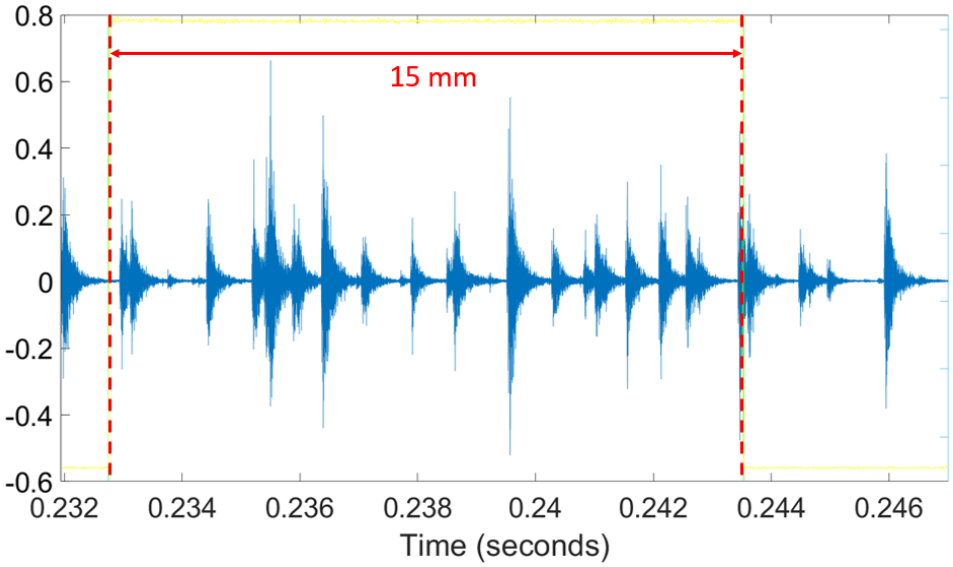

FIGURE 28: AE events during the LPBF process.

The AE data from every track in Sets 1-4 contain many of these events that begin shortly after the laser first starts melting powder, all the way to the end of the record. After cleaning off the excess powder and removing the substrate from the build plate, the top surface topography was inspected using a microscope. Many lateral cracks across the entire track were readily distinguishable in every track in Sets 1-4, regardless of the process parameter combination (P/V) used. In addition, longer cracks were seen all over the pads from Sets 5 and 6, as shown in FIGURE 29.

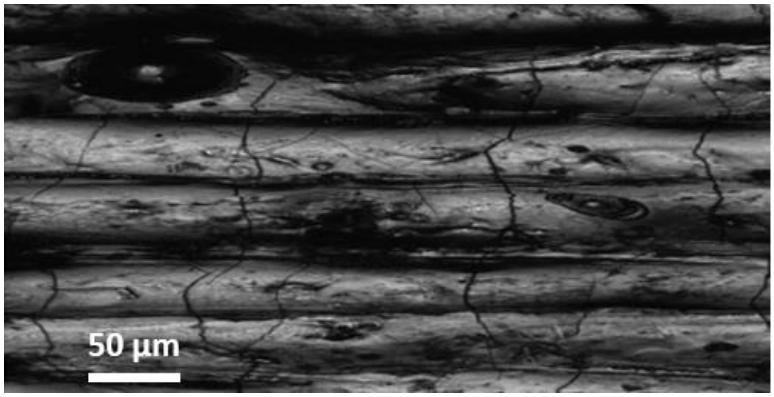

FIGURE 29: Example of cracking on pads created with single-layer Ti64.

Some tracks were selected for further analysis with a Zygo Zegage scanning white light interferometer (SWLI). A 20x objective was used on the Zegage to take interferograms along the entire length of these tracks and stitch them together in a single image. FIGURE 30 shows an example of the cracking observed using the SWLI.

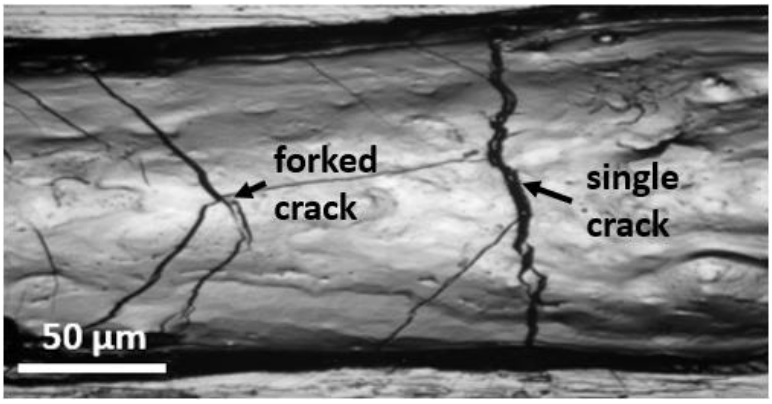

FIGURE 30: SWLI intensity image of Ti64 track created with P/V = 100/700.

Many of the thinner forked lines on the intensity images were not identifiable as cracks in the height maps from the SWLI, even with a 50x objective and appropriate spatial filtering. It should be noted that the Zegage has a default 3x3 filter that is automatically applied to the height data. This loss of resolution may be the reason why thin cracks are more visible in the intensity images, which are unfiltered. An example is shown in FIGURE 31 with an intensity image and a height map of a section of a track that contains several thin lines that appear to be cracks.

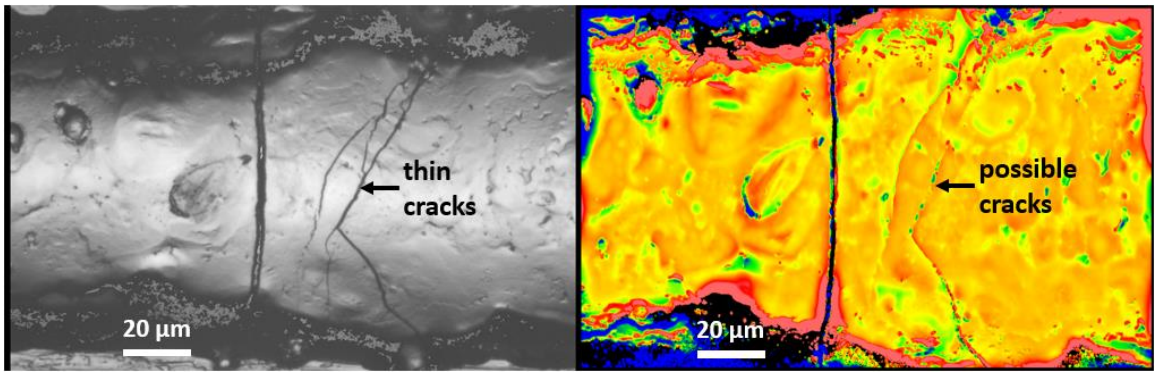

FIGURE 31: Intensity image (left) and height map (right) from SWLI.

Due to the difficulty in distinguishing thinner cracks from the surrounding topographical features, an automated image analysis and crack-counting algorithm cannot be reliably applied. Further analysis using a JEOL JSM 6480 scanning electron microscope (SEM) confirms that the thin lines seen in the SWLI intensity images are truly cracks, as shown in FIGURE 32.

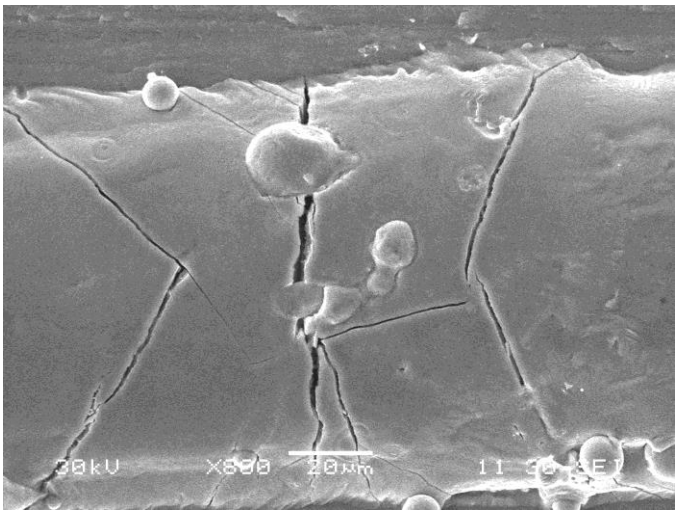

FIGURE 32: SEM image of cracking across Ti64 track.

Cracks were counted for the selected subset of tracks by visually inspecting the stitched intensity images and counting large single cracks as 1 and forked cracks as 2. This is certainly not the best method since it depends on the judgement of the operator and the distribution of the types of cracks, which may change with process parameters. However, it is the most time-efficient method and the effect of possible miscounting is low due to the high number of cracks in each track. AE events were also counted by taking the absolute value of the raw AE data, generating a signal envelope using MATLAB's envelope function and defining a threshold at three times the noise level when the laser is active, but no AE events are occurring. Finally, the peaks of the envelope above the threshold are counted as demonstrated in FIGURE 33.

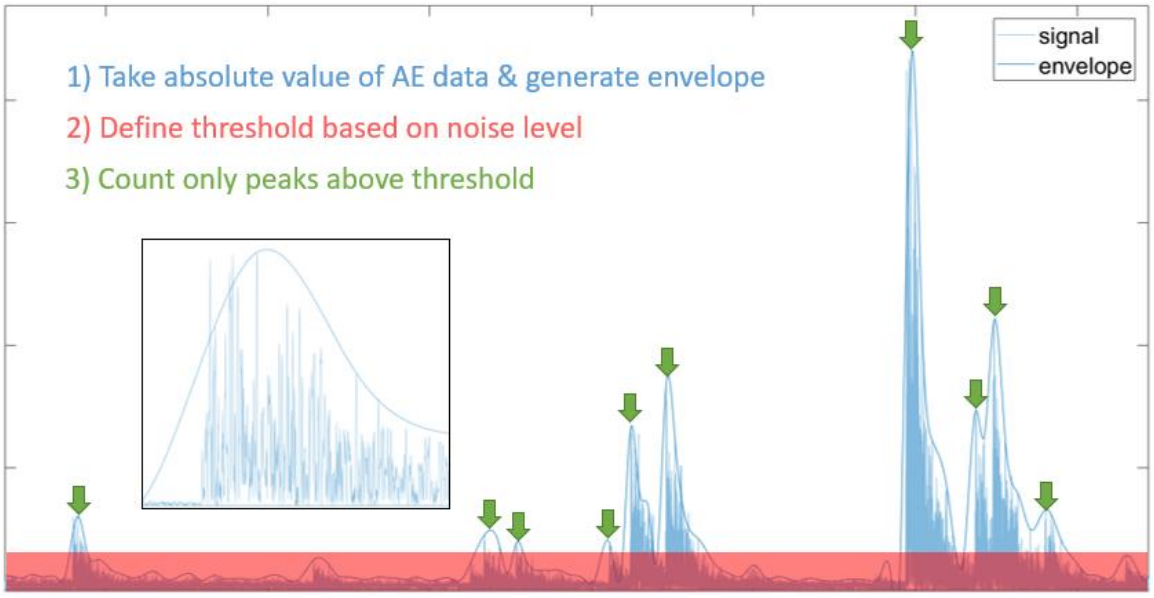

FIGURE 33: AE event counting process in MATLAB.

Although this process may not count all the AE events accurately, especially since some are overlapping, the envelope parameters were adjusted to balance between under- and over-counting. The envelope method was applied consistently to all the evaluated tracks, and FIGURE 34 shows an example of the result of counting AE events with the laser both on and off, where counted peaks are identified with a circle above the peak.

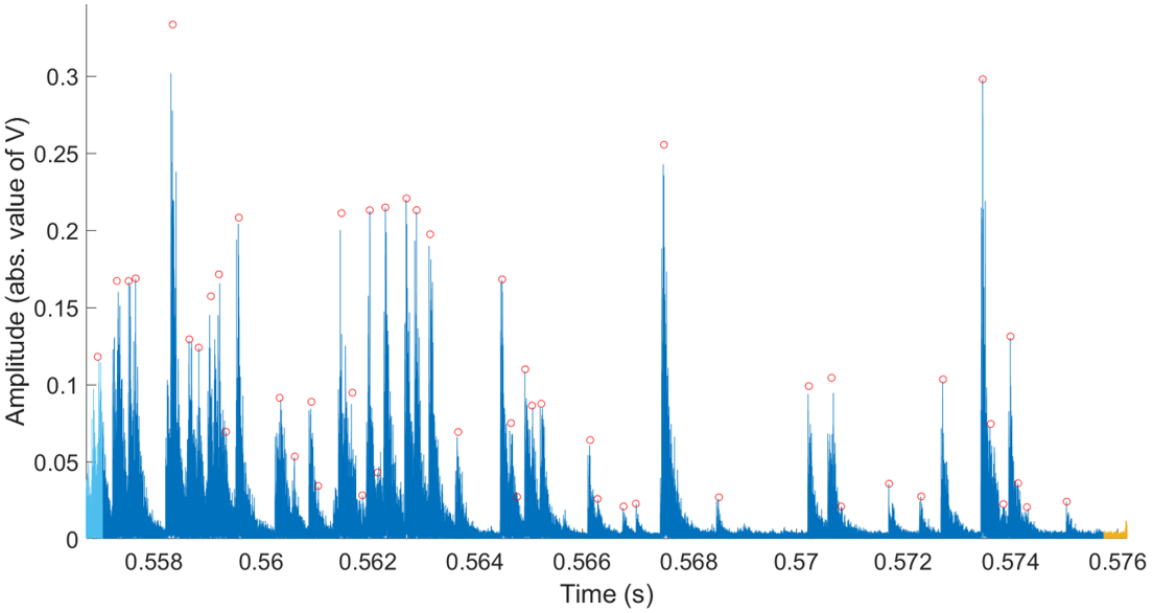

FIGURE 34: Example of AE event peaks counted using MATLAB's envelope function.

While the number of counted AE events increase with the number of observed cracks, a 1:1 relationship is not being claimed in this work. The distinct AE events occur when scanning the laser over a powder-covered substrate, but it has not been proven that solidification cracking is the source of the AE. There is also no correlation of the number of cracks to linear energy density, as shown in FIGURE 35.

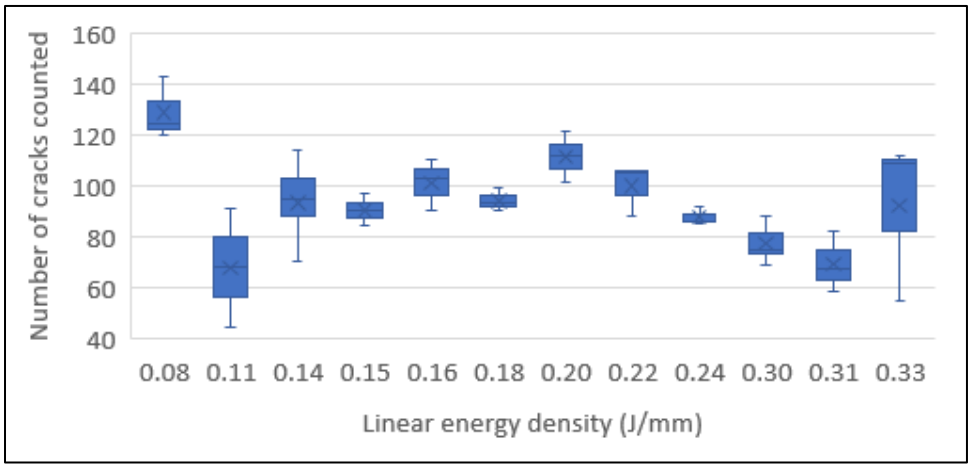

FIGURE 35: Crack counts for selected tracks, sorted by P/V ratio.

Crack counts from each of the three tracks created with the same process parameters were averaged and overlaid on the extended process map as shown in FIGURE 36. Analyzing only a subset of tracks, there are no process map areas that have consistently high or low average crack counts, except for the top left edge of the map.

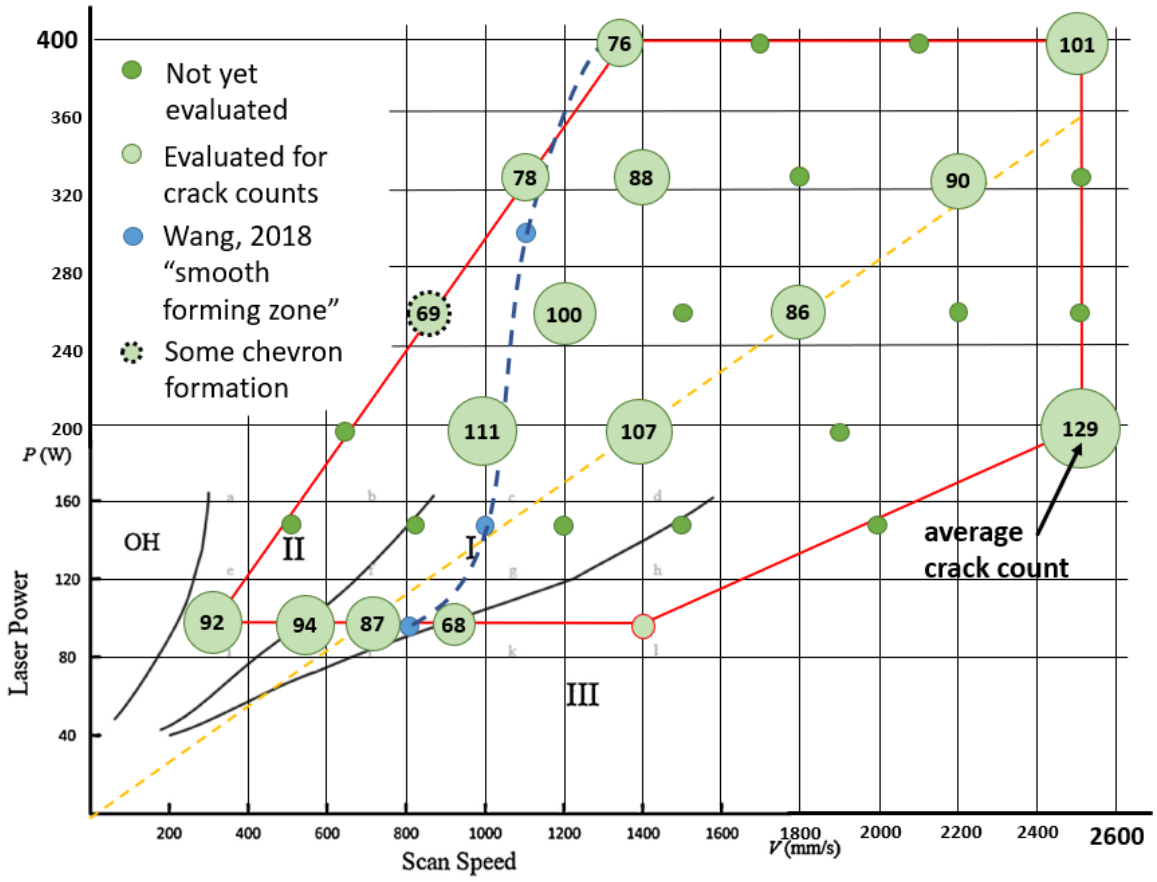

FIGURE 36: Average crack counts on Ti64 process map (based on Gong et al. 2014).

A further literature review revealed that "The traditional belief that setting the linear energy density appropriately can necessarily guarantee surface quality is incorrect." (Wang, Dou, and Yang 2018). Wang, et. al experimentally defined a "smooth forming zone" for Ti64 fabricated via LPBF. Although there is an exception at the P/V combination of 200/1000, most of the selected parameter combinations with lower average cracking are in the vicinity of Wang's ideal zone, with one set of tracks (P260, V850) even displaying some chevron formation, one topographical indicator of properly formed tracks (Gan et al. 2019).

However, due to the excessive cracking observed in every single track, a hypothesis was formed that the build plate and substrate should be preheated to achieve a

crack-free baseline signal at the optimal laser parameters. “Base-plate preheating shows an efficient method to reduce the scales and number of cracks. The residual stress was reduced by more than 50% when preheating at 300℃.” (Shuai et al. 2016) and “…pre-heating temperatures within commercial SLM systems are generally limited to below 200 °C…” (Ali et al. 2017). The Ti64 parameter preset for a commercial machine like the EOS M290 includes a pre-heat temperature of up to 200 °C. However, the maximum pre-heat temperature for the instrumentation rig is limited by the AE sensor’s maximum operating temperature of 177 °C.

As mentioned in the beginning of this section and demonstrated in FIGURE 37, there is still significant AE activity for at least several seconds after the laser finishes melting the tracks. A hypothesis was formed that cracking continues to occur while the plate is cooling or unwanted AE sensor coupling with the rig’s structure is causing ringdown effects to appear in the data. These issues are addressed in Chapter 5.

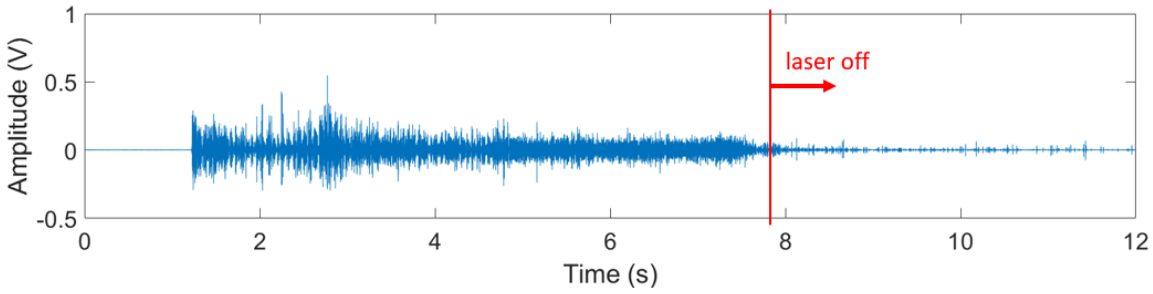

FIGURE 37: AE signal during scanning of all pads in Experiment A, Set 4.

CHAPTER 4: IMPROVEMENTS

4.1 Build plate heater

Initial experiments using a heating lamp above the substrate were unable to raise the underside of the substrate to 60 °C, even when partially insulated. An Abaqus FEA model of two polyimide strip heaters directly underneath the substrate predicted the top surface reaching only 80 °C after 30 minutes of heating.

In contrast, the original resistive heater installed in the AMMT was able to heat the underside of the build plate so that the top surface reached 100 °C in 24 minutes. To reach the desired temperature of 160 °C and to fit the dimensions of the build plate and sensor configuration, a 4” diameter, ring-shaped resistive heater was chosen. Compared to low-power polyimide or mica strip heaters, the 500 W ring heater from Omega has a heating capacity similar to the existing 400 W tubular heater in the AMMT.

Material was removed from the build plate and seal assembly plates via CNC machining to accommodate the ring heater and its wires, allowing the heater to be spring-loaded against the underside of the substrate and leaving a 3 mm insulating air gap under the heater when the substrate is installed, as shown in FIGURE 38. The heater is just thin enough to allow installation of an AE sensor and an RTD to monitor the substrate temperature.

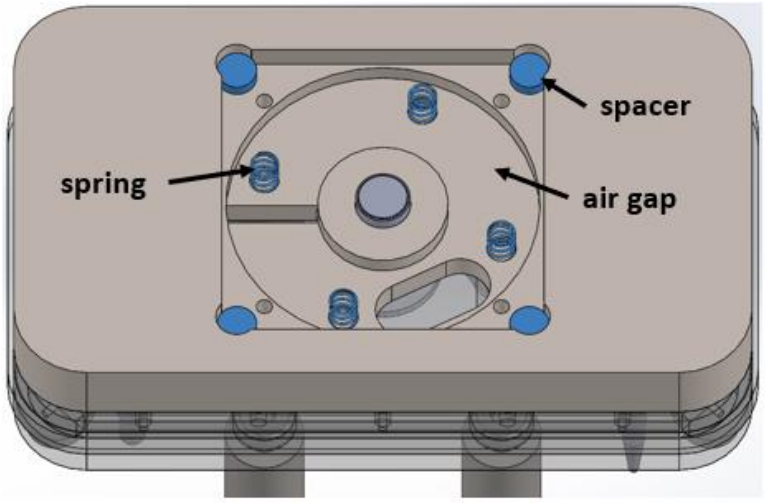

FIGURE 38: Modified build plate with spacers and springs to support the ring heater.

Three high-temperature wires were assembled into a cable with ring terminals that connect to the heater and ground on the rig on one end, with a C14 termination in accordance with IEC 60320 for connection to a C13 power cord on the other end. FIGURE 39 shows the 500 W ring heater, AE sensor and RTD installed and ready for thermal grease and ultrasonic couplant to be applied. The RTD is first attached to the bottom of the substrate with aluminum tape and positioned to avoid contact with the heater and AE sensor. The substrate is then pushed against the spring-loaded heater and AE sensor while the four screws are tightened from above to hold the substrate against the four spacers in each corner. This top-down installation scheme allows substrates to be swapped out quickly for multiple, back-to-back, single-layer experiments.

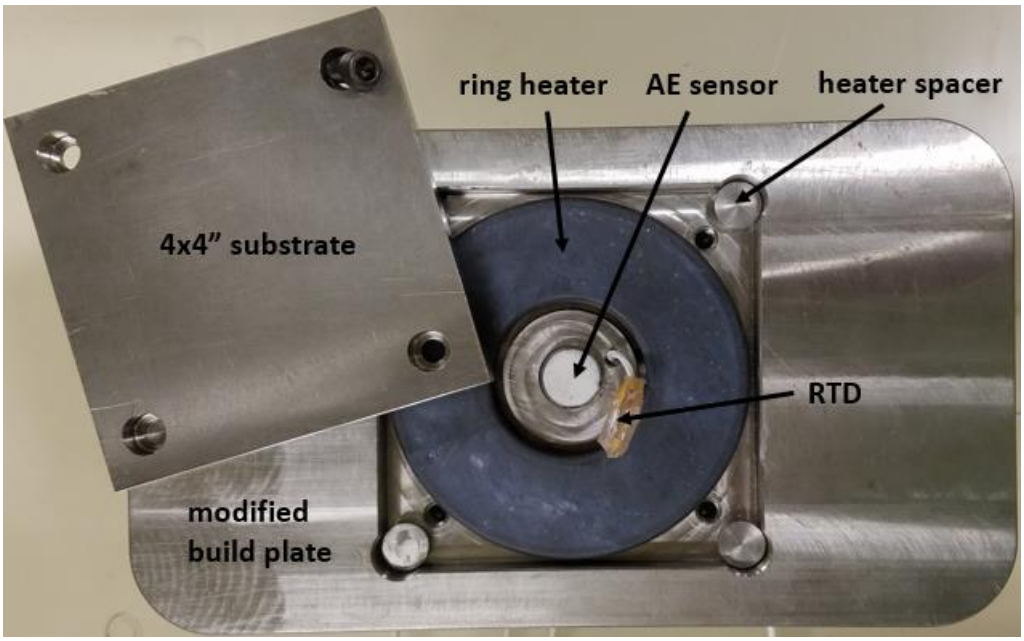

FIGURE 39: Top view of the heater and sensor configuration

4.2 Heater control

Raising and holding the temperature of the substrate at the desired value requires a closed-loop control system. With the spring-loaded heater and feedback RTD installed directly underneath the substrate, an existing Arduino program was modified (See APPENDIX) to create a simple bang-bang controller. Calibration RTDs attached across the top of the substrate confirmed a small, but acceptable, temperature gradient of 6 °C for a set point of 100 °C. Addition of thermal paste between the heater and the substrate improved response time which decreased oscillations around the set point from 11 °C to 7 °C. Overshoot in the beginning however, as seen in FIGURE 40, was unacceptable since it limited the maximum set point to ~30 °C below the overshoot peak.

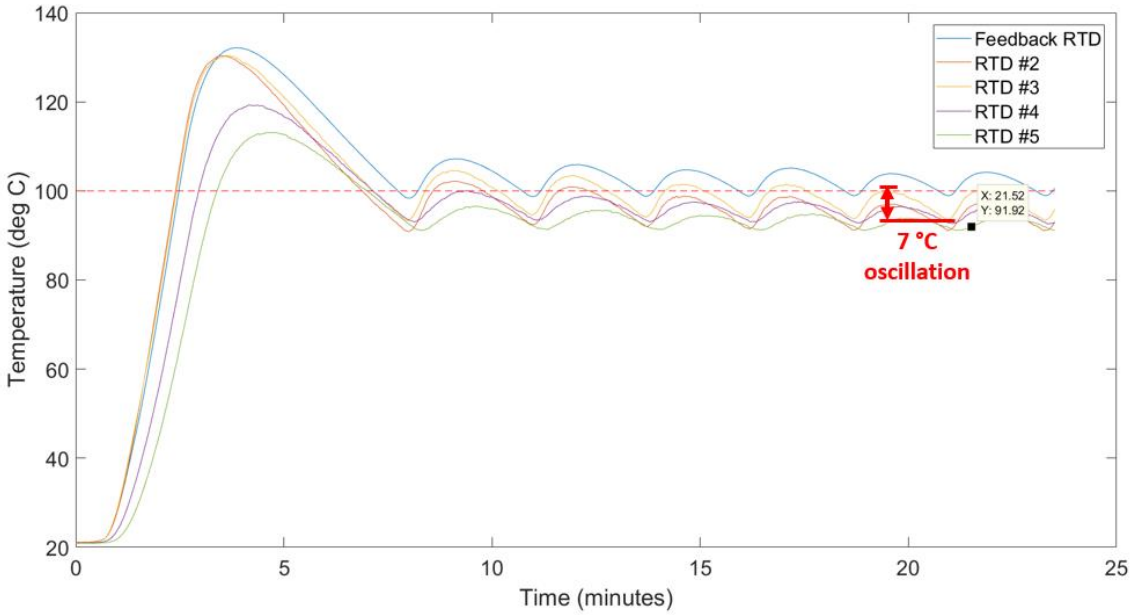

FIGURE 40: Initial overshoot and oscillations around a 100 °C set point using a bang-bang controller.

A properly tuned PID controller will reduce overshoot, so a LabVIEW-based controller was developed that can be integrated into the data acquisition program. Instead of purchasing a specialized RTD module, SPI communication with the feedback RTD had to be established through an RTD-to-digital converter connected to a previously purchased multifunction I/O module. A relay-controlled power strip enables PWM-based control of the effective heater power.

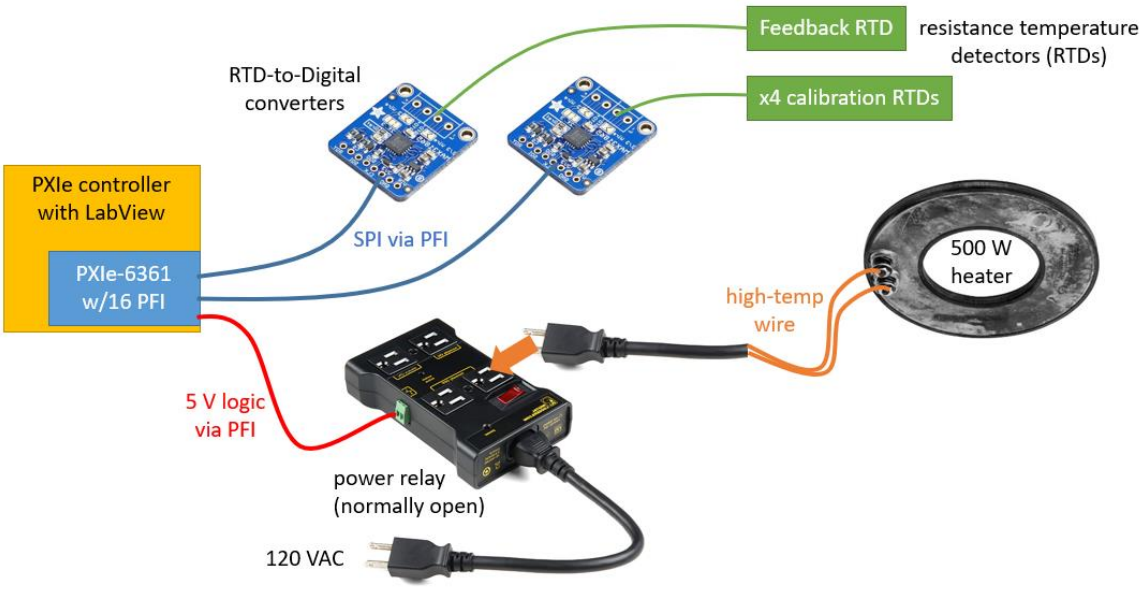

FIGURE 41: Equipment required to preheat the substrate.

An existing Arduino program for communication with the RTD-to-digital converter was first reverse engineered with the help of a Saleae logic analyzer. SPI communication was replicated in LabVIEW by writing a VI, or program, that sends commands to the RTD converter chip via bit-banging. The raw output of the chip is then converted to a decimal number, a resistance value and finally, a temperature using the Callendar-Van Dusen equation (Maxim Integrated 2015).

FIGURE 42 shows an example of the digital bits that make up a command to read a value from the chip. The Chip Select (CS) channel is sent low, the Servant Data In (SDI) channel sends 8 bits to correspond with each of the 8 “ticks” sent by the Clock (CLK) channel. From the memory location defined by the first 8 bits on the SDI channel, two more sets of 8 bits are read through the Servant Data Out (SDO) channel and the CS channel is sent high to be ready for the next command. Not shown are the configuration address and values that must be sent to the chip before the RTD can be read correctly.

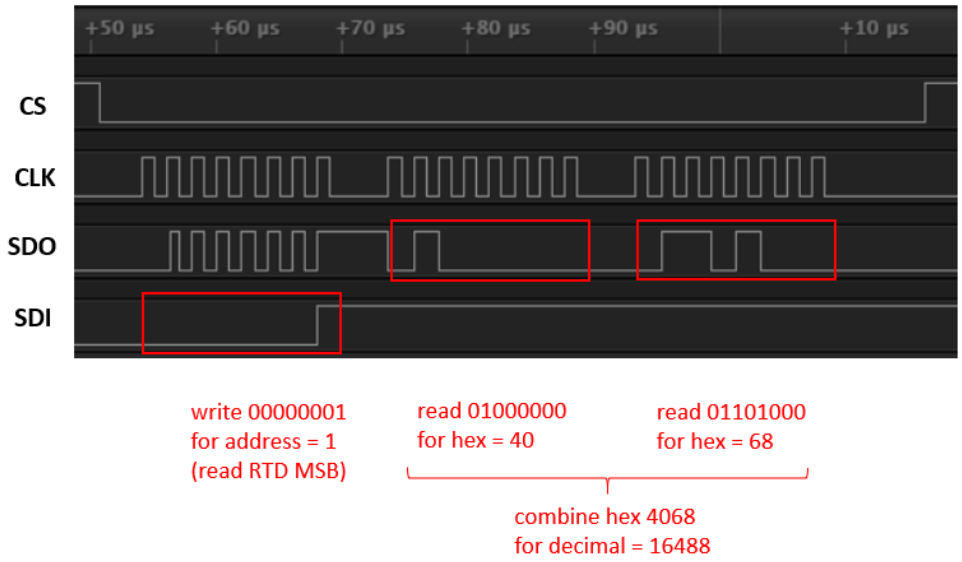

FIGURE 42: Output of Saleae logic analyzer demonstrating SPI communication.

Next, another LabView program was written based on PID theory, shown in FIGURE 43. The purpose of this program is to calculate a value, u(t), that is proportional to the error, e(t), which is the difference between the set point and the measured temperature, y(t).

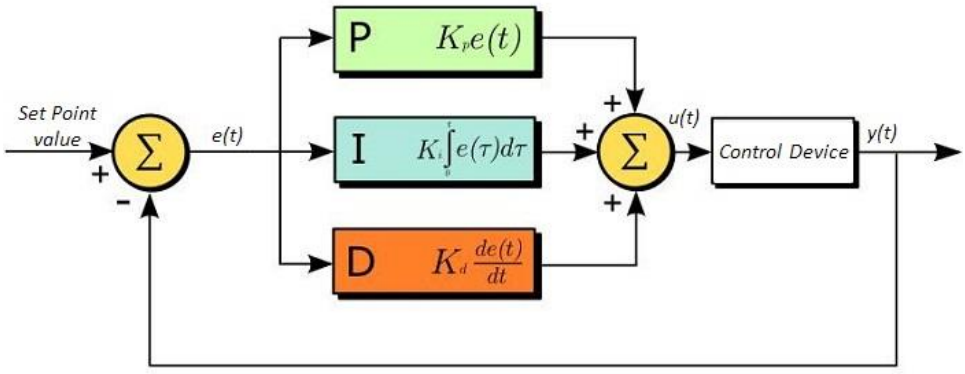

FIGURE 43: PID theory (Thorlabs Inc 1999).

A third LabView VI was written to cycle the heater on and off via an electromechanical relay. The time that the heater remains on, at full power, is based on the u(t) value calculated by the PID program. The effective heater power is calculated by multiplying the duty factor by 500 W during each one-second cycle period.

Even a partially tuned PID controller demonstrated a significant decrease in the overshoot and oscillation about a 100 °C set point with a similar rise time, as shown in FIGURE 44.

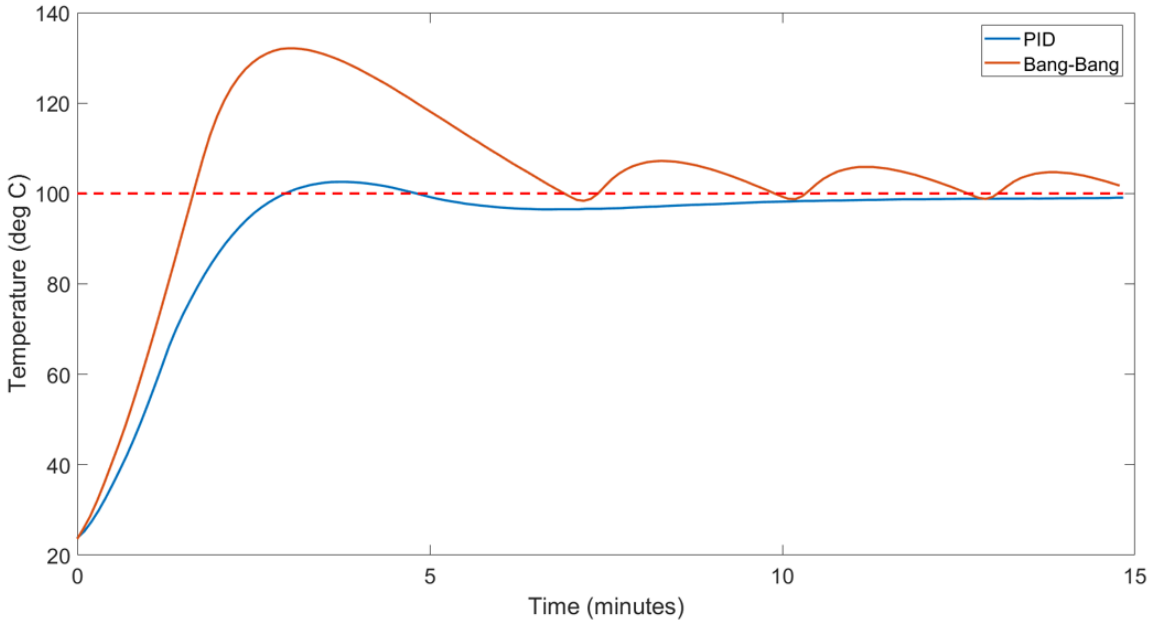

FIGURE 44: Comparison of heater control methods.

However, quickly reaching the desired set point of 165 °C with no overshoot and minimal oscillations requires fine-tuning of PID parameters. After unsuccessfully attempting to tune the controller using the Ziegler-Nichols and Åström–Hägglund tuning methods, the parameters in TABLE 4 were selected by conducting 24 subsequent heating tests. When the heater controller is first activated, the relay remains in a closed position until the temperature reaches 50 °C below the setpoint, after which the relay is controlled via PWM according to the PID controller's output.

TABLE 4: Final PID controller parameters for a 165 °C set point.

Parameter	Value
proportional	0.5
integral	0.02
derivative	8
cycle time	1 s
dead time	2 s
PWM range	50 °C

A cycle time of 1 second was chosen to simplify troubleshooting and scaling of values. A dead time of 5 seconds was originally incorporated to compensate for the system's large time constant and to increase the life of the mechanical relay but was eventually decreased to 2 seconds to improve response time. To prevent integrator windup, the integral term is set to zero while the measured temperature is outside a certain range relative to the set point. To eliminate derivative kick caused by a large change in the error, the standard PID equation was modified to calculate the derivative of the measured temperature rather than the derivative of the error. As shown in FIGURE 45, the optimized PID heater controller is capable of rapidly bringing the substrate to 165 °C with almost no overshoot and stable oscillations of +1/-4 °C.

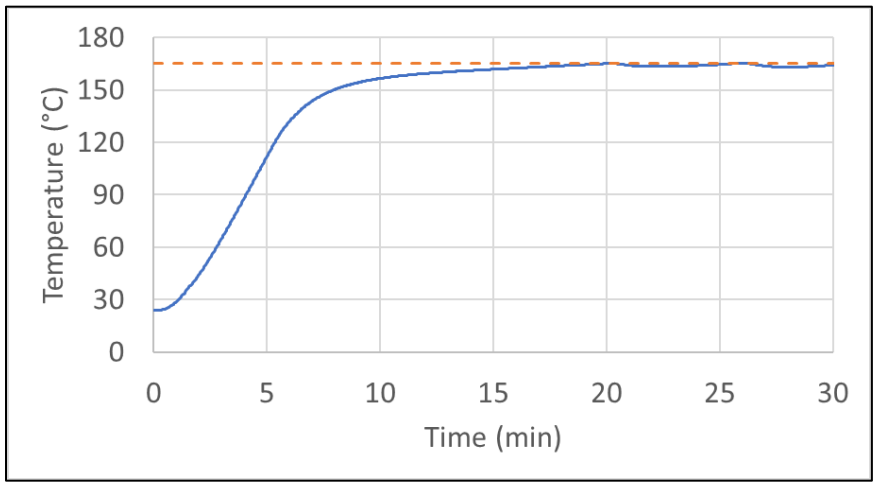

FIGURE 45: Holding the substrate at 165 °C with the optimized PID controller.

4.3 Leveling mechanism

The original, more delicate leveling mechanism in the AMMT had to be removed due to the weight of the instrumentation rig. Rough leveling could only be achieved by placing plastic shims underneath the rig, which prevented leveling after installing the rig. To enable fine leveling of the interchangeable substrates after installation, a more robust leveling mechanism was designed.

FIGURE 46 shows the final design of the new leveling mechanism with a flexure for rigidity while allowing bending in the desired plane, a steel ball for low friction while sliding against the upper plate, a linear bearing to keep the shaft from moving laterally and a removable bolt used to hold the bottom two plates together while installing the rig on top of the build arm.

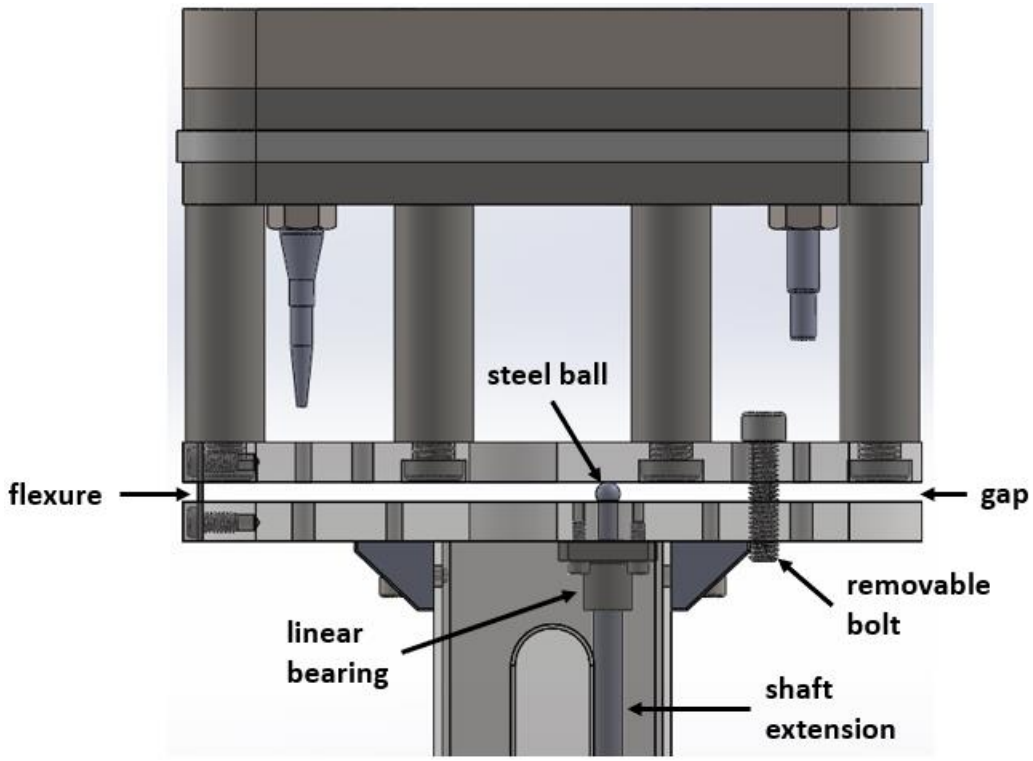

FIGURE 46: Side view of build stack with new leveling mechanism.

The steel flexure was designed to be stiff enough to support the 40 lb weight of the rig while allowing bending so the bottom plates can close the gap on the other end of the rig if needed. The required flexure thickness, h, was calculated from the moment applied by the weight of the rig and the dimensions of the top part of the flexure, as shown in FIGURE 47.

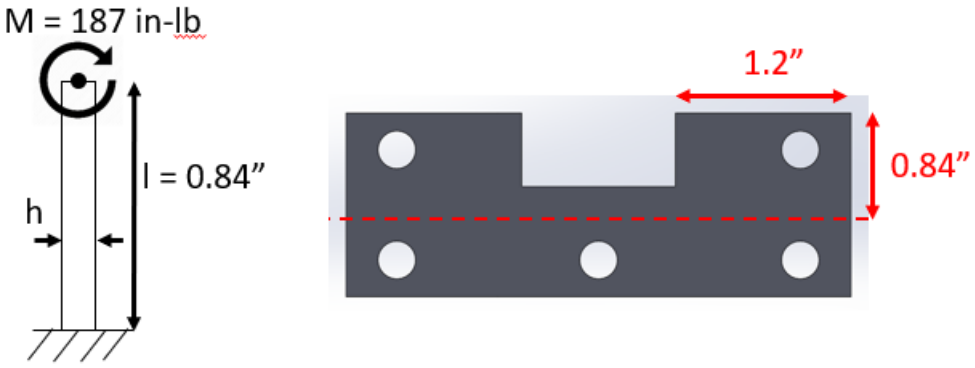

FIGURE 47: Flexure free body diagram and critical dimensions.

The shaft of the linear actuator for the original leveling mechanism was extended upwards to directly support the bottom of the rig. Leveling is achieved by extending or retracting the shaft, so the rig tilts up or down under its own weight. The linear actuator is capable of micro stepping, with a positioning resolution better than that of the Keyence laser displacement sensor used to measure the height and tilt of the build plate from above. Leveling is achieved by measuring the substrate height at two locations close to either edge of the substrate, then iteratively adjusting the linear actuator while remeasuring the height of the substrate edges until they are equal. With this method, substrates can be repeatably leveled to within 5 μm over their 100 mm width.

4.4 Combined data acquisition software

The original LabVIEW data acquisition program was set up to store AE data in the oscilloscope’s onboard memory using a “one-shot” method that was easier and faster

to program than using buffers to transfer data to the hard drive in real-time. Due to the high sampling rate of 10 MHz however, the onboard memory can only handle about 12 seconds of continuous recording. This limitation is not sufficient for recording AE during longer laser scans like single-layer pads or multi-layer structures. Therefore, a new program based on National Instrument's "Stream To Disk (Host)" VI was developed to stream AE data directly to the controller's hard drive. In addition, data acquisition capabilities for the temperature sensor and instrumented bolts along with PID control for the heater were integrated into the main program.

To handle the various acquisition rates for multiple types of sensors, the main program consists of 8 parallel loops as shown in FIGURE 48. This program architecture offers control via a queued state machine (LabVIEW Wiki 2019) with multiple producer loops acquiring and sending data to a consumer loop that updates the user interface (UI) display for the user.

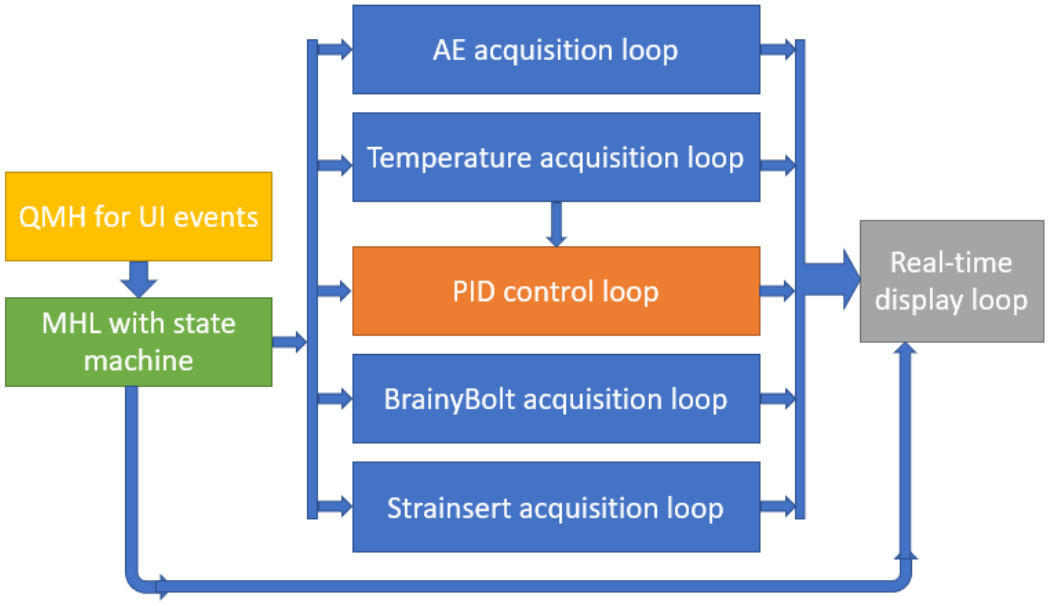

FIGURE 48: Combined data acquisition program architecture.

The queued message handler (QMH) is an event-driven loop that detects UI events such as button clicks or value changes and sends the relevant desired state to the message handler loop (MHL). Multiple messages from the QMH are stored in a queue in the order they are generated to prevent commands from being lost. The state machine inside the MHL receives the messages from the QMH and activates the desired state. The chosen state will then process the code it contains, such as updating the UI or sending commands to the producer loops. Once the code is processed, the state machine will either move to another state and process that code or return to idle and await the next message from the QMH. The state structure in the final version of the data acquisition software is shown in FIGURE 49.

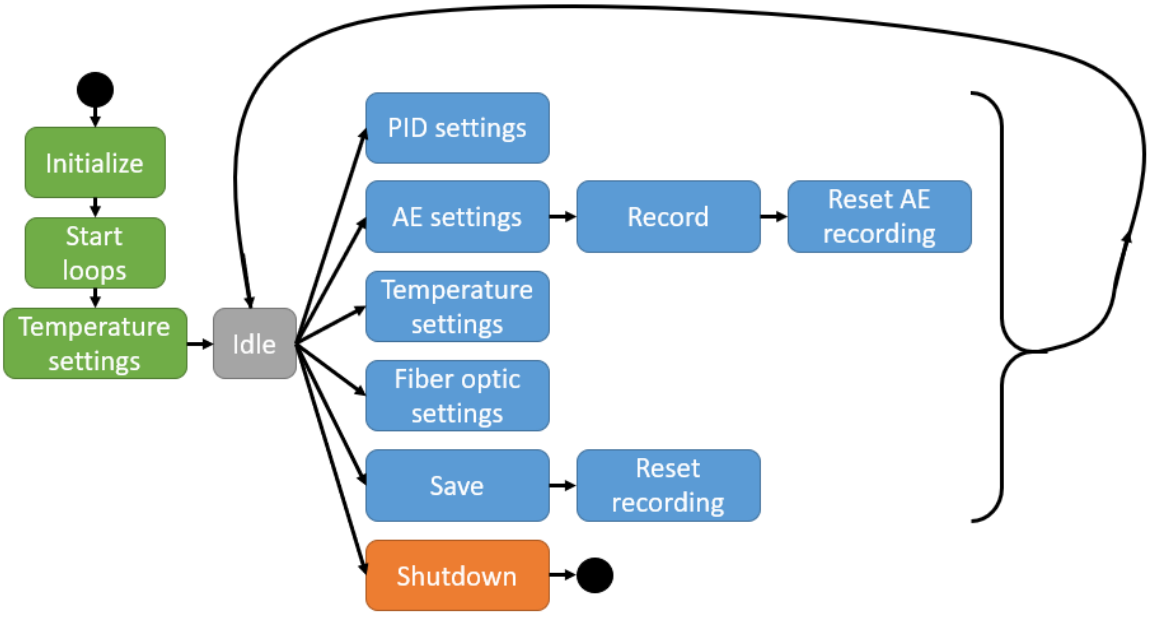

FIGURE 49: State machine diagram.

The main benefit of this queued state machine architecture is that the UI does not have to be constantly polled, which would use up CPU cycles unnecessarily. At the same time, states can be linked so that commands are processed in a certain order. For example, LabVIEW tasks must be initialized and channels must be configured before the

acquisition loops can be started. Due to these features, the program can idle with a real-time display while module settings are changed, the heater is enabled or disabled, and data acquisition options are chosen as shown in FIGURE 50.

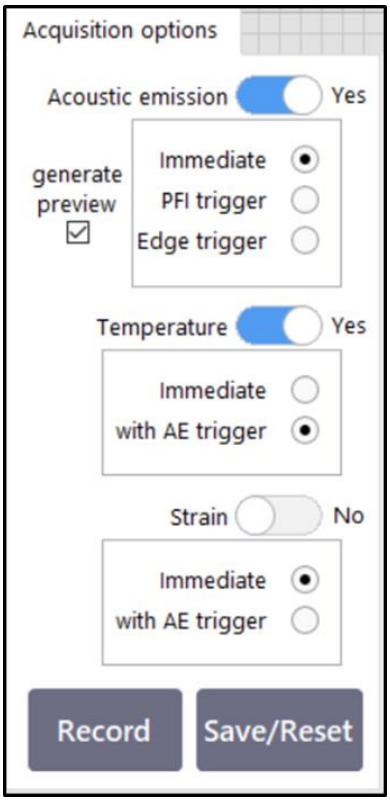

FIGURE 50: Data acquisition options on the LabVIEW program UI.

Being able to choose which type of data to record and how to trigger the acquisition gives the user flexibility to perform different types of experiments and easily carry out operational checks on the hardware. Resetting of the triggers after recording and saving enables the user to record multiple data sets without restarting the program, which would disrupt the PID controller for the build plate heater. Documentation has been written throughout the program for troubleshooting and with future users in mind.

CHAPTER 5: MORE EXPERIMENTS (2019)

The initial round of experiments demonstrated enough sensitivity in the acoustic emission measurement system to discriminate between the laser being inactive, the laser actively scanning on a bare substrate as well as on a single powder layer, and significant crack formation. To establish the baseline AE signal of a well-formed track, the substrate is preheated to avoid excessive cracking on the entire process map. Factors affecting the AE signal will be investigated by varying process parameters across a set of single tracks and evaluating the time- and frequency-domain characteristics of the recorded signals.

5.1 Preparation

For the new round of experiments, the entire original build stack in the AMMT was removed again and the improved instrumentation rig was installed directly on top of the build arm as shown in FIGURE 51.

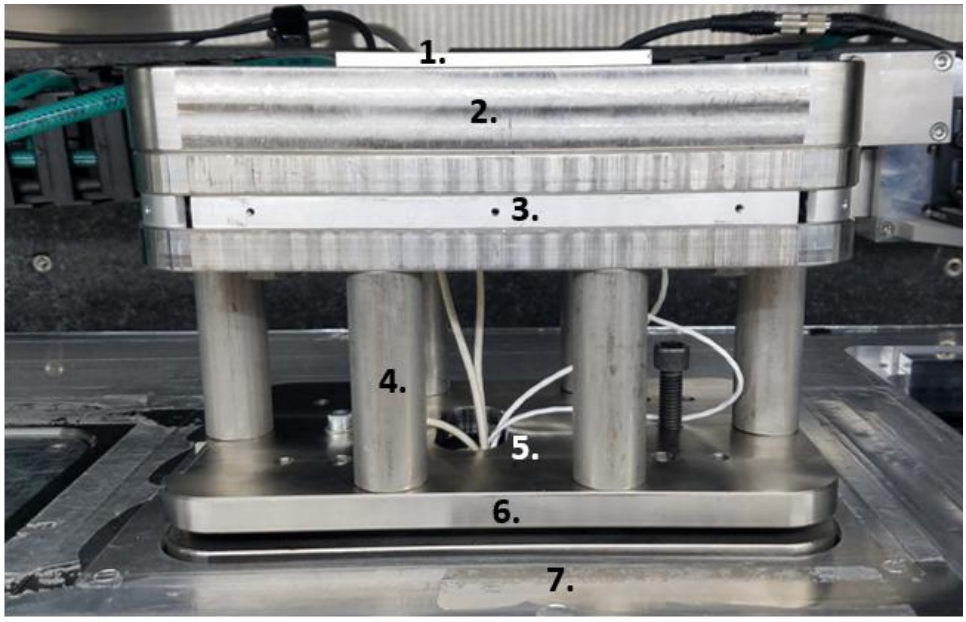

FIGURE 51: Improved instrumentation rig installed on build arm of AMMT.

The substrate (1) is installed from the top onto the heater-integrated build plate (2), which is attached to the seal assembly (3, felt seal not shown) by standard bolts from below. The spacers (4) allow room for instrumented bolts with longer heads to replace the standard bolts for future 3D builds. Cables (5) from the heater, AE sensor and RTD are fed through the dual plates (6) of the tilt mechanism and out through the bottom of the AMMT chassis (7). After lowering the rig into the build cylinder, the instrumentation is prepared as described in Chapter 4.1 and shown in FIGURE 52.

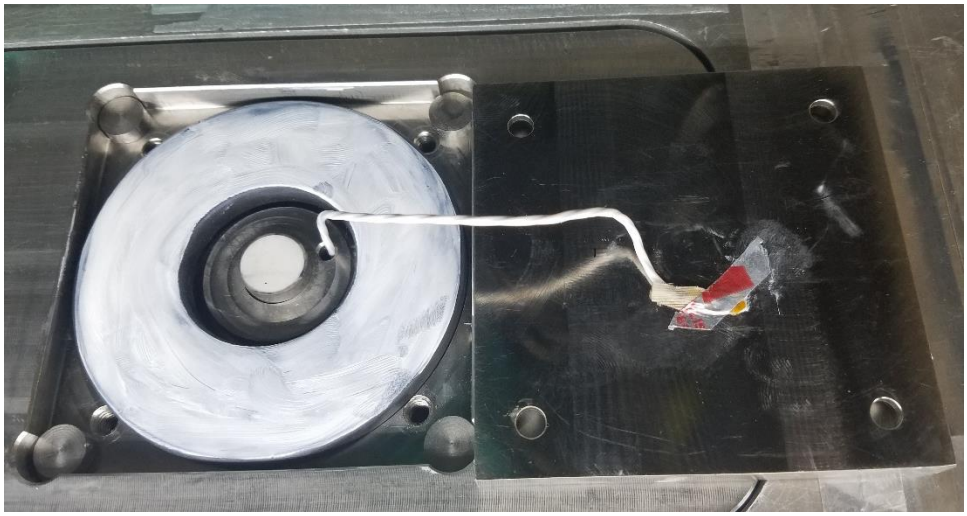

FIGURE 52: Ring heater, AE sensor and RTD ready for substrate installation.

With the substrate installed, the heater functionality and sensor responses are checked via the data acquisition software. Next, the substrate is leveled as described in Chapter 4.3 and then raised to the appropriate height corresponding to the desired laser spot size as described in Chapter 3.1. To prevent excess powder from falling into the heater cavity or down the build cylinder, aluminum tape is applied around the entire substrate and masking tape along the edges of the build plate as shown in FIGURE 53.

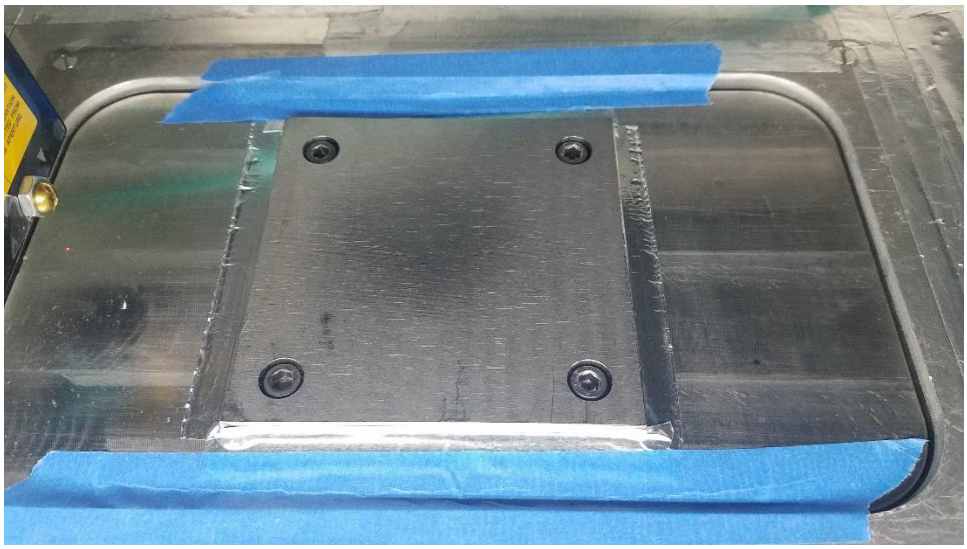

FIGURE 53: Substrate ready for powder spreading and laser scanning.

5.2 Preliminary scans

The initial approach for the new round of experiments is to first select a representative subset of datapoints from the original parameter space discussed in Chapter 3.3 and attempt to repeat the results while addressing the issues encountered in Experiment A and discussed in Chapter 3.6. The scan code was modified to create the tracks one at a time with at least 60 seconds between tracks, which gives the AE time to ring down and prevents it from affecting the next track's signal. To prevent excessive cracking in the single-layer Ti64 tracks, the substrate is pre-heated and maintained at 165 +1/-4 °C for the duration of the experiment. Since temperature is measured on the underside of the substrate and some heat is lost from the top surface of the bare substrate, the effective temperature of the top surface is 160 °C for this setpoint.

In addition to heating the substrate for the Ti64 scans, a second set of process parameter combinations was chosen for another material in case the heater did not function properly. Of the available powder and substrate materials, 17-4PH stainless steel was chosen for its relatively low thermal expansion coefficient (CTE) and relatively high

thermal conductivity. Materials with a high CTE and low thermal conductivity are more susceptible to solidification cracking (Yu, Rombouts, and Maes 2013), so the thermal properties of 17-4PH are advantageous to printing defect-free on an unheated substrate. In contrast to titanium or aluminum, NIST allows large batches of stainless powder to be used in the AMMT, which is necessary for future multi-layer builds. A parameter space was chosen as shown in FIGURE 54 by expanding the area around the process parameters used to create continuous single-layer 17-4PH tracks created on an unheated substrate.

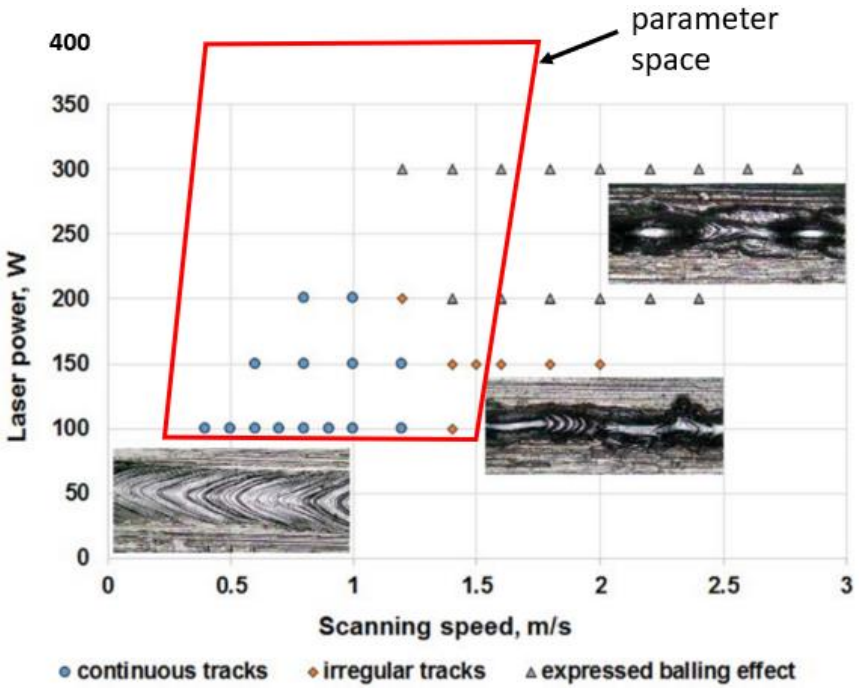

FIGURE 54: Adapted from process map for 17-4PH (Makoana et al. 2018).

It is expected that tracks created with non-ideal parameters will have more defects or cracking, which may be detectable in the AE signal like in Experiment A. TABLE 5 shows the parameter combinations chosen for the preliminary single-layer experiment, representing a wide array of P/V values within the defined parameter spaces.

TABLE 5: Subset of process parameters for preliminary experiments.

Ti64			17-4PH		
Power (W)	Speed (mm/s)	P/V (J/mm)	Power (W)	Speed (mm/s)	P/V (J/mm)
100	550	0.18	**100**	200	0.50
100	700	0.14	100	800	0.13
100	1400	0.07	100	1400	0.07
200	2500	0.08	**260**	300	0.87
260	850	0.31	260	900	0.29
260	1200	0.22	260	1550	0.17

However, the AE signals recorded during the Ti64 scans differed significantly from those of the unheated experiments in Chapter 3. No significant AE events were detected, and no cracking was observed for tracks created with any of the chosen process parameter combinations. In fact, only a short initial AE event was recorded for tracks created with linear energy densities below 0.16. For linear energy densities of 0.16 and above, the AE signal was continuous for the length of the track but did not reach amplitudes much greater than the noise level in the measurement setup and showed little to no ring down after the laser finished scanning, as shown in FIGURE 55.

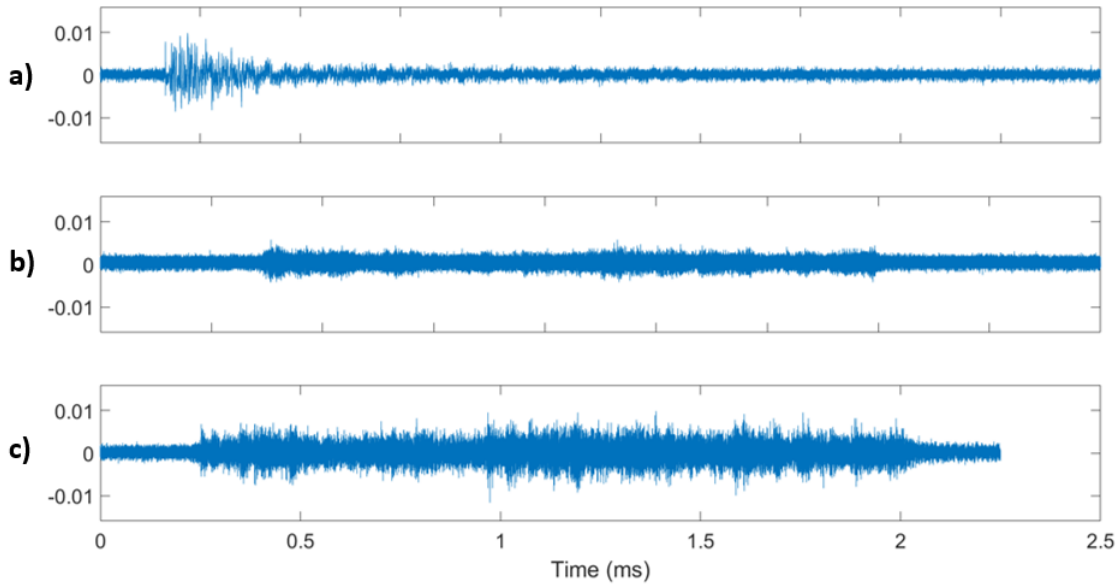

FIGURE 55: AE signal of tracks created with P/V of a) 0.08, b) 0.18 and c) 0.31.

5.3 Experiment 1 design

Due to the lack of continuous AE signals for tracks created with linear energy densities below 0.16, the process map was modified to exclude this zone and focus on process parameter combinations that are expected to generate continuous AE that can be analyzed. The solid triangular line in FIGURE 56 traces the new parameter space to be investigated, the dotted polygon denotes the original parameter space from Experiment A, the straight dashed line represents the boundary line of constant linear energy density and the curved dashed line traces the "smooth forming zone" (Wang, Dou, and Yang 2018) described in Chapter 3.6.

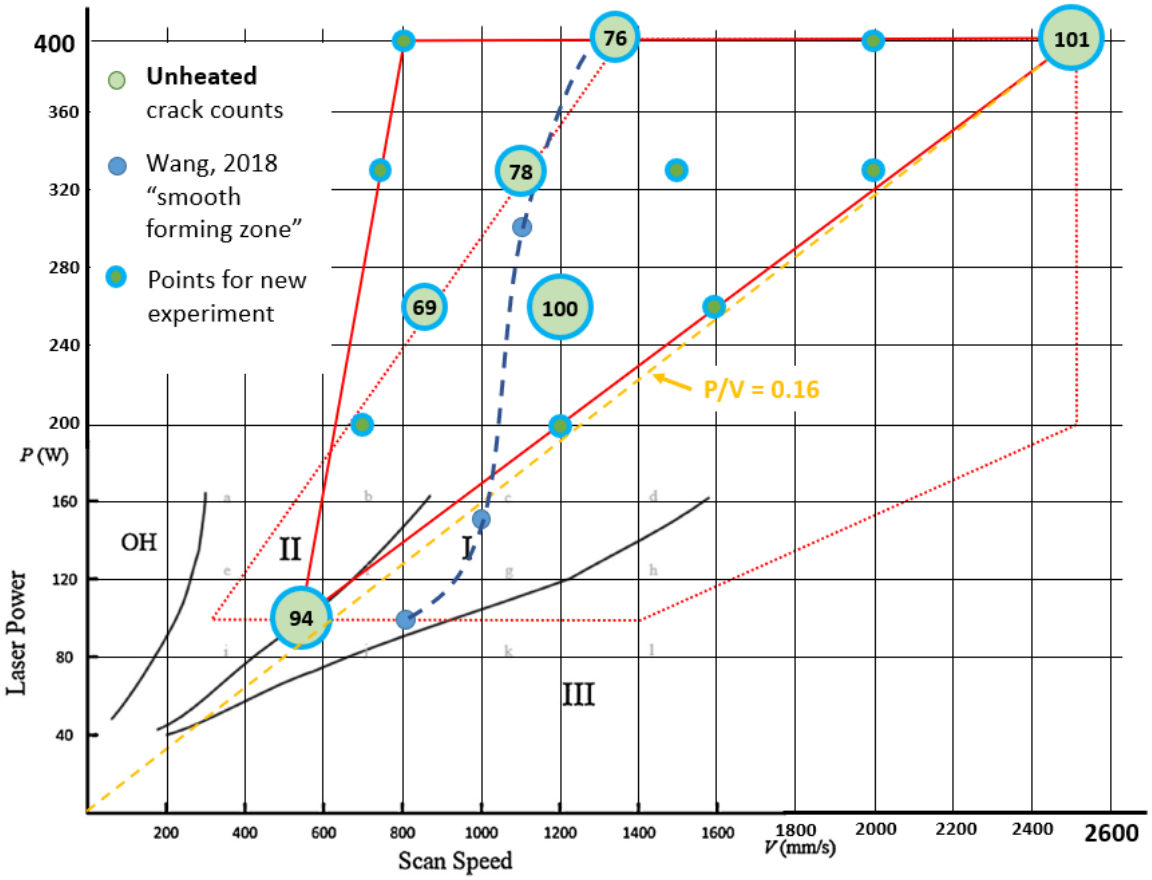

FIGURE 56: Process map for Experiment 1.

The 14 parameter combos, shown as outlined circles in the process map above, were used to create sets of 14 individual 10 mm long tracks. The list of process parameter values for each track is given in TABLE 6.

TABLE 6: Track-specific process parameters (laser power in W, scan speed in mm/s, linear energy density in J/s).

Track #	Power	Speed	P/V	Name
1	100	550	0.182	g1t1
2	200	700	0.286	g2t1
3	200	1200	0.167	g2t2
4	260	850	0.306	g2t3
5	260	1200	0.217	g2t4
6	260	1600	0.163	g2t5
7	330	750	0.440	g3t1
8	330	1100	0.300	g3t2
9	330	1500	0.220	g3t3
10	330	2000	0.165	g3t4
11	390	800	0.488	g4t1
12	390	1350	0.289	g4t2
13	390	2000	0.195	g4t3
14	390	2500	0.156	g4t4

Similar to Experiment A, a single scan direction was chosen for the 14 tracks which are again spaced 0.5 mm apart and grouped within pads which are repeated four times for averaging purposes. Since no AE ringdown was observed during the heated preliminary scans, only a 20-millisecond delay was added between tracks created on the heated substrate and a 1 second delay between tracks created at room temperature. The layout of the track pads and sets for Experiment 1 is shown in FIGURE 57.

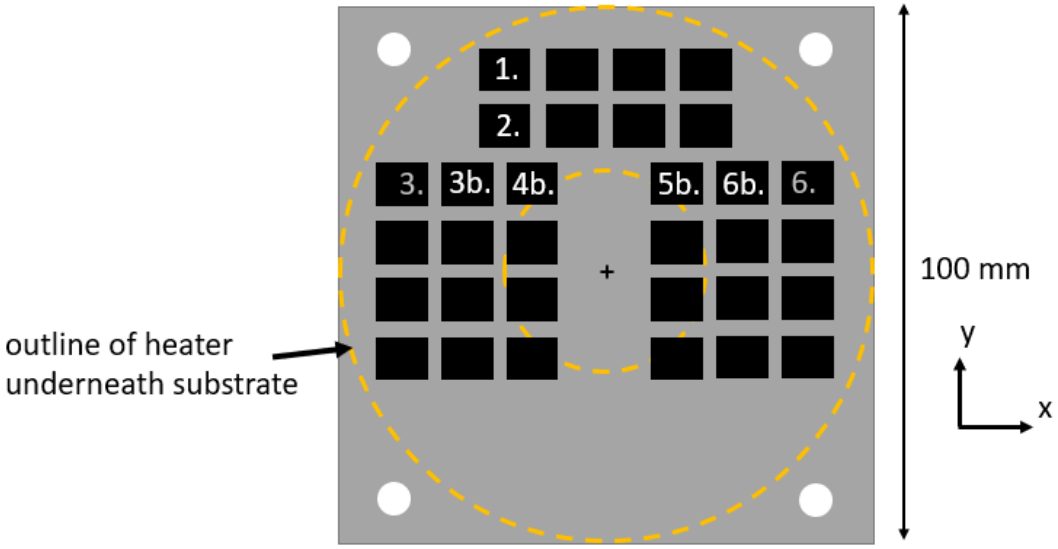

FIGURE 57: Pad layout for Experiment 1.

Due to a software error while scanning Set 3, the AE signal was not recorded for this set. Powder was also blown away during scanning from the area covered by Set 6, so many tracks in this set were incomplete. Because of these issues, the original layout for Experiment 1 was modified, shifting Sets 3-6 inwards and renaming them 3b-6b. TABLE 7 lists the process parameters corresponding to each set.

TABLE 7: Set-specific process parameters for Experiment 1.

Set #	Substrate temp. (°C)	Laser spot size (µm)	Substrate condition
1	25	85	bare
2	25	85	powder
3b	165	55	powder
4b	165	55	bare
5b	165	85	bare
6b	165	85	powder

5.4 Experiment 1 process

After applying thermal paste to the heater and RTD, and applying Magnaflux Sono 600 couplant to the AE sensor, a Ti64 substrate was installed and leveled as described in Chapter 4.3. Next, a single layer of Ti64 powder was spread using the AMMT's steel recoater blade moving at a constant 20 mm/s across the substrate in the

positive x-direction. The average layer thickness of 61 ±18 μm was determined by across tracing a line (1) across the substrate (2) and taking a height measurement every 10 mm using a Keyence laser displacement gauge (3), which was zeroed on a bare spot at the edge of the substrate.

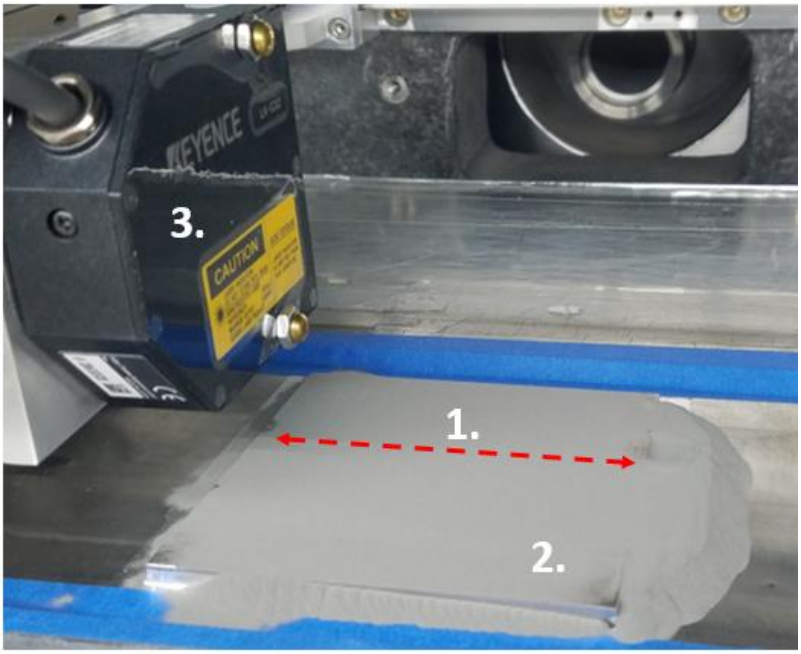

FIGURE 58: Powder layer thickness measurement.

While the laser displacement gauge has a resolution better than 1 μm, the measurement uncertainty depends on the sizes and distribution of the powder particles under the laser spot when the measurement is recorded. To prevent oxidation of the powder, a plexiglass enclosure is installed over the substrate and filled with argon gas via a diffuser. A sensor inside the enclosure monitors the oxygen level and an adjustable blower nozzle provides direct gas flow across the substrate as shown in FIGURE 59.

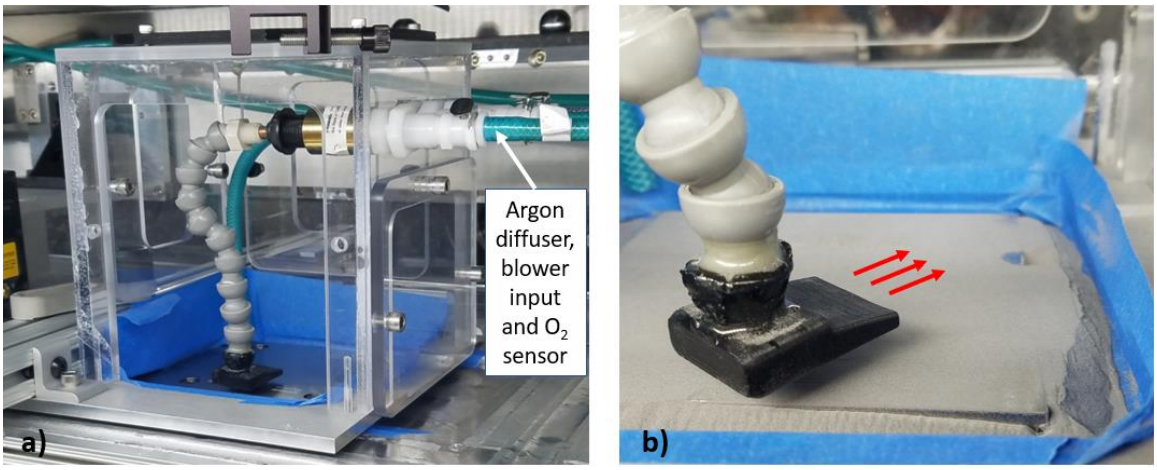

FIGURE 59: a) Enclosure positioned over substrate & b) Argon blower nozzle.

The LPBF process creates a plume of vaporized metal condensate rising from the melt pool, which scatters light from the laser beam and can lead to laser power attenuation, beam defocusing and generation of ejecta (Of et al. 2020). The argon blower nozzle is used to blow the plume away from the path of the laser beam. The nozzle was manually adjusted to be as close as possible to each set being scanned while keeping the gas flow parallel to the substrate. FIGURE 60 shows the approximate nozzle orientation with respect to the set being scanned, with dashed outlines representing the second nozzle position and corresponding pads.

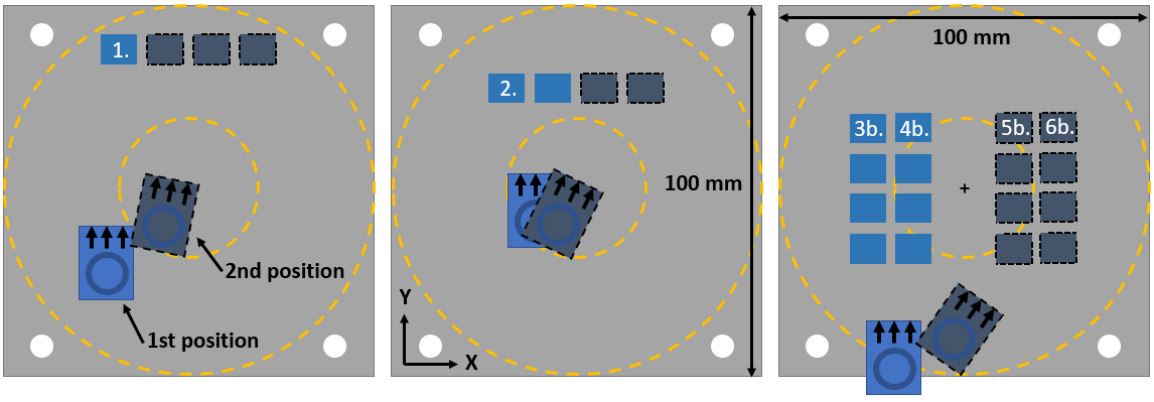

FIGURE 60: Approximate blower nozzle x-y orientations for each set.

Sets 1 and 2 were scanned one pad at a time, so the blower nozzle was able to be repositioned for better gas coverage. Due to time constraints, all four pads of the remaining sets were scanned back-to-back, so the nozzle was repositioned only once, between Sets 4b and 5b. The vertical distance between the nozzle and the powder layer was not measured but is estimated at 5 to 10 mm depending on the x-y position. The gas flow rate for the blower nozzle was set to 14 lpm, which is the maximum flow rate that did not disturb the powder bed.

5.5 Experiment 1 results

Confirming the results of the preliminary experiment in Chapter 5.2, most tracks created with P/V of 0.16 or greater generated some AE. The average baseline noise amplitude for both experiments is 0.002 (unitless) for reference in FIGURE 61 and FIGURE 62, and the RMS of the baseline noise is 7.3 RMS units after adjusting for the oscilloscope's gain and offset. The maximum signal-to-noise ratio (SNR) for tracks (heated or unheated) in Experiment 1 is around 10, much lower than the maximum SNR of Experiment A which exceeded 200 as demonstrated in FIGURE 61a.

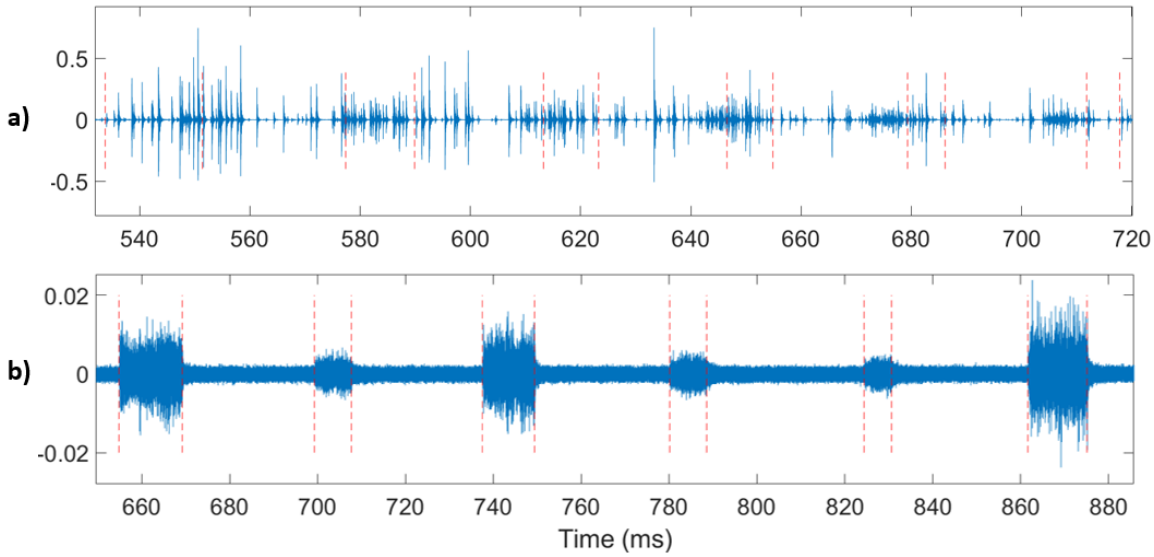

FIGURE 61: Set of six tracks from a) Exp. A and b) Exp. 1 (N*ote y-axis range*).

Comparing individual tracks made with identical process parameters, it is evident that the high amplitude AE events observed in Experiment A are no longer present in the new experiments. The comparison of an individual track (P = 260 W, V = 850 mm/s) from both Experiment A and Experiment 1 is shown in FIGURE 62, with the dashed line indicating where the laser becomes active.

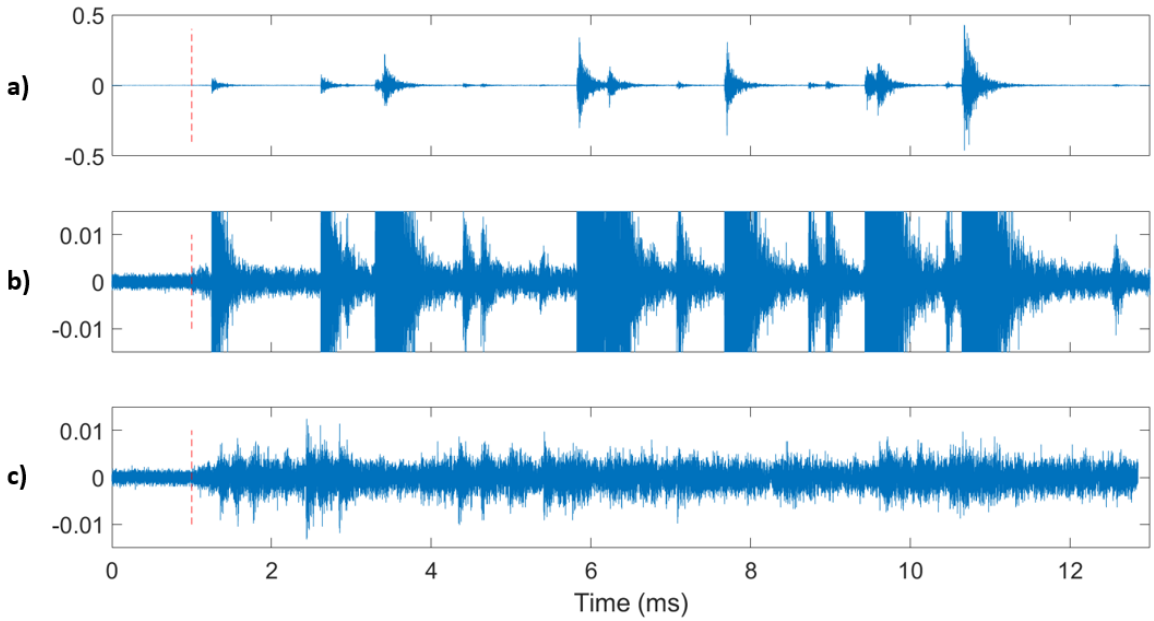

FIGURE 62: AE signal from a) Exp. A, b) Exp. A (zoomed) and c) Exp. 1.

Baseline noise level amplitudes before the laser activates are equal, which indicates that the experimental setup is repeatable and that any variations in the setup between experiments cannot solely account for the lack of significant AE events. Since no significant AE events were detected for any tracks in Experiment 1, the event counting method explained in Chapter 3.6, FIGURE 33 is not possible.

In lieu of counting cracking events, the RMS of the AE signal during laser operation is an alternative signal characteristic that was chosen to compare tracks created with different process parameter combinations. The entire recorded AE signal is first chopped into sections where the laser is active. Next, the AE signal RMS for each

section, or track, is calculated across its entire length. As shown in FIGURE 63, the AE signal RMS seems to slightly increase with laser power and is consistently higher for the smaller spot size. These trends are expected since more energy is being delivered by the laser beam in both cases. However, there is no clear correlation with laser scanning speed, as shown in FIGURE 64.

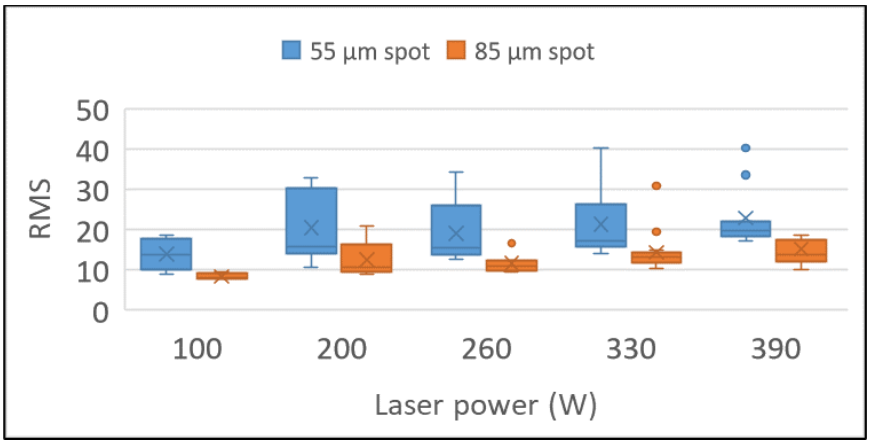

FIGURE 63: AE RMS values for Ti64 tracks created at 165 °C, sorted by power.

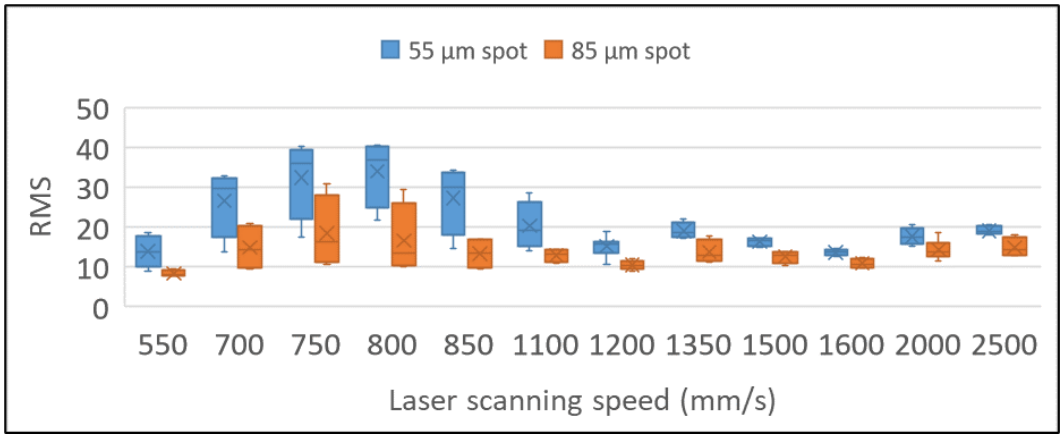

FIGURE 64: AE RMS values for Ti64 tracks created at 165 °C, sorted by speed.

Linear energy density combines the laser power and scanning speed into one parameter, and was expected to demonstrate a strong correlation with the AE signal RMS. As shown in FIGURE 65, although there seems to be some increase in the RMS at higher energy densities, the large spread of RMS values obscures any trend.

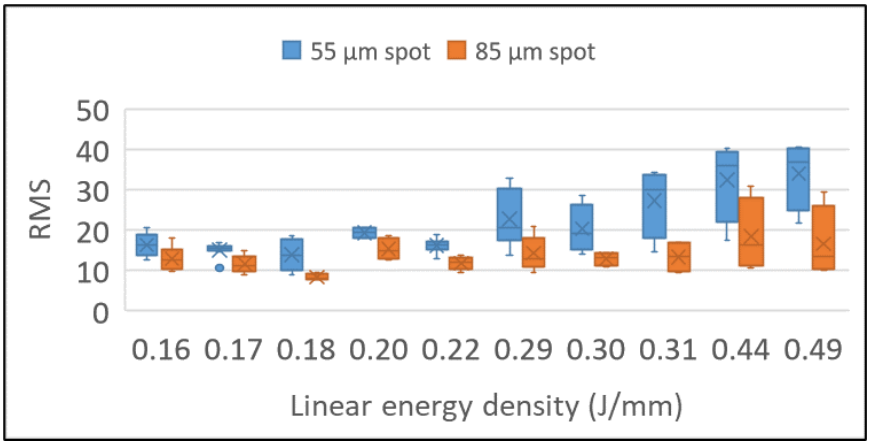

FIGURE 65: AE RMS values for Ti64 tracks created at 165 °C, sorted by energy density.

For reference in the following charts, all the pads (with 14 tracks each) are numbered as shown in FIGURE 66.

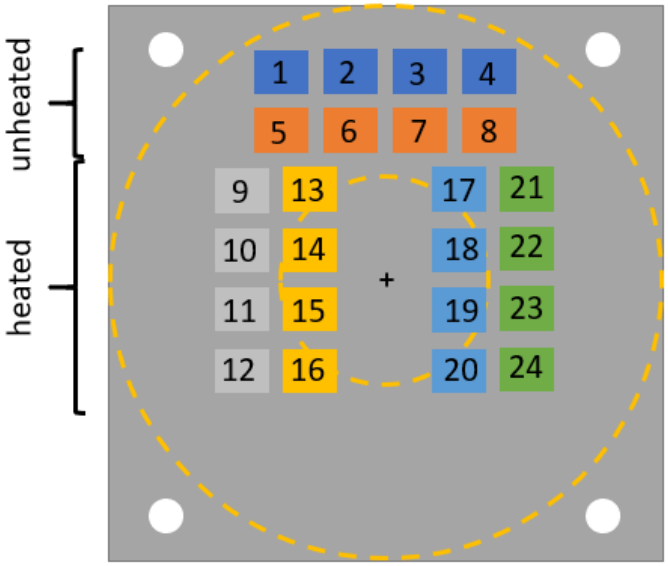

FIGURE 66: Pad ID numbers for Experiment 1.

Due to a software problem with the AMMT's controller, the laser did not activate for the last four tracks in Pads 1 and 5. This was remedied by reducing the commanded power from 400 W to 390 W for the appropriate tracks in all the other pads. In FIGURE 67, a decreasing trend in the RMS can be seen in Sets 3b to 6b (tracks 9 through 24) as the pads' distance to the blower nozzle decreases.

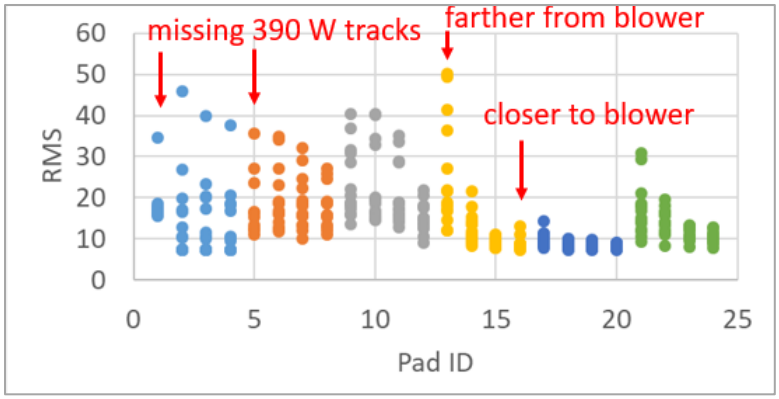

FIGURE 67: RMS values for all tracks, sorted by Pad ID.

The RMS values of all the tracks in each pad were averaged to compare overall variations from pad to pad within a set and variations between different sets. As shown in FIGURE 68, pads created on a single Ti64 powder layer generally have a higher mean RMS (denoted by an X) than pads created on the bare substrate. Higher mean RMS values also appear to correspond to lower substrate temperatures.

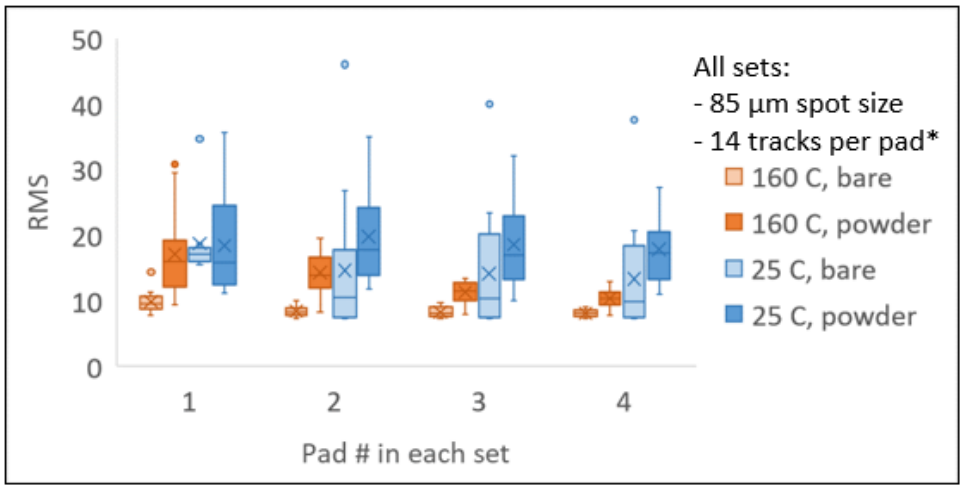

FIGURE 68: RMS values for all tracks in Sets 5b, 6b, 1 and 2 (in order).

*Caveat: Four 390 W tracks are missing from Pad 1 in both 25 °C datasets, which causes their means to be lower than they would otherwise be. As shown in FIGURE 69, the RMS of the AE signal is inversely related to the laser spot size, which is expected

since a smaller spot size at the same laser power results in a higher energy density at the substrate surface. Again, the presence of powder generally results in higher RMS values.

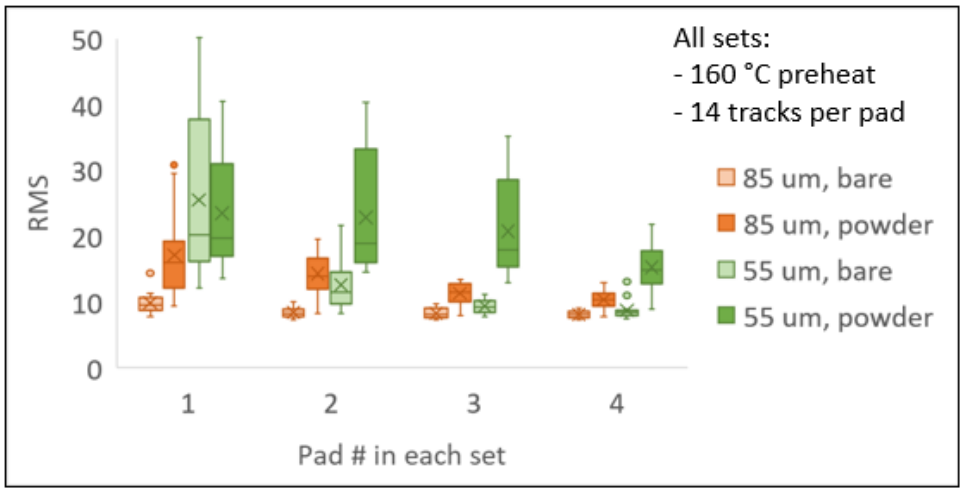

FIGURE 69: RMS values for all pads in Sets 5b, 6b, 4b and 3b (in order).

5.6 Experiment 2

Powder denudation is a common effect of the LPBF process and occurs when powder particles are blown away from the melt path of an active laser beam (Khairallah et al. 2016). Since the RMS of the AE signal changes with the presence of powder as observed in Experiment 1, the second experiment was designed to investigate this effect. Varying the laser power and speed results in varying amounts of powder denudation (Matthews et al. 2016), so a hypothesis was formed that the AE signal strength changes with the amount of denudation.

Sets 3b and 6b from Experiment 1 were chosen to be repeated for the purpose of recording the amount of denudation that occurs for each track. Set 2 was repeated to confirm the relationship between AE signal RMS and substrate temperature. Set 1 was partially repeated to investigate the effects of the blower nozzle. The layout of the track pads and sets for Experiment 2 is shown in FIGURE 70.

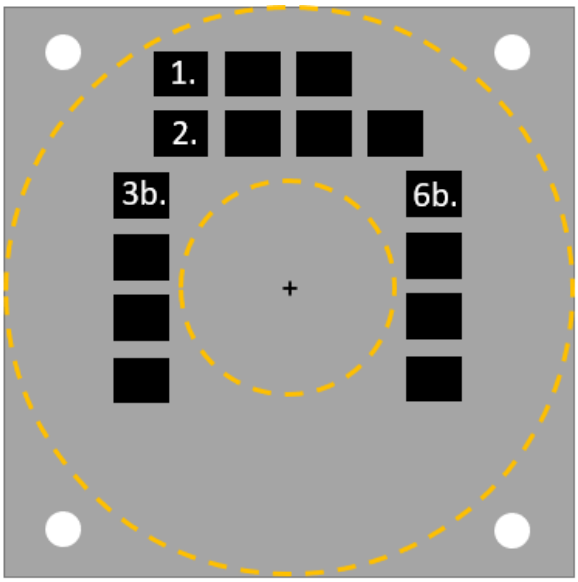

FIGURE 70: Pad layout for Experiment 2.

After leveling the new substrate and spreading a single layer of powder, all tracks were created as follows. For Set 1, the first pad was created without the presence of argon gas. For the second pad, the enclosure box was filled with argon and the blower nozzle aimed directly at the pad with a flowrate of 30 scfh. The third pad was created after the box was filled with argon, but with the blower nozzle inactive. For Sets 2, 3b and 6b, the blower nozzle was positioned similar to the arrangement shown in FIGURE 60. TABLE 8 lists the controlled process parameters corresponding to each set.

TABLE 8: Set-specific process parameters for Experiment 2.

Set #	Substrate temp. (°C)	Laser spot size (µm)	Substrate condition	Notes
1 - Pad1	25	85	bare	no argon
1 - Pad2	25	85	bare	box & blower
1 - Pad3	25	85	bare	box only
2	25	85	powder	
3b	165	55	powder	
6b	165	85	powder	

The mean AE signal RMS of Set 1, Pad 1 was about 50% higher than the other pads in the set, as expected for laser welding in a non-inert environment (He, Zhao, and

Niu 2018) The mean RMS values for Pads 2 and 3 of Set 1 did not significantly differ, but both pads had higher RMS values than the same pads from Experiment 1. This trend continues as shown in FIGURE 71, where mean RMS values for Experiment 2 pads are consistently higher than corresponding pads from Experiment 1, and RMS values decrease approaching the blower nozzle within each set. *Caveat: Four 390 W tracks are missing from Pad 1 in the 25 °C dataset from Experiment 1, which causes its mean to be lower than it would otherwise be.

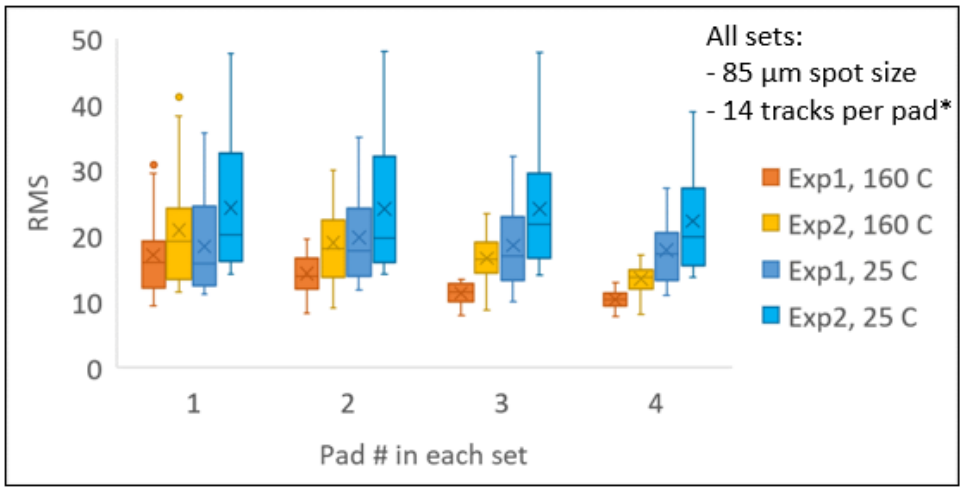

FIGURE 71: Cross-experiment comparison of RMS values for all pads in Sets 3b and 6b.

A height measurement trace, as described in Section 5.4, was taken across the centerline of the substrate after creating all sets of tracks. The measurement was repeated on the bare substrate after carefully removing the remaining loose powder. The sum of the two measurements gives the effective powder layer thickness, which was found to be up to two times the nominal 60 µm layer thickness due to deviations in the flatness of the substrate. The process of grinding the substrate results in an astigmatic top surface, which can be visualized as a potato chip. Flatter substrate top surfaces and more thorough powder layer thickness measurements are planned for future experiments.

Images of powder denudation were recorded after all tracks were created, but before height measurement of the bare substrate. As shown in FIGURE 72, a 10-megapixel Basler CMOS camera (1) with 10x macro zoom lens (2) was installed in the AMMT along with a flat, silver-coated mirror (3) which allows images to be recorded perpendicular to the substrate's top surface (4). Linear blue-light LED clusters were also installed to provide bright-field (5) and dark-field (6) illumination.

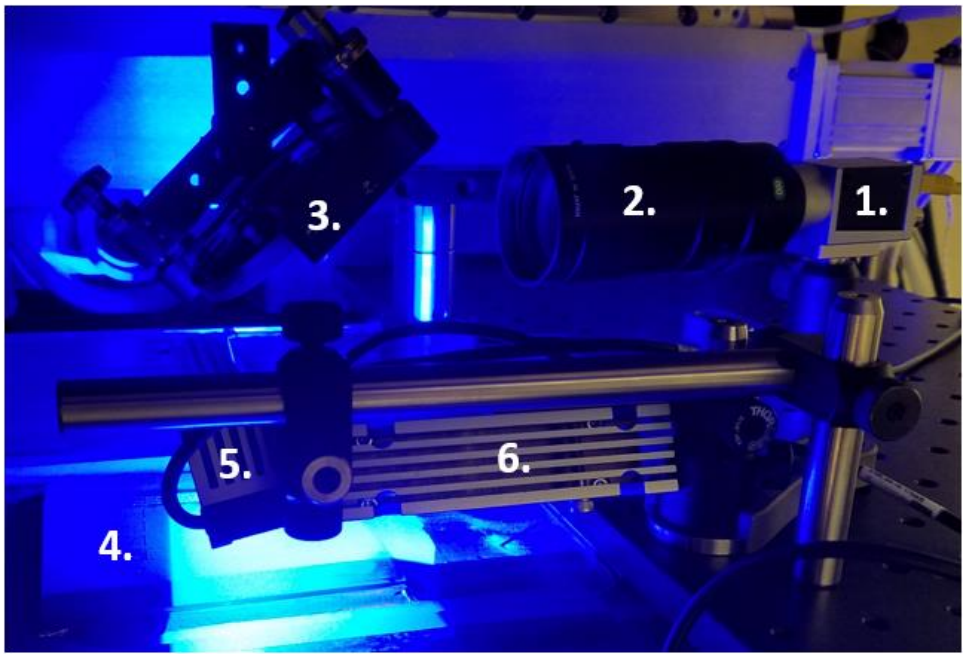

FIGURE 72: Denudation imaging setup above substrate in AMMT.

The bright-field LED cluster was adjusted to be almost parallel to the camera's beam path but had to be slightly tilted so the LED housing did not enter the frame. The dark-field LED cluster was adjusted to be as parallel as possible to the substrate's top surface, with the light coming from a direction perpendicular to the tracks. A combination of bright- and dark-field illumination was the best way to reveal the denudation occurring around the tracks. However, the 500 μm track spacing, based on

similar work in the literature (Matthews et al. 2016), was not enough to keep the denudation zones from overlapping, as shown in FIGURE 73.

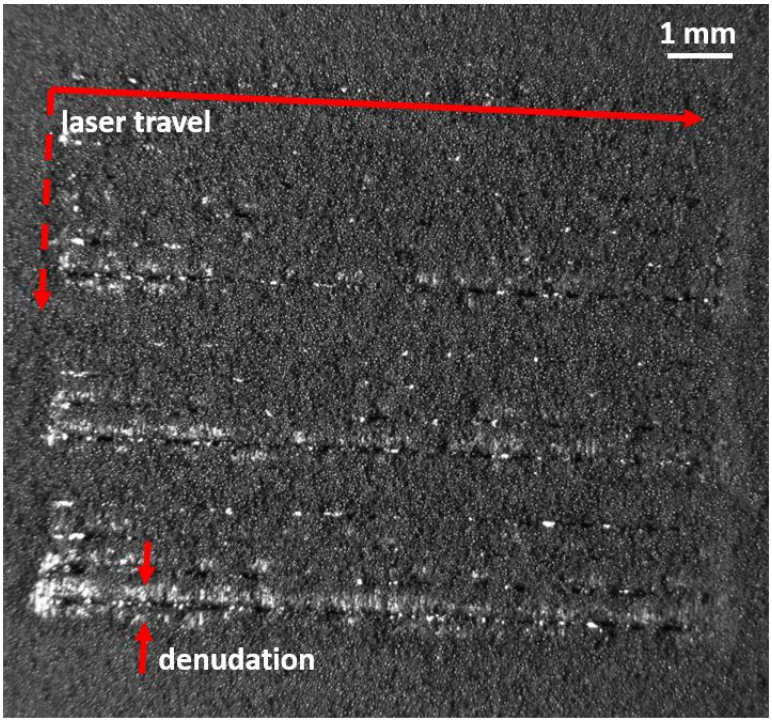

FIGURE 73: Image of Set 2, Pad 4 created on a single Ti64 powder layer.

From a visual inspection, pads created first and farthest from the blower nozzle have more loose powder coverage than pads created last and closest to the nozzle, as shown in FIGURE 74.

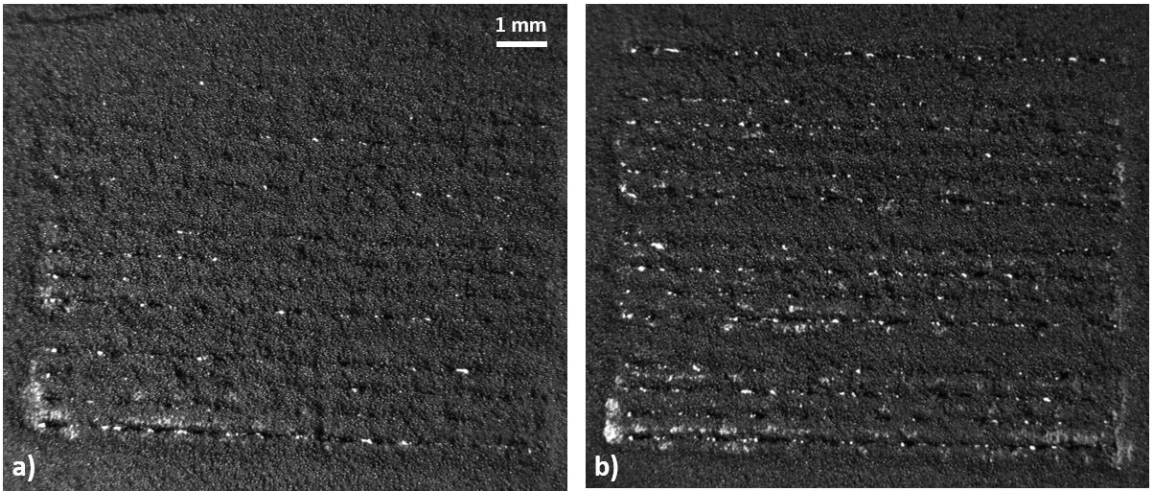

FIGURE 74: Images of Set 6b, a) Pad 1 far from and b) Pad 4 close to the blower.

In addition, tracks created closer to the blower nozzle show a greater balling effect and seem to be less continuous than tracks in pads farthest away, as shown in FIGURE 75. However, this effect may be caused by variations in the powder layer thickness rather than variations in proximity to the blower.

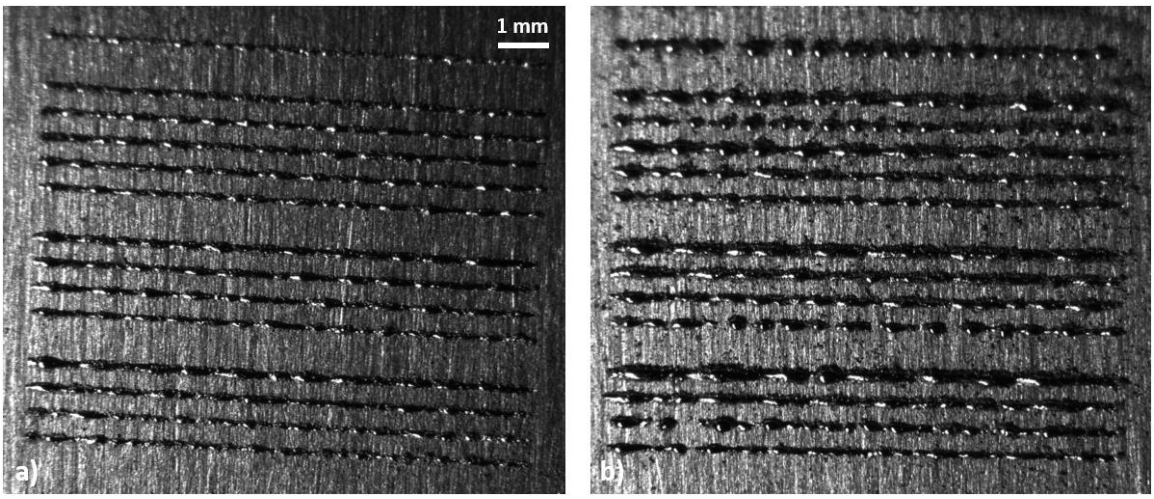

FIGURE 75: Images of Set 3b, a) Pad 1 far from and b) Pad 4 close to the blower.

5.7 Experiment 3

The third experiment incorporates four major changes: a track layout optimized for denudation imaging, a flatter top substrate surface, a more consistent illumination configuration and no gas flow from the blower nozzle. Still using the same 14 parameter sets listed in TABLE 6, all tracks were oriented perpendicular to the original direction with the spacing increased from 0.5 mm to 2 mm. Four pads containing 14 tracks each were repeated across the top half of the substrate as shown in FIGURE 76.

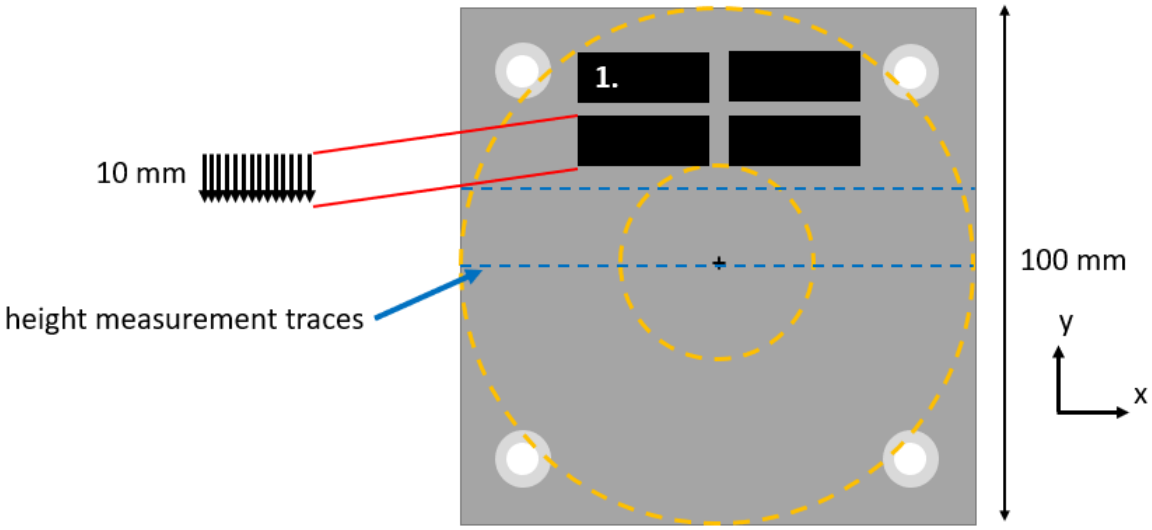

FIGURE 76: Pad layout for Experiment 3.

All tracks in this set of four pads were created with an 85 µm laser spot size on a single Ti64 powder layer preheated to 160 °C. This layout allows wider spacing between tracks to prevent denudation zones from overlapping and requires the camera to be repositioned only once. The reground substrate bows less than 50 µm, as demonstrated by the height measurements shown in FIGURE 77.

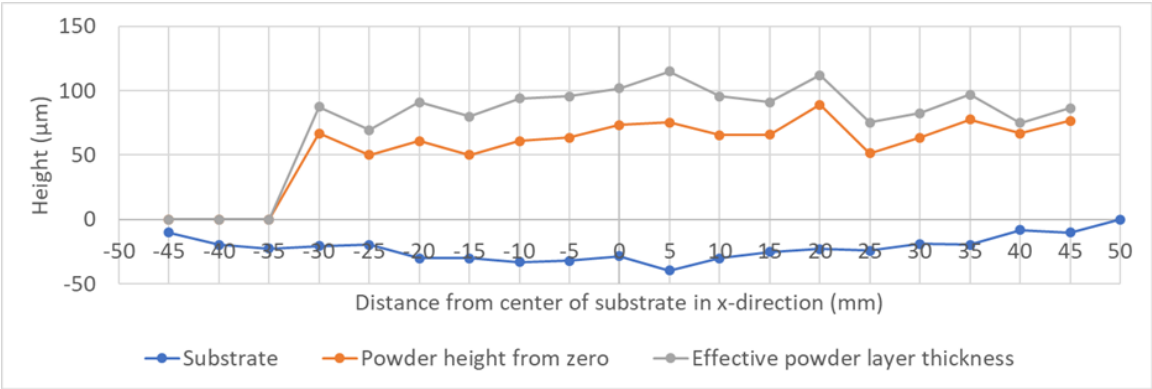

FIGURE 77: Height measurement traces across the center of the substrate.

A software error resulted in no AE data being recorded for Pad 1. Compared to Experiments 1 and 2, the average RMS values for the remaining pads in Experiment 3 do

not follow the previous decreasing trend, as shown in FIGURE 78. Possible explanations include the different pad layout and absence of the blower nozzle in Experiment 3.

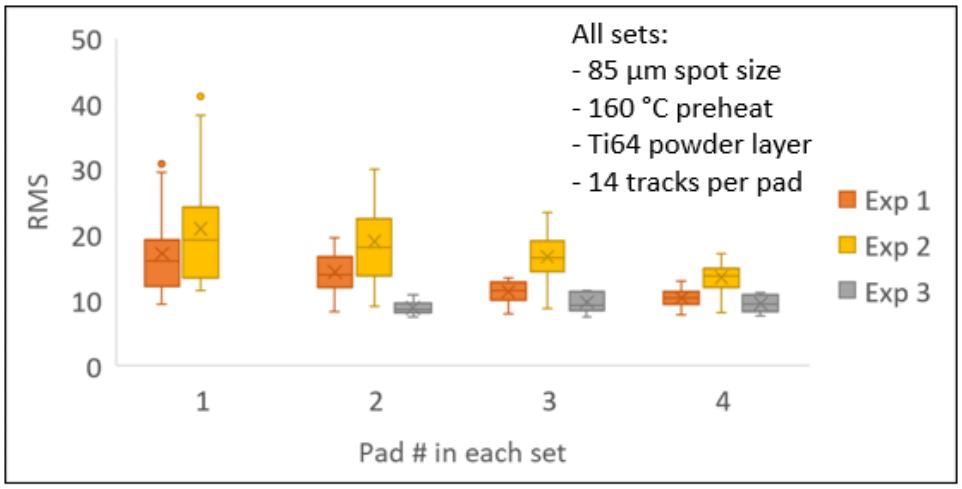

FIGURE 78: Cross-experiment comparison of RMS values for selected sets.

Due to the increased track spacing, only 5 tracks can be imaged at a time. As shown in FIGURE 79, the same CMOS camera (1), 10x zoom lens (2) and dark-field LED cluster (3) from Experiment 2 were used to record the images. Instead of using the mirror, the camera was mounted perpendicular to the substrate's top surface, with bright-field illumination provided by a ring light (4) mounted as close as possible to the zoom lens' objective.

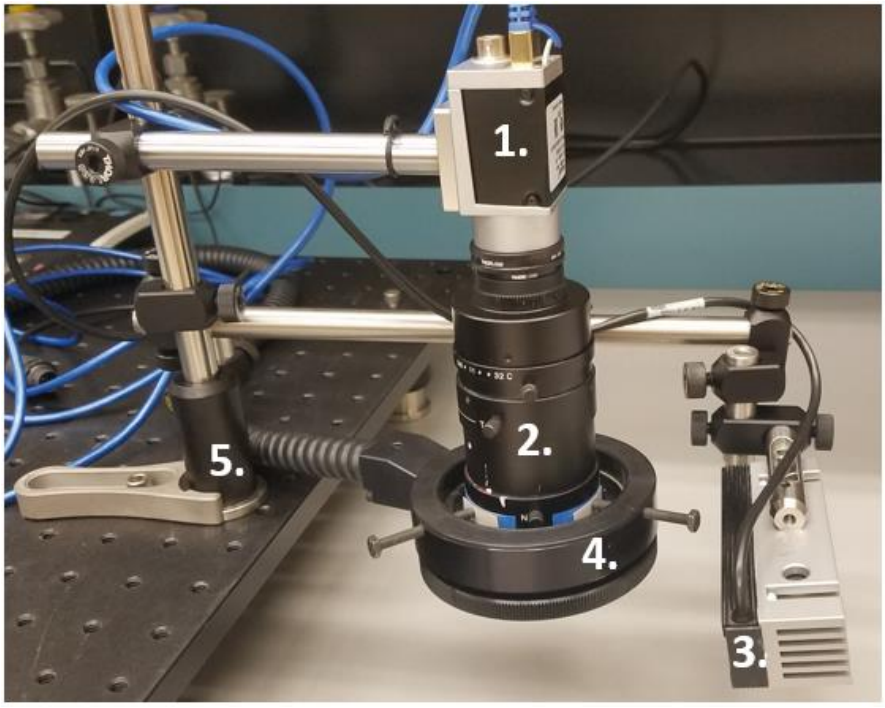

FIGURE 79: Denudation imaging setup for Experiment 3.

All the components in this configuration are physically connected to a common mounting post (5), which allows more consistent images when relocating the camera over the next row of pads. Images were recorded with dark field and bright field illumination separately, as shown in FIGURE 80 and FIGURE 81. Although the dark field images indicate areas of denudation, quantifiable measurements of the denudation widths could not be extracted from this data.

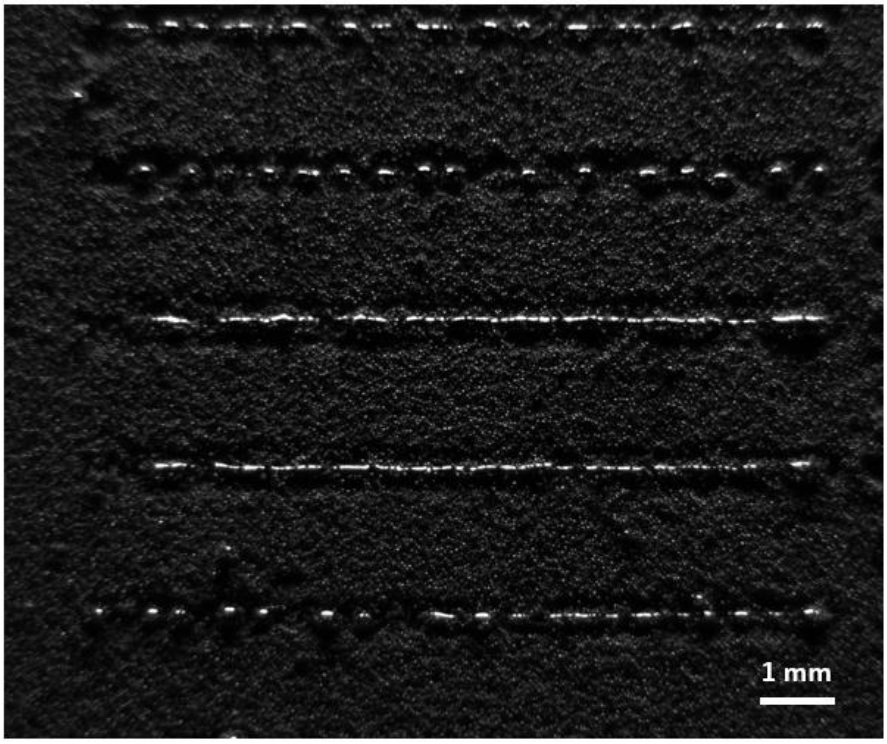

FIGURE 80: Dark field image of Pad 4, Tracks 9-13.

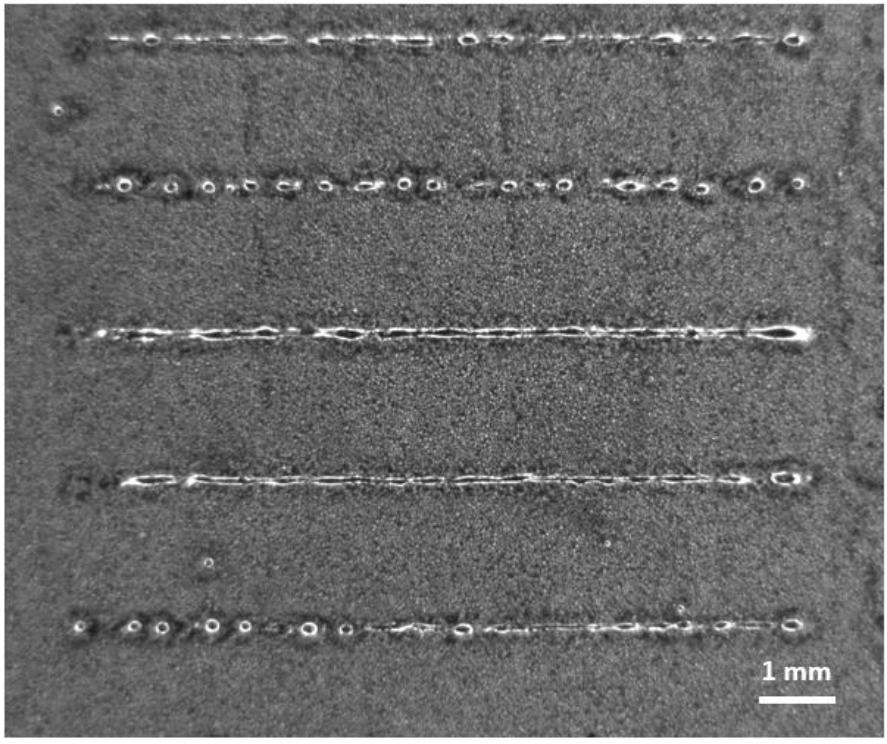

FIGURE 81: Bright field image of Pad 4, Tracks 9-13.

While denudation was hard to distinguish, the ring light illumination method worked well in revealing the shape of the tracks after removing loose powder, as shown in FIGURE 82. Tracks created with higher energy densities are wider and continuous, while tracks created with lower energy densities show more balling effects.

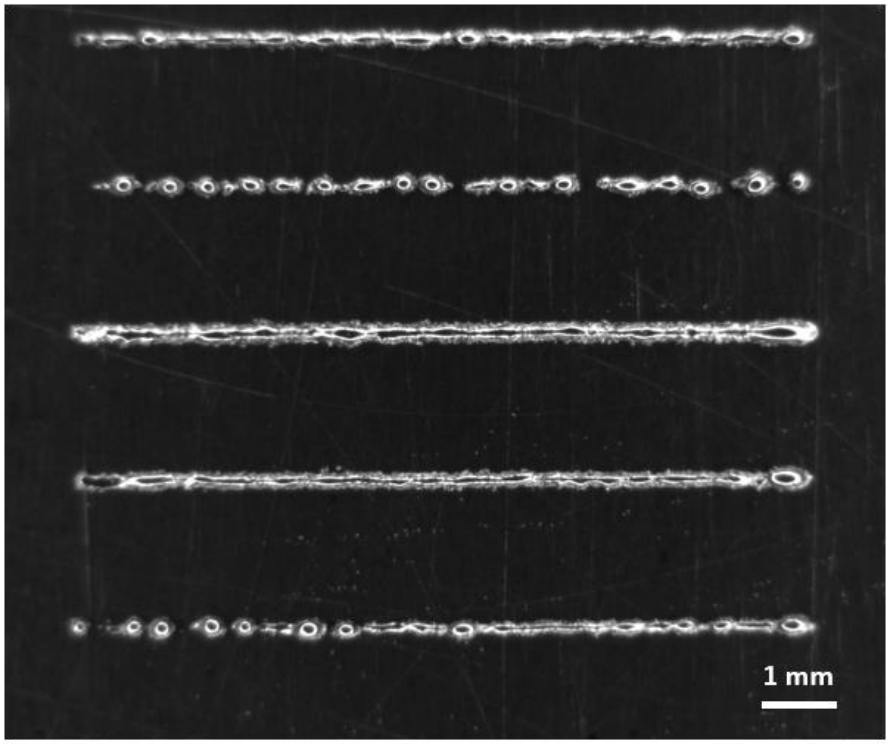

FIGURE 82: Bright field image of Pad 4, Tracks 9-13 with powder removed.

It was discovered later that the wrong beam splitter was unintentionally left in the AMMT for this experiment, which resulted in a much larger laser spot size than expected. A larger spot size at the same power means lower energy density, which could result in the observed discontinuous balling effect.

5.8 Experiment 4

The goals of the fourth experiment are to improve image quality and quantify denudation so it can be compared to the AE signal characteristics for each track. The tracks were laid out with the same orientation and spacing as in Experiment 3. Two sets

of 3 pads, each with the same 14 tracks listed in TABLE 6, were laid out as shown in FIGURE 83. Set 1 tracks were created first with an 85 µm laser spot size on a single Ti64 powder layer preheated to 160 °C, followed by Set 2 on the bare substrate reheated to 160 °C after loose powder removal.

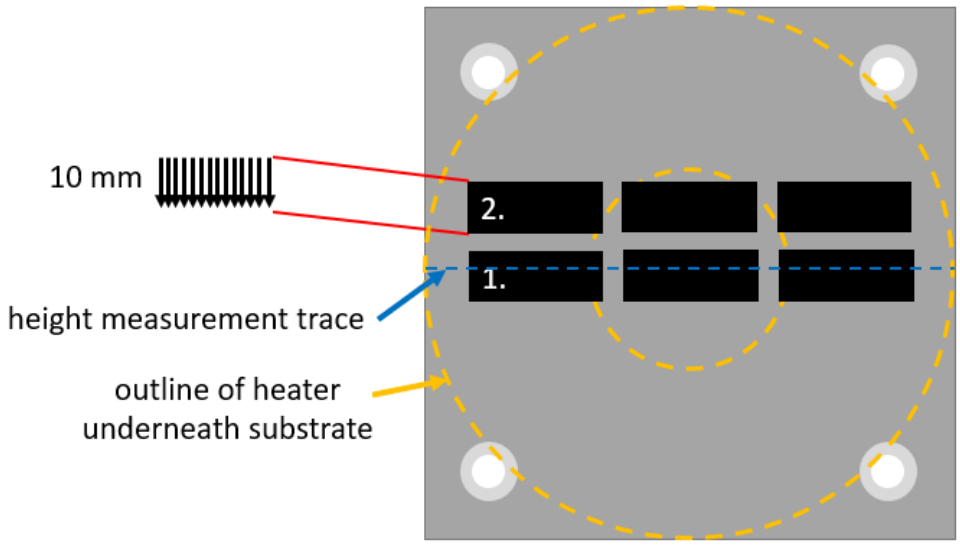

FIGURE 83: Pad layout for Experiment 4.

A measurement trace was taken across the center of the substrate after the powder layer was spread. The effective powder layer thickness over the entire area to be scanned was 59 ±20 µm, the closest so far to the nominal value of 60 µm. As shown in FIGURE 84, mean RMS values are slightly, but not significantly, higher in the presence of powder. However, cross-experiment correlation is not good, which could mean that the location of the pads relative to the AE sensor affects the AE signal strength more strongly than expected.

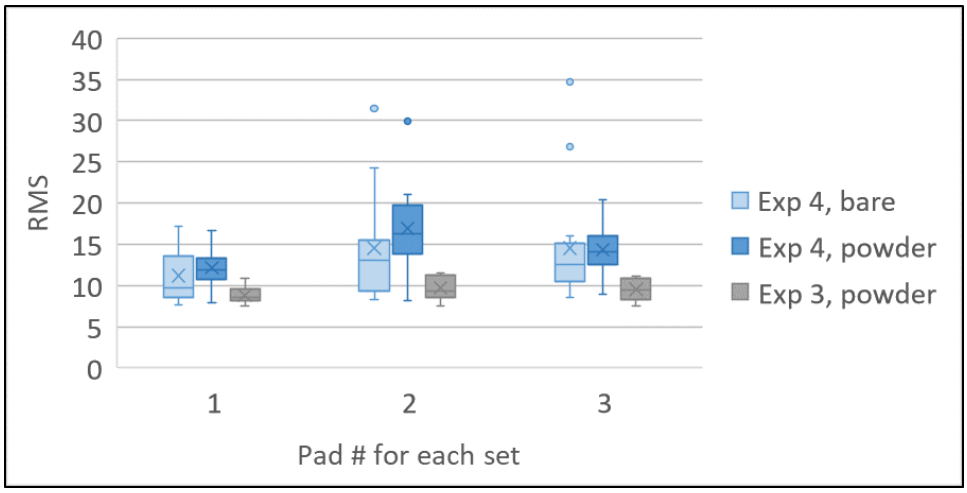

FIGURE 84: Cross-experiment comparison of RMS values for selected sets.

Tracks with low, medium and high linear energy densities were selected to be compared across all pads of Set 1 in Experiment 4 to investigate the effect of proximity to the AE sensor. As shown in FIGURE 85, a slightly increasing trend in RMS values could be inferred as the track's proximity to the sensor increases. However, more data is needed as the RMS values of the tracks with P/V = 0.49 are widely scattered.

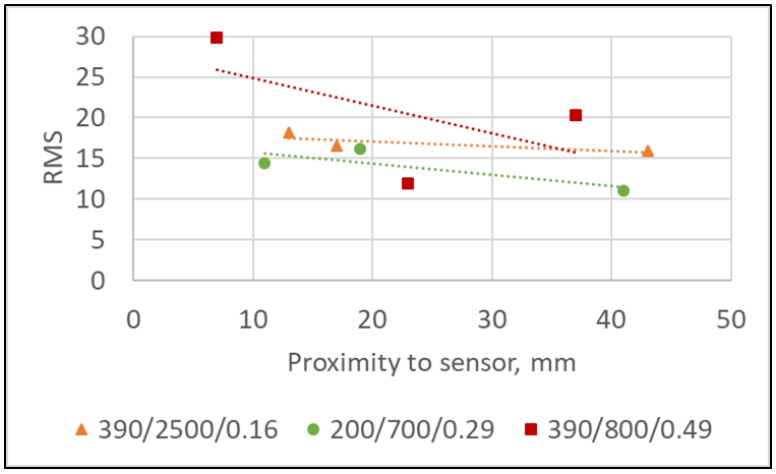

FIGURE 85: Comparison of RMS values relative to track's proximity to AE sensor.

Since the ring light from Experiment 3 did not provide good illumination for measuring denudation, the bright field illumination was changed back to the linear blue-light LED cluster from Experiment 2. As shown in FIGURE 86, a common mounting

post (1) was used to suspend the CMOS camera (2), macro zoom lens (3), bright field (4) and dark field (5) illuminators over the top surface of the substrate (6).

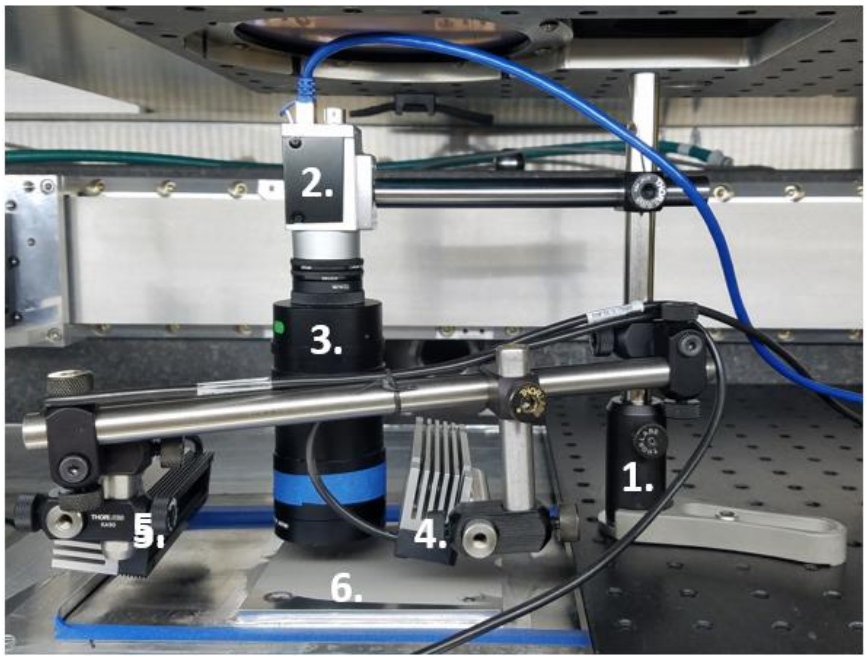

FIGURE 86: Denudation imaging setup for Experiment 4.

As shown in FIGURE 87, the combination of bright and dark field illumination provides the best image and allows an estimate of the powder denudation zone width to be obtained. There was no discontinuous balling observed for any tracks in this experiment, although the laser power and scanning speed for each track are identical to those in Experiment 3, which confirms that the balling effect resulted from using a larger laser spot size.

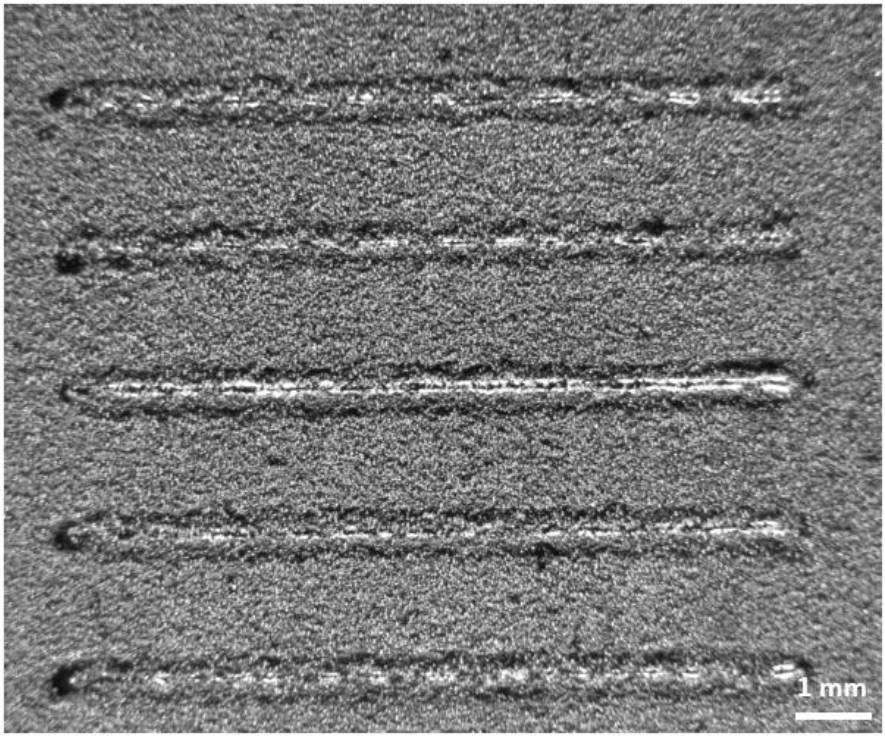

FIGURE 87: Combination bright & dark field image of Pad 2, Tracks 9-13.

Although the denudation zone widths seem to vary slightly with different laser powers and energy densities as shown in FIGURE 88, the zones are still not defined clearly enough to be measured more rigorously.

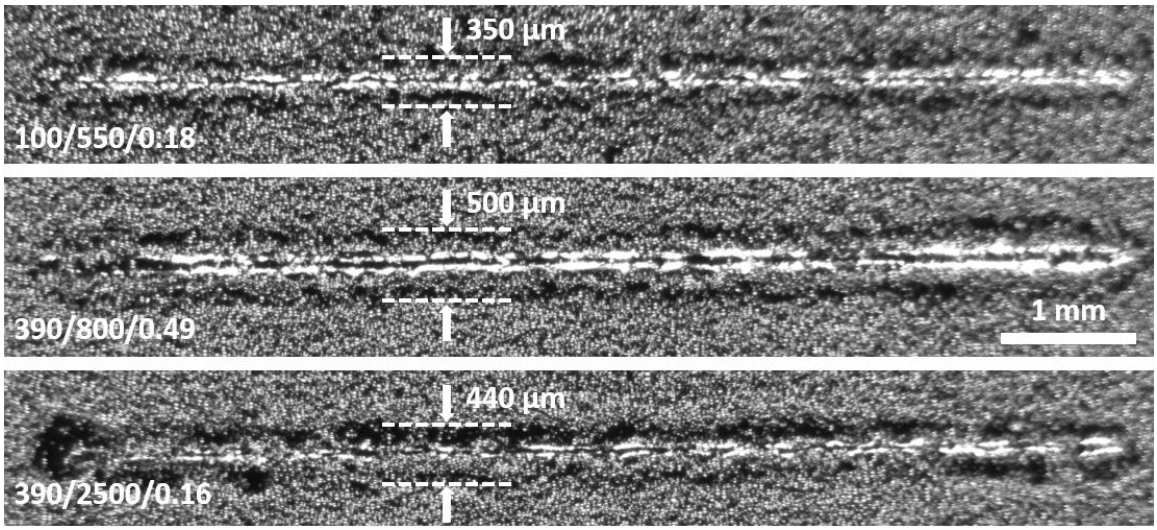

FIGURE 88: Denudation zone width estimations for selected tracks in Set 1, Pad 2.

5.9 Experiment 5

With limited time remaining for access to the AMMT, the last experiment was designed to provide a repeatability check and additional data for future analysis. The layout, orientation and location of the two sets from Experiment 4 were repeated. In addition, three more sets of four pads were added in the locations shown in FIGURE 89. The design and parameters for these pads is discussed later in this section. All tracks were created on a single Ti64 powder layer, with a 60 µm nominal thickness, using a Ti64 substrate preheated to 160 °C in a non-pressurized argon environment.

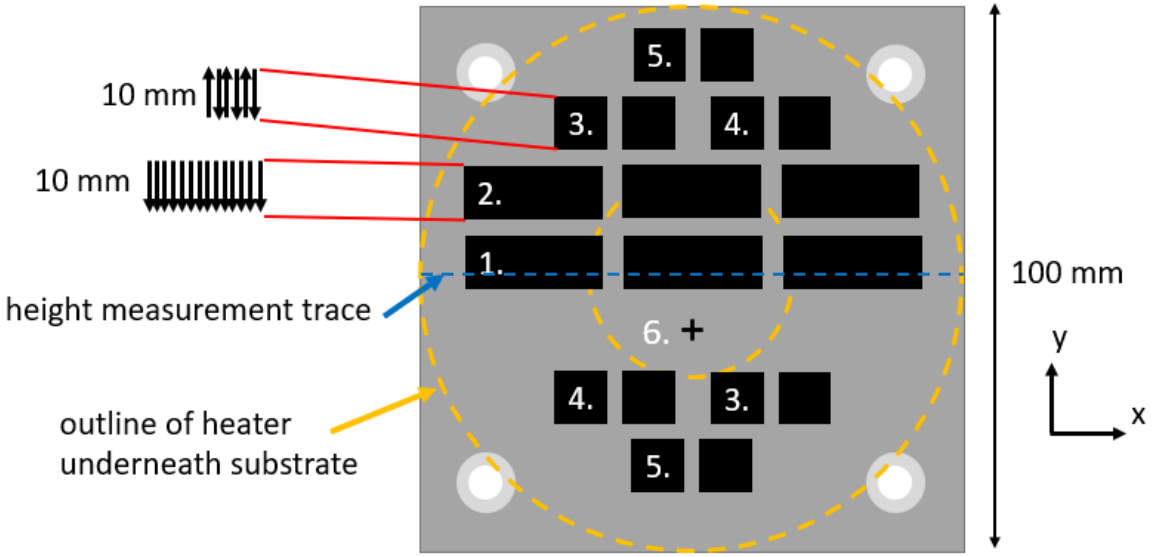

FIGURE 89: Pad layout for Experiment 5.

All conditions must be kept constant for a good repeatability measurement, so the denudation imaging setup from the previous experiment was not modified. After a reground substrate with a bow of 40 µm was installed, powder was spread and measured as usual. The effective powder layer thickness measurements across the center of the substrate matched more closely for Experiments 4 and 5 than any previous experiment. As shown in FIGURE 90, there seems to be good agreement between Experiment 4 and 5

for AE RMS values of tracks created on a layer of powder, which could indicate that these were the most well-controlled experiments so far.

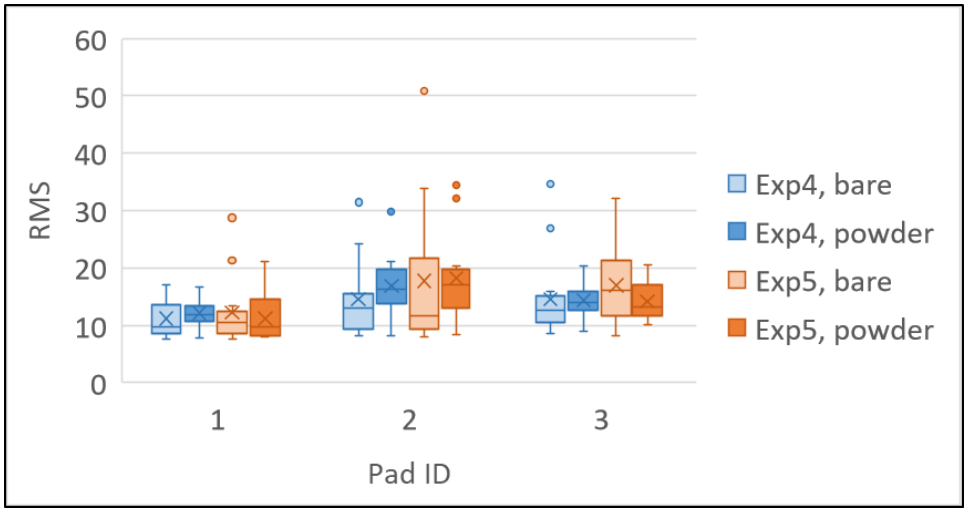

FIGURE 90: Cross-experiment comparison of RMS values for Sets 1 and 2 (in order).

However, there is not good agreement between experiments for AE RMS values of tracks created on the bare substrate, and bare tracks do not have significantly lower RMS values than tracks on powder like in Experiment 1. As shown in FIGURE 91, the powder denudation images recorded for Experiment 5 appear to be similar to the images recorded for Experiment 4, which suggests similar powder bed conditions between the experiments.

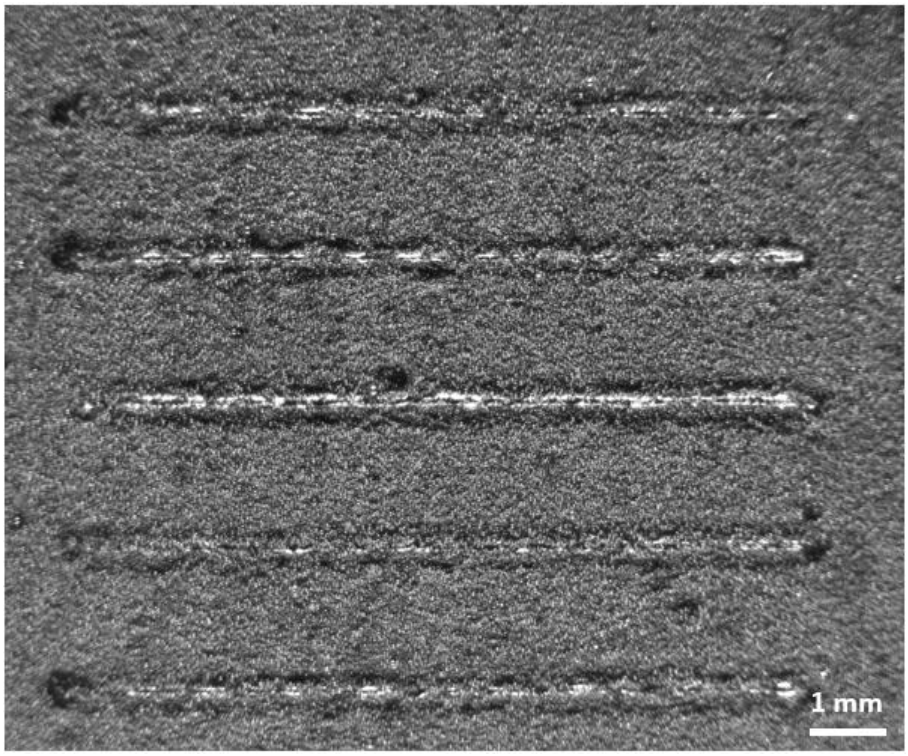

FIGURE 91: Combination bright & dark field image of Pad 2, Tracks 9-13.

Sets 3 to 5 consist of 10 mm long tracks scanned in alternating directions and spaced with a 20% overlap of the predicted track width. The goal of the alternating, overlapping scan strategy is to create pads that are more representative of a real-world application than single tracks (Carter et al. 2014). TABLE 9 lists the process parameters used to create all twelve pads in Sets 3 to 5.

TABLE 9: Set-specific process parameters for Experiment 5 (laser power in W, scan speed in mm/s, linear energy density in J/s).

Set #	Power	Speed	P/V
3	390	2500	0.16
4	260	850	0.31
5	390	800	0.49

The four pads in each of these sets are numbered left to right, with the first pad in each set located at the top of the substrate as shown in FIGURE 92.

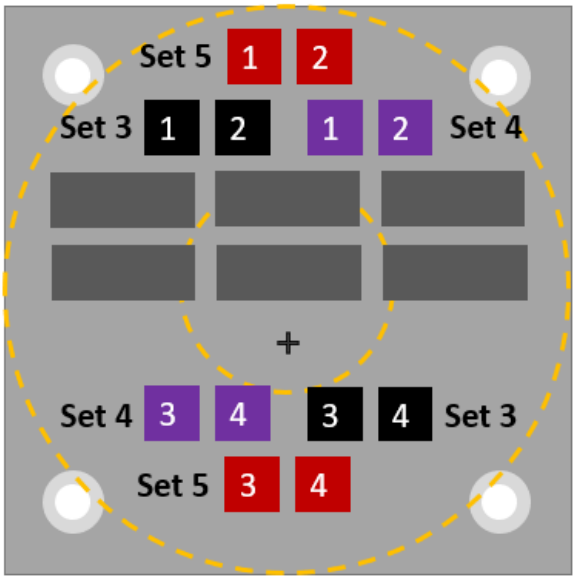

FIGURE 92: Layout for Experiment 5, Sets 3-5, with pads numbered.

Because the laser was set to constant-speed mode, the galvo-mounted mirrors controlling the beam take time to accelerate and decelerate between scanning each of the 50 tracks in each pad, which means that the AE signals for each individual track can be easily identified and separated. The RMS values of the AE signals recorded for each track and are shown in FIGURE 93. The AE signals for Set 3, Pad 2 were mistakenly not recorded.

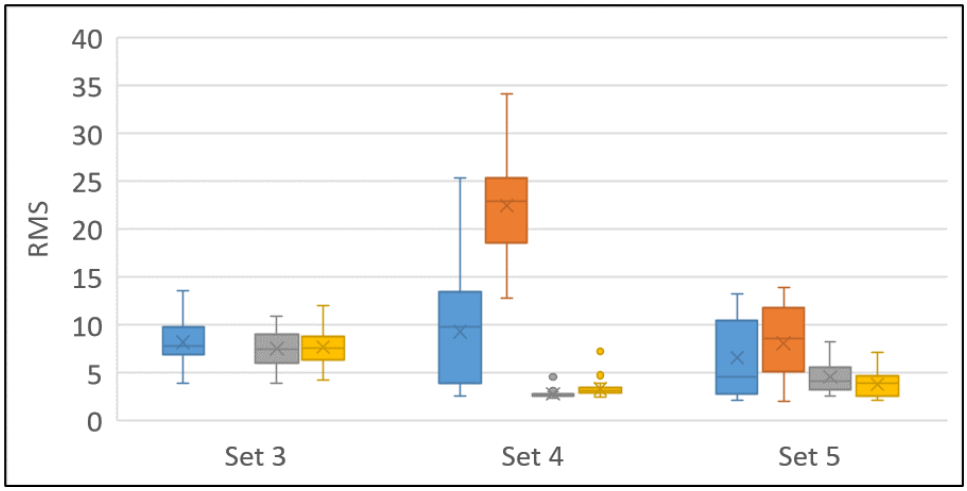

FIGURE 93: RMS values for all tracks in Sets 3-5.

The spread of RMS values is similar across all pads of Set 3. RMS values for Pad 1 of Set 4 are lower than Pad 2 due to the AE signal dropping significantly after the 26th track. Surface images of Pads 1 and 2, seen in FIGURE 94 offer no apparent explanation of the decrease in AE signal after the 26th track, denoted by a dotted line.

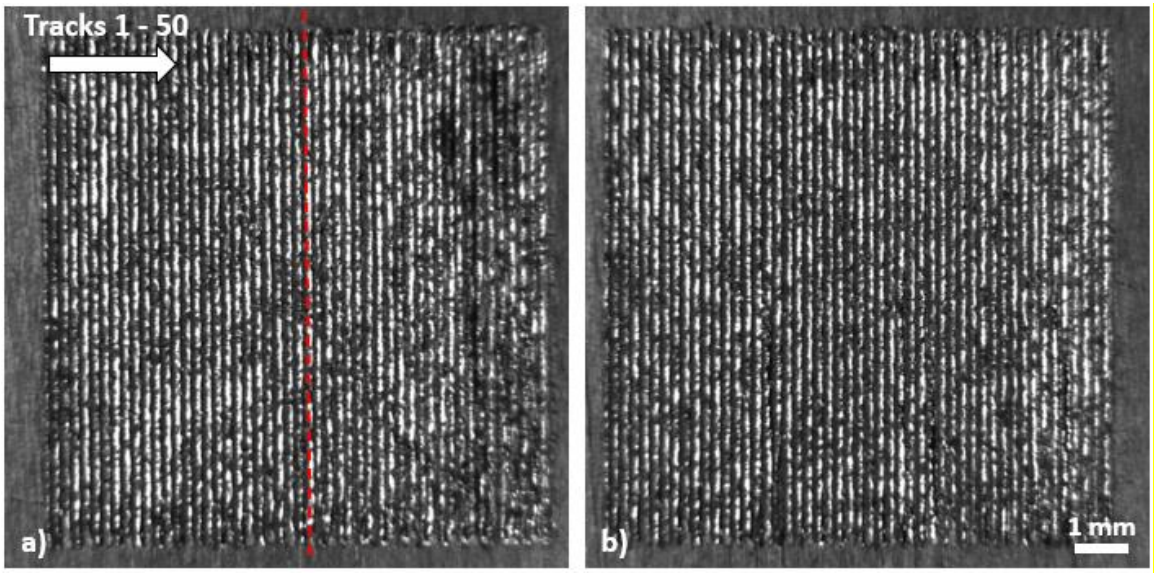

FIGURE 94: Surface image comparison of Set4, a) Pad 1 and b) Pad 2.

RMS values for Set 5 were expected to be higher than the other sets because of the higher laser power used to create these tracks. Due to the location of Pads 1 and 2 however, the laser beam was partially blocked by the enclosure shown in FIGURE 59a. This resulted in partial tracks, seen at the top of FIGURE 95, which decreased the calculated RMS value for each track.

FIGURE 95: Substrate with single layer of Ti64 after scanning Sets 1, 3, 4 & 5.

Pads 3 and 4 for Sets 4 and 5 have RMS values at or close to the noise floor of the AE measurement system. There are no indications in the surface images shown in FIGURE 96 to explain this lack of consistency in the AE signals.

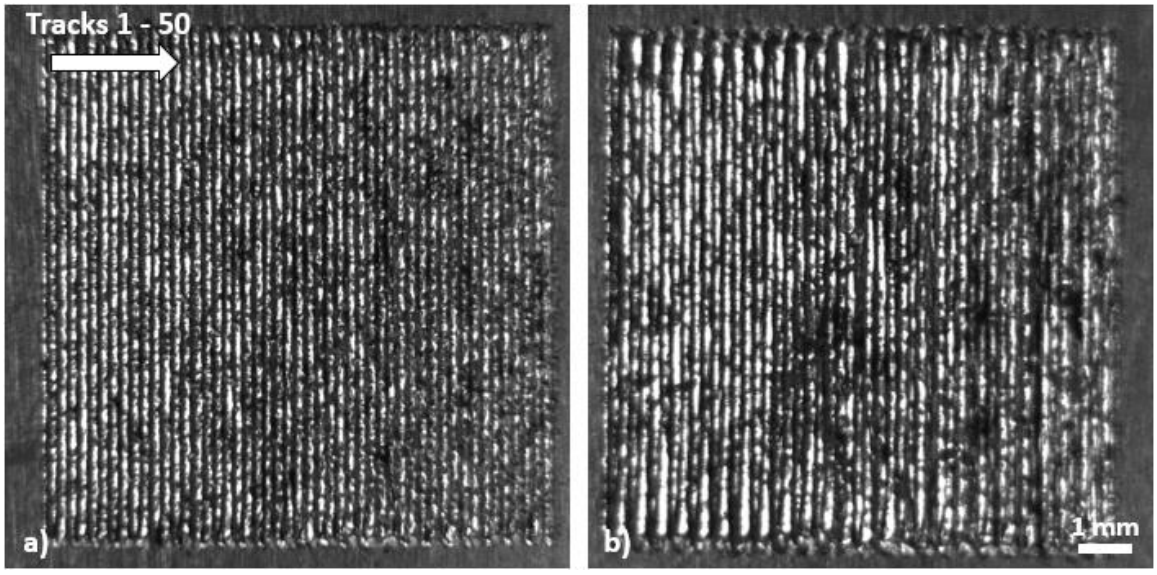

FIGURE 96: Surface images of a) Set 4, Pad 3 and b) Set 5, Pad 3.

CHAPTER 6: CONCLUSIONS & FUTURE RECOMMENDATIONS

6.1 Conclusions

This work documents the design, fabrication and successful integration into the AMMT of a stainless-steel instrumented build plate, which includes swappable substrates consisting of multiple common AM metals. A LabVIEW-based data acquisition system was assembled and synchronized with the AMMT's controller to record acoustic emissions in-situ. Initial experiments discussed in Chapter 3 demonstrated sensitivity of the measurement system to cracking during the LPBF process.

The second iteration of the instrumentation rig adds a PID-controlled resistance heater which allows preheating of the substrates or build plate up to 160 °C to prevent excessive cracking. Additionally, the existing build plate leveling mechanism was replaced with a more robust design. A new data acquisition and heater control program was developed to accommodate the new features and provide multi-sample-rate recording of the various sensor responses.

Follow-on experiments failed to repeat the cracking that generated the significant AE events seen initially. This is attributed to differences in powder composition between Experiment A and Experiments 1-5. The Ti64 powder used in Experiment A was a small, donated batch that was not well-documented and was only available for the first experiment. Experiments 1-5 were carried out using Spherical APA Ti-6Al-4V Grade 23 powder from Advanced Powders & Coatings, with a 15-63 μm particle size range (Advanced Powders & Coatings 2016).

TABLE 10 summarizes blower and imaging configurations for the experiments discussed in Chapter 5. The argon blower nozzle was removed after Experiment 2 over

concerns that it introduces too much variability. The characteristics of the gas flow from the nozzle are unknown and nozzle positioning is not well-controlled. However, it seems that significant differences in RMS values between bare and powder tracks occur only when using the blower nozzle.

TABLE 10: Chapter 5 experiment configurations.

	Blower nozzle	Meltpool camera	Denudation camera	Notes
Prelim experiment	N	N	N	
Experiment 1	Y	Y	N	
Experiment 2	Y	Y	Y	Denudation overlap
Experiment 3	N	Y	Y	Wrong spot size
Experiment 4	N	N	Y	Camera malfunction
Experiment 5	N	Y	Y	

Results from the NIR melt pool camera integrated into the AMMT are discussed in Chapter 6.3. Attempts to measure powder denudation started with Experiment 2, after results from the previous two experiments demonstrated significant differences in RMS values between bare and powder tracks but failed to reveal significant AE events to analyze. Even after improving the imaging setup between experiments, the amount of powder denudation around individual tracks was not significant enough to be clearly measured. Inconsistent RMS values from pads in Experiment 5 indicate that the measurement setup is not robust and/or that there are other variables affecting the process that have not been identified and controlled.

The following chapters present some preliminary analysis and recommendations for future work based on the lessons learned in the course of this project.

6.2 Future work: Frequency analysis

While RMS values of the raw AE signal are calculated in the time domain, the frequency domain also has characteristics that can be evaluated. Conversion to the

frequency domain is accomplished by performing a Fast Fourier Transform (FFT) on the AE signal of each track. FFTs were performed by applying the MATLAB 'fft' function using 2^{14} points, converting to a one-sided spectrum, and scaling the x-axis values according to the number of points and the original sampling frequency of 10 MHz.

Further investigation was begun on the trend observed in Experiment 1 where tracks created on a bare substrate resulted in a lower AE signal RMS than tracks created on a single layer of powder. The amplitude of the frequency spectrum for each track was first converted to power by multiplying by its conjugate, then normalized by the number of FFT points and length of the original AE signal. The average power values of the bare and single-layer frequency spectrums differ by several orders of magnitude, as shown in the power spectral density (PSD) plots in FIGURE 97.

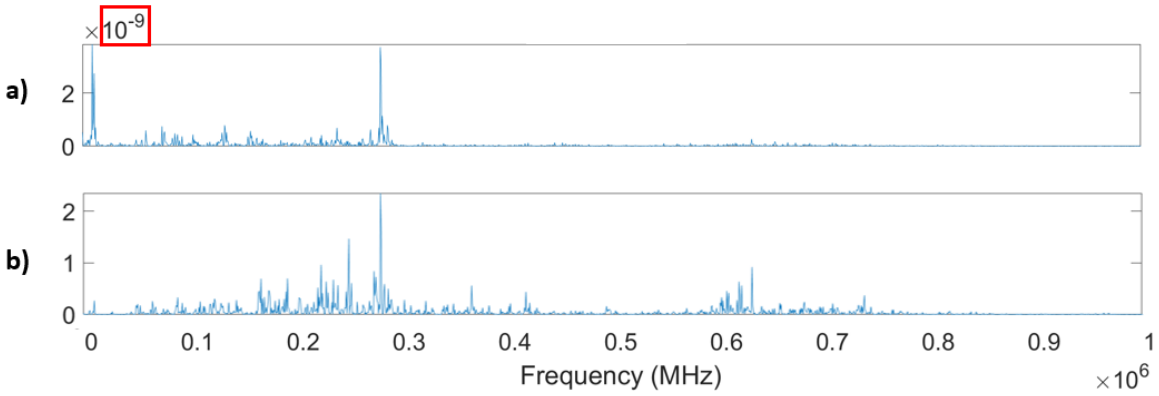

FIGURE 97: PSD plots for a) bare and b) single-layer track name g3t1 in Experiment 1, Sets 5b and 6b, Pad 1.

Besides the expected difference in average power, the single-layer tracks from this experiment have higher power content at higher frequencies than bare tracks. PSDs are especially good for comparing data sets of different durations because artificial amplitude changes are prevented by normalizing to the frequency bin width (Hanly 2016).

If the amplitude of the raw FFT can be normalized in another way however, it is easier to compare other characteristics like peaks across multiple data sets, described in the following paragraphs for tracks in Experiment 5. To count the top three frequencies for each track listed in TABLE 6, the frequency spectrum amplitudes were first normalized to the highest amplitude in each track's FFT plot. The MATLAB 'envelope' function was applied, and a threshold was chosen to ensure at least three peaks in each FFT plot. The three highest peaks of the envelope above this threshold were then identified. As demonstrated by the example in FIGURE 98, all FFT plots have a high amplitude peak around 10 kHz.

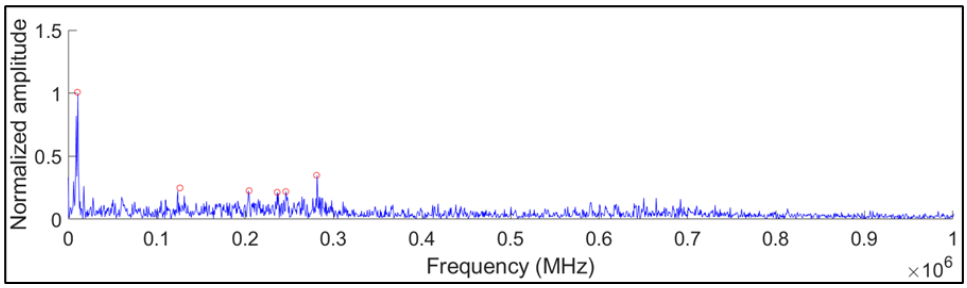

FIGURE 98: FFT peaks for Experiment 5, Set 5b, Pad 1, Track g4t1.

Since the AE sensor's bandwidth ranges from 100 kHz to 1 MHz however, the three highest peaks were recounted only between these frequencies. The result of this method is demonstrated below for selected tracks from Experiment 1, Set 5b, Pad 2. FIGURE 99 shows the a) envelope with threshold and b) counted peaks for track g1t1 (P100, V550), and the c) envelope with threshold and b) counted peaks for track g4t1 (P390, V800).

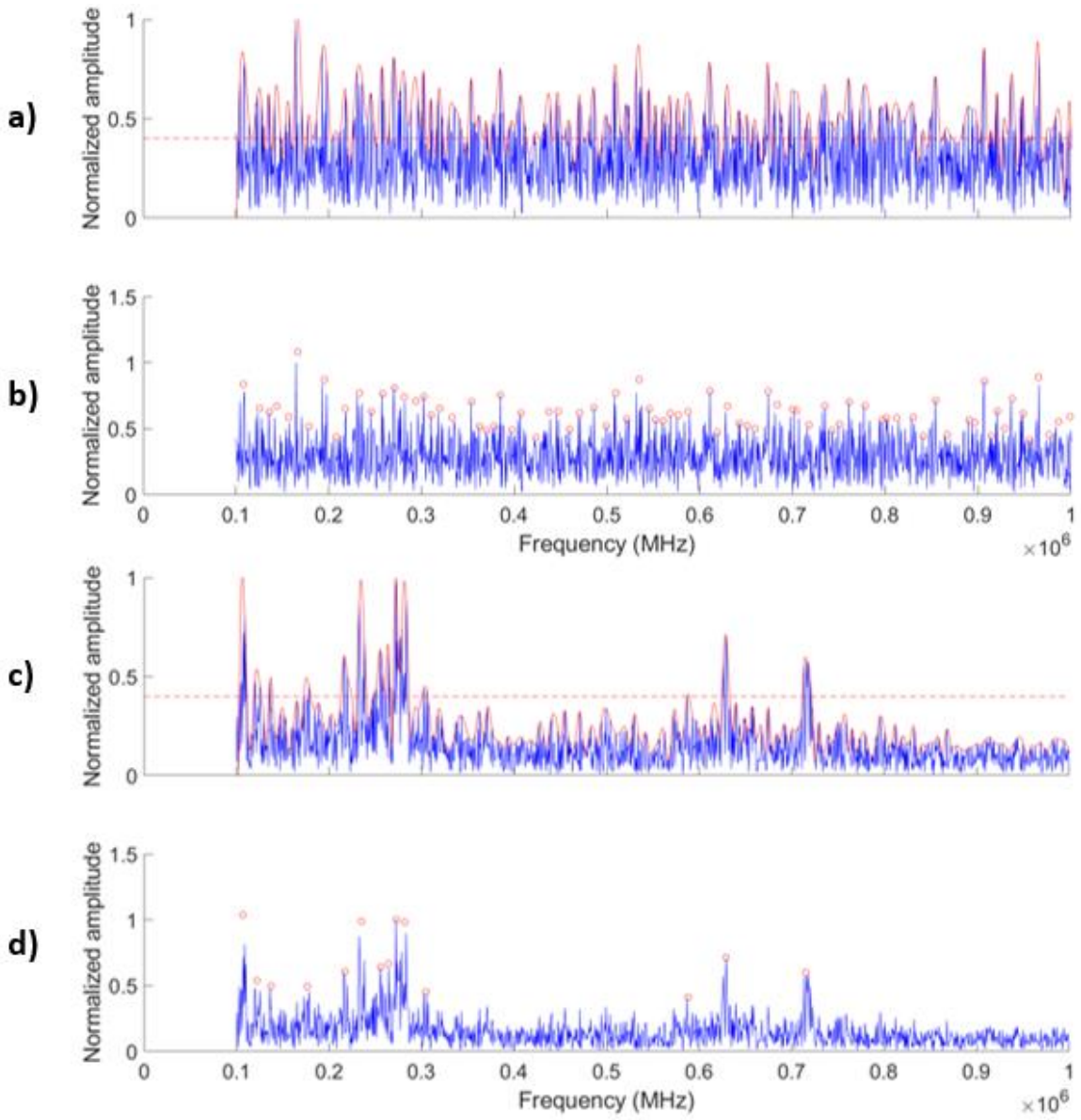

FIGURE 99: Peak counting on amplitude-normalized FFT plots.

The maximum real amplitude of track g1t1 is much lower than that of track g4t1, but the amplitudes of each track were normalized so a common threshold could be consistently applied. The frequencies of the three largest frequency spectrum amplitudes for each track in Set 5b are shown in FIGURE 100.

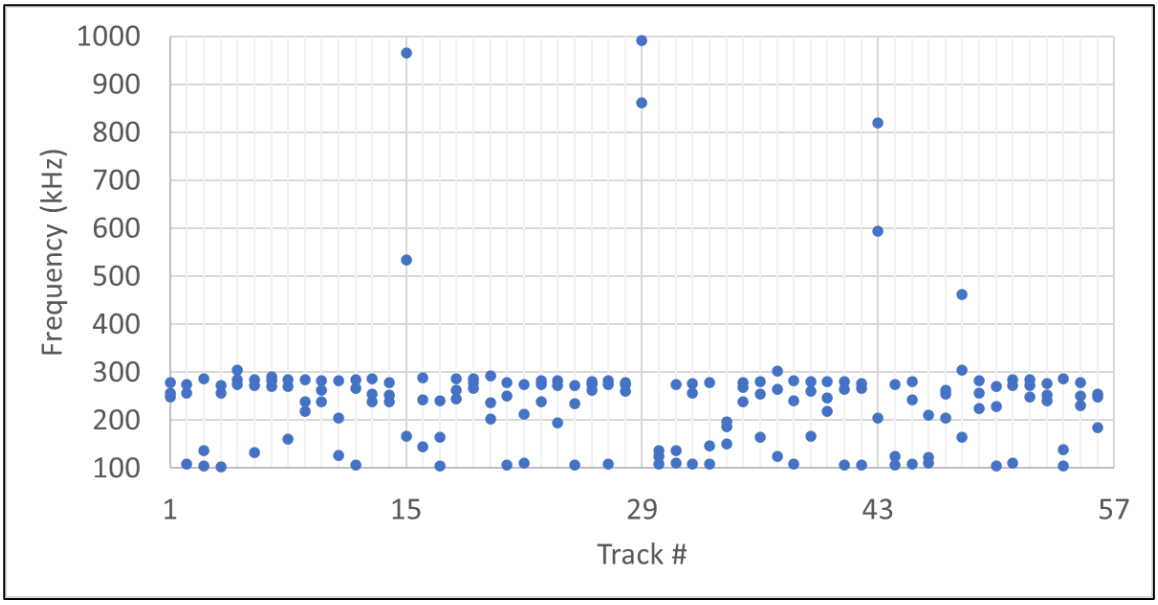

FIGURE 100: Top 3 FFT plot peaks (100-1000 kHz) in Experiment 1, Set 5b.

Most of the frequency content of all tracks seems to be located between 100 and 300 kHz. No energy-density-dependent patterns are apparent in this data, except that the first tracks in Pads 2-4 have large amplitude peaks in the higher frequencies. However, this is probably a result of the relatively consistent amplitudes across the entire frequency spectrum, as seen in FIGURE 98 a) and b). A possible continuation of this analysis is to apply frequency-domain filtering based on the largest amplitudes of the frequency spectrum and the AE sensor's bandwidth. Reverse Fourier transforms could then be performed and the reconstructed signals analyzed further in the time domain.

Another analysis technique for comparing different signals is cross-correlation. The strength of the correlation can be given by a value known as the correlation coefficient. All tracks in Experiment 1, Set 5b were compared against each other and the correlation coefficients plotted in color maps. FIGURE 101 shows the results of cross-correlating the raw AE signals, which were all truncated to match the shortest signal.

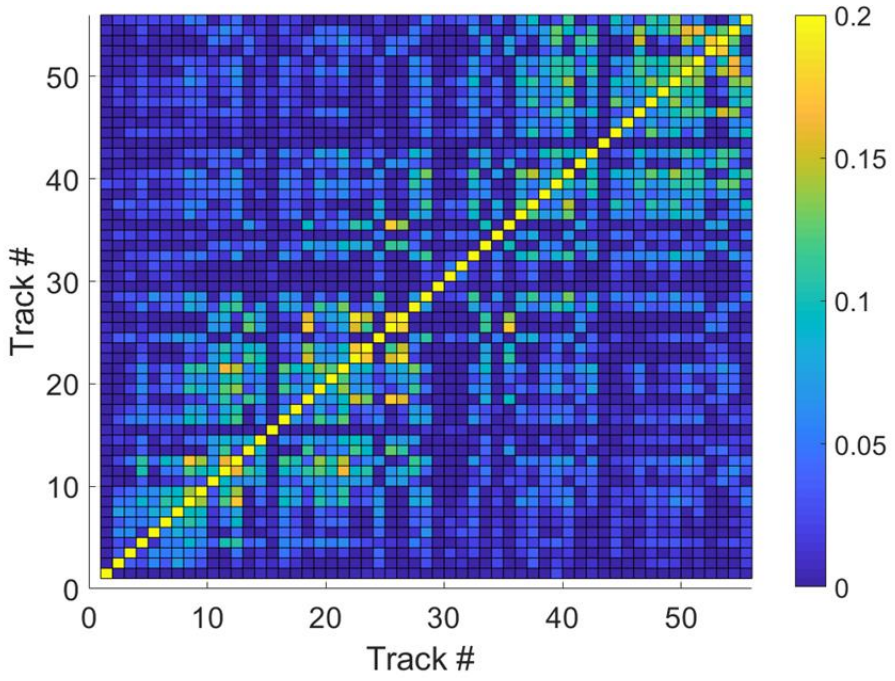

FIGURE 101: Cross-correlation coefficients for Exp1, Set 5b raw AE signals.

FIGURE 102 shows the results of cross-correlating the frequency spectra of the same set of AE signals.

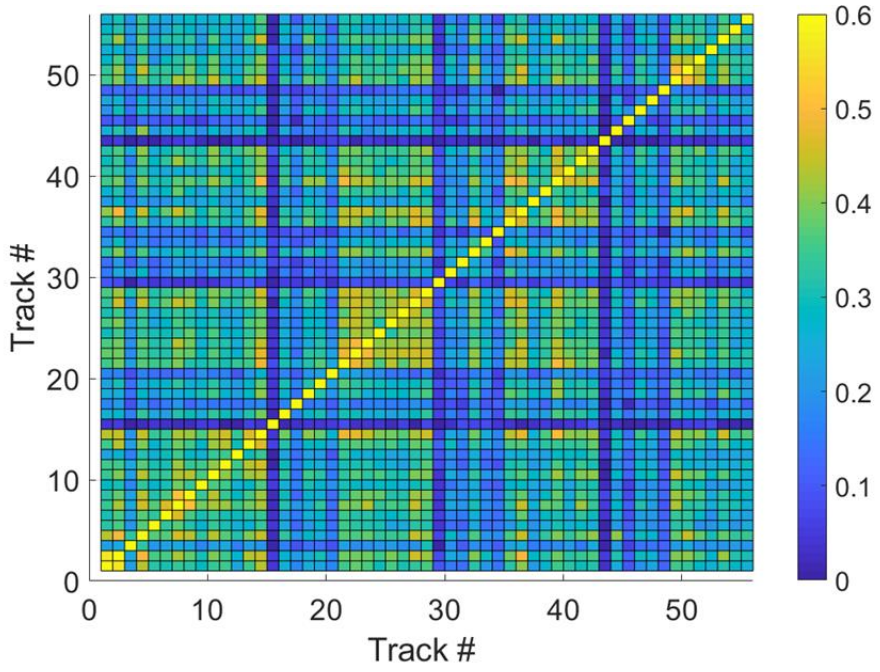

FIGURE 102: Cross-correlation coefficients for Exp1, Set5b frequency spectra.

As expected, all cross-correlation coefficients are saturated (have a value of 1) on the diagonal line because they are compared with themselves, while the other coefficients from comparing different signals are mirrored across the line. This preliminary work is meant to demonstrate another possible analysis method.

Other frequency analysis tools include the continuous wavelet transform and short-term Fourier transform. Both techniques analyze the frequency content of a signal along the time axis. An example of the latter is shown in FIGURE 103, comparing the first three tracks of Experiment 1, Set 5b, Pad 1. Longer AE signals were truncated to match the shortest one.

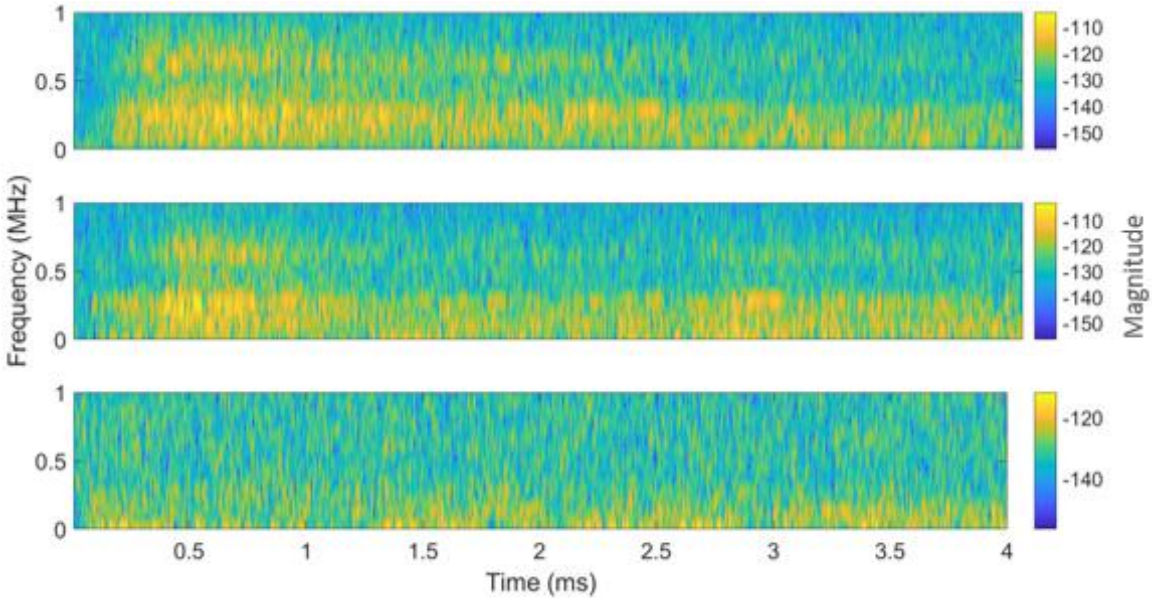

FIGURE 103: Short-term Fourier transforms of selected AE signals.

This technique shows some promise in that there are differences not only between different AE signals, but also along the time axis of each signal, where correlations to spatially varying surface topography or defects could be investigated.

6.3 Future work: Melt pool monitoring

The AMMT's near infrared camera is configured coaxially with the laser beam to image the melt pool at 10 kHz, with a pixel size of approximately 8 μm square (Brandon Lane and Levine 2019). Melt pool dimensions that vary with process parameters like laser power and scanning speed can be identified with this type of measurement, as demonstrated by the selection of tracks with different linear energy densities shown in FIGURE 104.

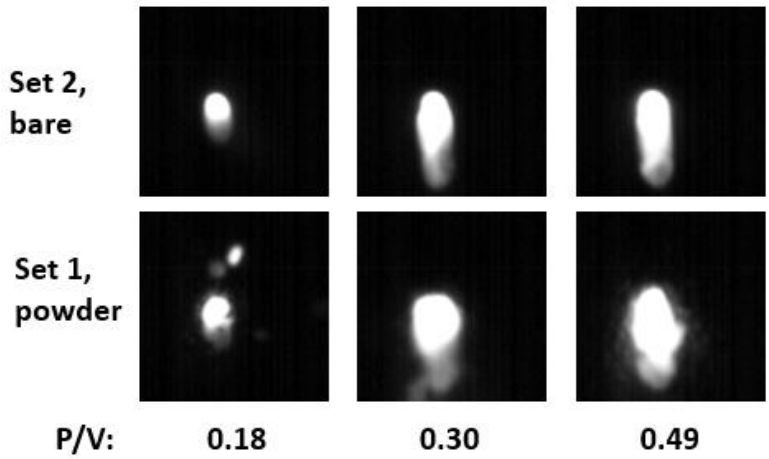

FIGURE 104: NIR images of 10th frame of selected tracks from Experiment 5.

Unexpected variations in the length, width and shape of the melt pool could be compared to AE signal characteristics at that moment in time. Another feature of interest in these images is the melted powder particles that can be ejected from the melt pool. A hypothesis was formed that an ejected particle, or liquid metal collapsing on a cavity left by an ejected particle, generates acoustic emissions. The size, velocity and number of ejected particles, like the one indicated with an arrow in FIGURE 105, could possibly be quantified and compared to AE signal characteristics.

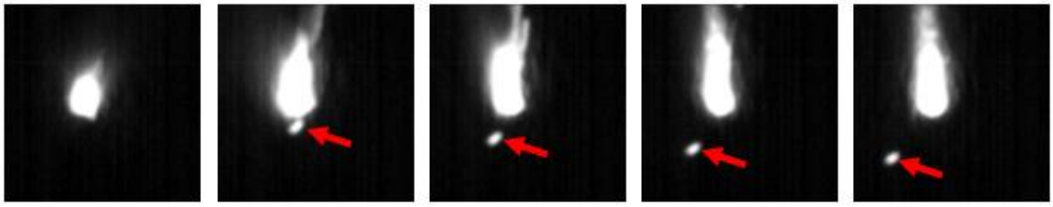

FIGURE 105: NIR images of first 5 frames of Experiment 5, Set 3, Pad 1.

The path of ejected particles can also be visualized by combining melt pool images for entire tracks, as shown in FIGURE 106. Further experiments are recommended to determine if particle ejections are contributing to the AE signal in order to filter them out when evaluating other possible sources of AE.

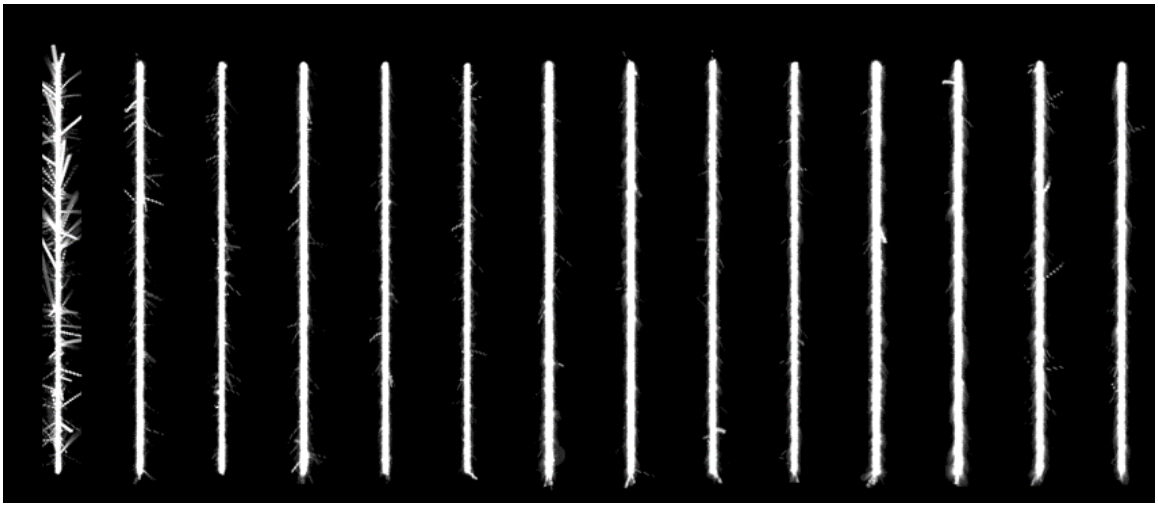

FIGURE 106: Combined melt pool images for all tracks in Experiment 5, Set 1, Pad 1 (image compilation by Nikola Bura).

6.4 Future work: Repeatability testing

Due to the inconsistency of the RMS values from Sets 3-5 in Experiment 5, the repeatability of the AE sensor setup was tested. The bottom plates of the instrumentation rig were left in the AMMT as part of the new leveling mechanism, so the rig was placed on a thick piece of dense foam as shown in FIGURE 107. The AE sensor was installed as usual, directly under a Ti64 substrate with Magnaflux Sono 600 couplant.

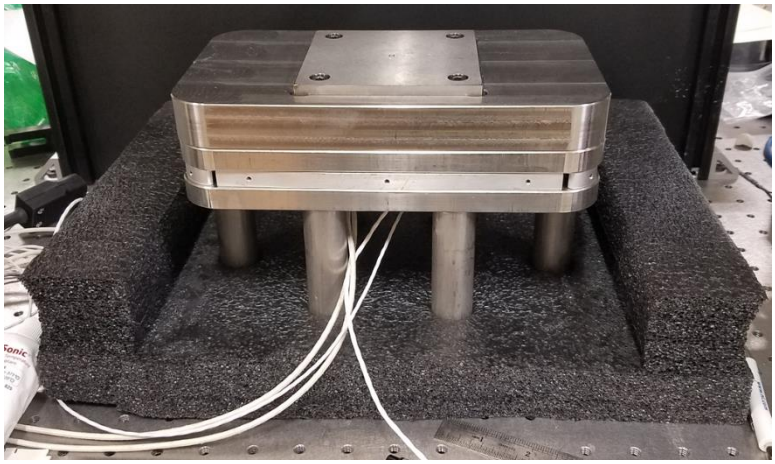

FIGURE 107: Top part of instrumentation rig on vibration-damping foam.

Hsu-Nielsen pencil-lead break (PLB) tests, described in Chapter 2.2, were carried out on a 2 mm x 2 mm area on the top surface of the substrate, directly above the AE sensor. Seven sets of 10 PLBs each were recorded, with the same substrate being removed and reinstalled between each set. The couplant was cleaned off and reapplied with every reinstall, and the RMS values of all the PLBs are shown in FIGURE 108.

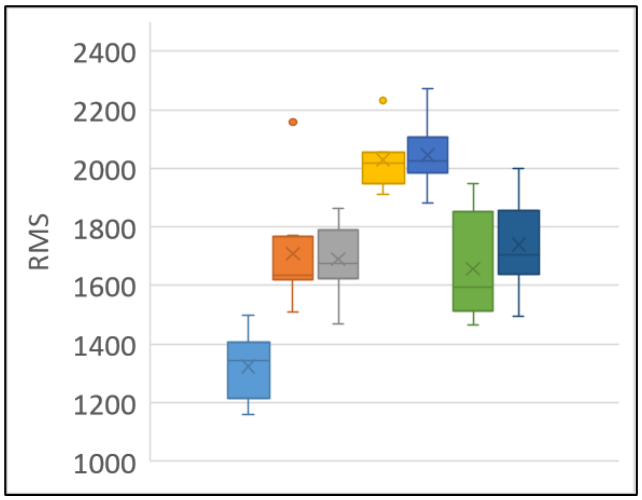

FIGURE 108: RMS values for PLBs in center of substrate.

The average RMS value of these PLBs is much higher than any RMS values for AE signals recorded during the single-layer experiments (1700 vs max 50 RMS units). This comparison gives an idea of how weak the AE signals are during the LPBF process.

The average RMS value of PLBs on the 3/8” thick substrate is also higher than those recorded for PLBs on a 1” thick build plate (1700 vs 350 RMS units) described in Chapter 2.2. This could be due to attenuation through the bulk of a thicker build plate or because Permatex Blue couplant was used for the 1” plate PLBs.

With the exception of one high value in the second set, RMS values for all PLBs within a set do not deviate more than 17% of the average RMS value of that set. Further testing is recommended to quantify the repeatability of the measurement system and investigate the influence of couplant application, AE sensor contact pressure and attenuation of the AE signal both laterally and vertically through the build plate. Based on testing results, the AE sensor setup could also be redesigned for better vibration isolation to improve signal to noise ratio.

6.5 Future work: Acoustic performance

Complementary to achieving better repeatability, there are several ways that the acoustic sensor configuration could be improved to increase SNR and reduce reverberations. Many of these possible modifications stem from discussions with Steve Fick at NIST.

Joint slip due to different materials expanding or contracting can result in acoustic emissions. Further simulations are recommended to explore the level of thermal stress in a constrained build plate heated to 160 °C. If high thermal stress is present, it can be designed out mechanically by mounting the build plate kinematically to allow movement in the appropriate degrees of freedom, and by using Teflon sheets between plates and as bushings around bolts.

Reverberation of elastic waves within the structure supporting the build plate make interpretation of the AE sensor response more difficult. One approach to reduce reverberations is to design a substrate with a certain geometry that can only support certain resonant modes, such as the Beattie block shown in FIGURE 109.

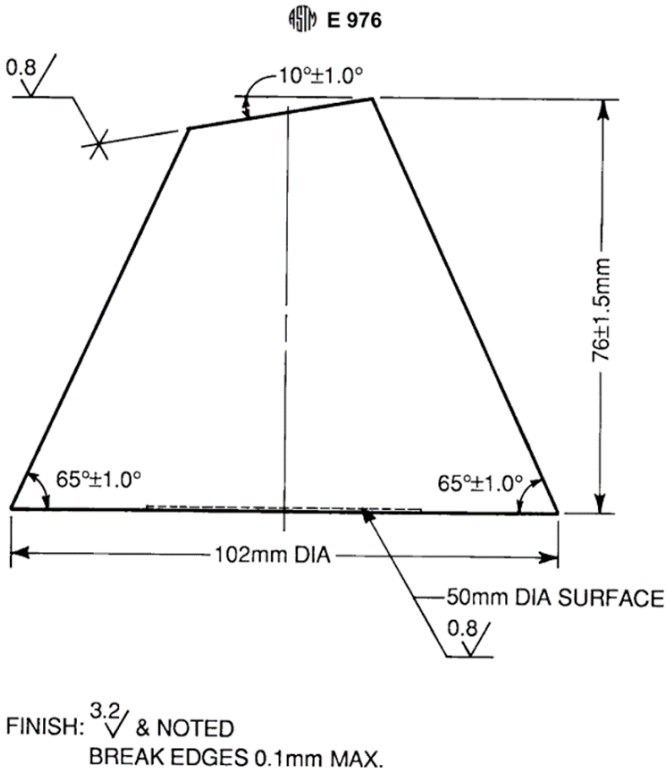

FIGURE 109: "Nonresonant" conical block for AE testing (ASTM 1999).

The lack of parallel surfaces greatly reduces the number of mechanical resonances when the AE sensor is mounted to the shorter surface that is offset by 10 degrees. On a more traditional plate of well-known geometry, a pair of AE sensors in pulse-echo mode could be used to measure the signature of the impulse and the ring-down time. A filter could then be designed to remove some of the reverberations from the signal.

Bolts securing a build plate also act as wave guides, and complex geometries behave as higher order resonators. Damping could be applied at interfaces to attenuate reverberations. Ideally, the build plate should be isolated from the rest of the structure as

a “floating” plate. The frequency content of the AE signal should be further evaluated to find an interface material that provides the best damping at the major frequencies.

Contact between the heater and the build plate changes the geometry and affects the reverberations. A possible contact-less solution is to use inductive heating, which greatly increases the complexity of the design however (Caprio et al. 2018). Additionally, a buffer rod made from quartz may be necessary to provide separation between the AE sensor and the magnetic field heating the build plate.

Since AE transducer noise is dominated by electronics, one way to increase the SNR is to ensure proper coupling. In addition to couplant re-application experiments from Chapter 6.4, further experiments are recommended to investigate the effect of different coupling compounds on the recorded energy of well-controlled pencil lead breaks. Other mounting methods should also be explored, including the use of a low viscosity, low shear strength adhesive couplant made from 2-part anaerobic silicone rubber. It is recommended to mix this type of couplant in a soft vacuum to avoid entrapping air which would change the acoustic impedance across the sensor head.

The physical design of the current instrumented build plate is not compatible with many of these modifications, so a new build plate may need to be fabricated to acquire the AE sensor response separately from the stress measurements in future experiments to achieve the best results.

6.6 Future work: Other

Experiment 1 had the potential to be a two-level full factorial screening design with three factors according to the Design of Experiments method, which is a systematic method to determine the relationship between factors affecting a process and the output

of that process (NIST/SEMATECH 2013). Future experiments should apply this method to properly explore the relationship between the many process parameters and variables, listed in TABLE 11, that were identified in this work as having an effect on the LPBF process and potentially on the recorded AE signal.

TABLE 11: Measured or estimated parameters affecting the LPBF process.

Parameter/variable
Laser power
Laser speed
Laser spot size
Substrate material
Substrate flatness
Substrate temperature
Powder material
Powder layer thickness
Oxygen content
Blower nozzle flow rate
Blower nozzle proximity

In addition to the listed laser parameters, the laser beam intensity profile should also be recorded for each future experiment. As indicated by the lack of cracking after switching powder batches between Experiment A and Experiment 1, the chemical composition, particle size distribution, morphology, thermal properties and flow characteristics all affect the LPBF process (Field et al. 2020). A powder with higher cracking susceptibility could be chosen to further evaluate hit-based AE analysis.

A thorough investigation into the effects of the argon blower nozzle is recommended. The blower nozzle can redirect the plume of vaporized metal above the melt pool, which changes the energy density at the powder layer. It is hypothesized that using the blower nozzle leads to significant differences in the RMS of the AE signal between tracks created on a bare substrate vs on a single layer of powder. However, the

flow field across the active build area should be characterized for each blower nozzle position to make robust conclusions.

REFERENCES

Advanced Powders & Coatings. 2016. “SAFETY DATA SHEET - Product: Spherical Ti-6Al-4V Powder (Coarse).” *SDS Document Number TI64-B-06-E*. http://advancedpowders.ca/wp-content/uploads/SDS-Ti-6Al-4V-Coarse-English-16-04-15.pdf.

Ali, Haider, Le Ma, Hassan Ghadbeigi, and Kamran Mumtaz. 2017. “In-Situ Residual Stress Reduction, Martensitic Decomposition and Mechanical Properties Enhancement through High Temperature Powder Bed Pre-Heating of Selective Laser Melted Ti6Al4V.” *Materials Science and Engineering: A* 695 (April): 211–20. https://doi.org/10.1016/j.msea.2017.04.033.

Apogee Instruments Inc. 2019. “Differential vs. Single-Ended Measurements.” 2019. https://www.apogeeinstruments.com/differential-vs-single-ended-measurements.

ASTM. 1999. “Standard Guide for Determining the Reproducibility of Acoustic Emission.” *Annual Book of ASTM Standards*, no. C: 1–7. https://doi.org/10.1520/E0976-10.2.

Caprio, L, G Chiari, A G Demir, and B Previtali. 2018. “Development of Novel High Temperature Laser Powder Bed Fusion System for the Processing of Crack-Susceptible Alloys,” 2275–85.

Carter, Luke N., Christopher Martin, Philip J. Withers, and Moataz M. Attallah. 2014. “The Influence of the Laser Scan Strategy on Grain Structure and Cracking Behaviour in SLM Powder-Bed Fabricated Nickel Superalloy.” *Journal of Alloys and Compounds* 615: 338–47. https://doi.org/10.1016/j.jallcom.2014.06.172.

Cleveland Electric Laboratories. n.d. “Datasheet: LCM-200 Series Brainy Bolts.”

http://www.clevelandelectriclabs.com/wp-content/uploads/2016/02/Brainy-Bolt2015.pdf.

Cunningham, Ross, Sneha P. Narra, Colt Montgomery, Jack Beuth, and A. D. Rollett. 2017. "Synchrotron-Based X-Ray Microtomography Characterization of the Effect of Processing Variables on Porosity Formation in Laser Power-Bed Additive Manufacturing of Ti-6Al-4V." *Jom* 69 (3): 479–84. https://doi.org/10.1007/s11837-016-2234-1.

Dunbar, A. J., E. R. Denlinger, J. Heigel, P. Michaleris, P. Guerrier, R. Martukanitz, and T. W. Simpson. 2016. "Development of Experimental Method for in Situ Distortion and Temperature Measurements during the Laser Powder Bed Fusion Additive Manufacturing Process." *Additive Manufacturing* 12: 25–30. https://doi.org/10.1016/j.addma.2016.04.007.

Eschner, N, L Weiser, B Häfner, and G Lanza. 2018. "Development of an Acoustic Process Monitoring System for Selective Laser Melting (SLM)." *Solid Freeform Fabrication Symposium*, no. Reschetnik 2017: 2097–2117.

Field, A. C., L. N. Carter, N. J.E. Adkins, M. M. Attallah, M. J. Gorley, and M. Strangwood. 2020. "The Effect of Powder Characteristics on Build Quality of High-Purity Tungsten Produced via Laser Powder Bed Fusion (LPBF)." *Metallurgical and Materials Transactions A: Physical Metallurgy and Materials Science* 51 (3): 1367–78. https://doi.org/10.1007/s11661-019-05601-6.

Gan, Zhengtao, Yanping Lian, Stephen E. Lin, Kevontrez K. Jones, Wing Kam Liu, and Gregory J. Wagner. 2019. "Benchmark Study of Thermal Behavior, Surface Topography, and Dendritic Microstructure in Selective Laser Melting of Inconel

625." *Integrating Materials and Manufacturing Innovation* 8 (2): 178–93. https://doi.org/10.1007/s40192-019-00130-x.

Gold, Scott Alan, and Thomas Graham Spears. 2017. Acoustic monitoring method for additive manufacturing process. US 2017/0146488 A1, issued 2017.

Gong, Haijun, Khalid Rafi, Hengfeng Gu, Thomas Starr, and Brent Stucker. 2014. "Analysis of Defect Generation in Ti-6Al-4V Parts Made Using Powder Bed Fusion Additive Manufacturing Processes." *Additive Manufacturing* 1: 87–98. https://doi.org/10.1016/j.addma.2014.08.002.

Grasso, Marco, and Bianca Maria Colosimo. 2017. "Process Defects and in Situ Monitoring Methods in Metal Powder Bed Fusion: A Review." *Measurement Science and Technology* 28 (4): aa5c4f. https://doi.org/10.1088/1361-6501/aa5c4f.

Hanly, Steve. 2016. "Why the Power Spectral Density (PSD) Is the Gold Standard of Vibration Analysis." Endaq Blog. 2016. https://blog.endaq.com/why-the-power-spectral-density-psd-is-the-gold-standard-of-vibration-analysis.

Harrison, Neil J., Iain Todd, and Kamran Mumtaz. 2015. "Reduction of Micro-Cracking in Nickel Superalloys Processed by Selective Laser Melting: A Fundamental Alloy Design Approach." *Acta Materialia* 94: 59–68. https://doi.org/10.1016/j.actamat.2015.04.035.

He, Lugui, Haiyan Zhao, and Wenchong Niu. 2018. "Understanding the Effect of Oxygen on Weld Pool and Keyhole in Laser Beam Welding." *Journal of Laser Applications* 30 (1): 012003. https://doi.org/10.2351/1.5017703.

Heigel, J. C., and B. M. Lane. 2017. "The Effect of Powder on Cooling Rate and Melt Pool Length Measurements Using In Situ Thermographic Techniques." *Proceedings*

of the 2017 Annual International SFF Symposium. https://tsapps.nist.gov/publication/get_pdf.cfm?pub_id=923988.

Heigel, J. C., and B. M. Lane. 2018. "Measurement of the Melt Pool Length during Single Scan Tracks in a Commercial Laser Powder Bed Fusion Process." *Journal of Manufacturing Science and Engineering, Transactions of the ASME* 140 (5): 1–8. https://doi.org/10.1115/1.4037571.

Iowa State University. 2001. "AE Signal Features." NDT Education Resource Center. 2001. https://www.nde-ed.org/EducationResources/CommunityCollege/Other Methods/AE/AE_Signal Features.htm.

Khairallah, Saad A., Andrew T. Anderson, Alexander Rubenchik, and Wayne E. King. 2016. "Laser Powder-Bed Fusion Additive Manufacturing: Physics of Complex Melt Flow and Formation Mechanisms of Pores, Spatter, and Denudation Zones." *Acta Materialia* 108: 36–45. https://doi.org/10.1016/j.actamat.2016.02.014.

Kouprianoff, D, N Luwes, E Newby, I Yadroitsava, and I Yadroitsev. 2017. "On-Line Monitoring of Laser Powder Bed Fusion by Acoustic Emission Acoustic Emission for Inspection of Single Tracks under Different Powder Layer Thickness," 203–7.

LabVIEW Wiki. 2019. "Design Patterns Overview." 2019. https://labviewwiki.org/wiki/Design_Patterns_Overview.

Lane, B, S Mekhontsev, S Grantham, ML Vlasea, J Whiting, H Yeung, J Fox, et al. 2016. "Design, Developments, and Results from the NIST Additive Manufacturing Metrology Testbed (AMMT)." *Solid Freeform Fabrication Symposium*, 1145–60. https://ws680.nist.gov/publication/get_pdf.cfm?pub_id=921551%0Ahttp://ws680.nist.gov/publication/get_pdf.cfm?pub_id=921551%0Ahttp://ws680.nist.gov/publicatio

n/get_pdf.cfm?pub_id=921551%0Ahttps://sffsymposium.engr.utexas.edu/sites/default/files/2016/093-La.

Lane, Brandon, and Lyle Levine. 2019. “2018 AM-Bench Test Descriptions for AMB2018-02.” 2019. https://www.nist.gov/ambench/amb2018-02-description.

Magnaflux. 2018. “Product Data Sheet: Magnaflux Sono 600.” https://www.mxindustrial.com/wp-content/uploads/2015/12/Sonotech-Sono-600-PDS.pdf.

Makoana, Nkutwane Washington, Ina Yadroitsava, Heinrich Möller, and Igor Yadroitsev. 2018. “Characterization of 17-4ph Single Tracks Produced at Different Parametric Conditions towards Increased Productivity of Lpbf Systems—the Effect of Laser Power and Spot Size Upscaling.” *Metals* 8 (7). https://doi.org/10.3390/met8070475.

Matthews, Manyalibo J, Gabe Guss, Saad A Khairallah, Alexander M Rubenchik, Philip J Depond, and Wayne E King. 2016. “Denudation of Metal Powder Layers in Laser Powder Bed Fusion Processes.” *Acta Materialia* 114: 33–42. https://doi.org/10.1016/j.actamat.2016.05.017.

Maxim Integrated. 2015. “MAX31865 Datasheet.” https://datasheets.maximintegrated.com/en/ds/MAX31865.pdf.

Mercelis, Peter, and Jean Pierre Kruth. 2006. “Residual Stresses in Selective Laser Sintering and Selective Laser Melting.” *Rapid Prototyping Journal* 12 (5): 254–65. https://doi.org/10.1108/13552540610707013.

MISTRAS Group. n.d. “Acoustic Emission - AE Systems.” Accessed April 12, 2019. https://mistrasgroup.co.uk/products-and-systems/ae-systems.

NIST/SEMATECH. 2013. “Two-Level Full Factorial Designs.” Engineering Statistics

Handbook. 2013. https://www.itl.nist.gov/div898/handbook/pri/section3/pri3331.htm.

Of, Effects, Shield Gas, Flow On, Meltpool Variability, Signature In, and Scanned Laser Melting. 2020. “Msec2020-8410 Effects of Shield Gas Flow on Meltpool Variability and Signature In,” 1–12.

Permatex. 2018. “Technical Data Sheet: Permatex Ultra Blue RTV Silicone Gasket Maker.” https://www.permatex.com/wp-content/uploads/tech_docs/tds/81725.pdf.

Shuai, Li, Qingsong Wei, Yusheng Shi, Jie Zhang, and Li Wei. 2016. “Micro-Crack Formation and Controlling of Inconel625 Parts Fabricated by Selective Laser Melting.” *Solid Freeform Fabrication Symposium – An Additive Manufacturing Conference*, 520–29. https://sffsymposium.engr.utexas.edu/sites/default/files/2016/038-Shuai.pdf.

Smith, Richard J., Matthias Hirsch, Rikesh Patel, Wenqi Li, Adam T. Clare, and Steve D. Sharples. 2016. “Spatially Resolved Acoustic Spectroscopy for Selective Laser Melting.” *Journal of Materials Processing Technology* 236: 93–102. https://doi.org/10.1016/j.jmatprotec.2016.05.005.

Strainsert. n.d. “Standard Internally Gaged 12-Point Cap Screws, SDH Series.” http://www.process-controls.com/intertechnology/Strainsert/pdfs/Stnd_Inter_Gauged_12_Point_Cap_Screws.pdf.

Thériault, Gabrielle. 2018. “The Beginner’s Guide on Spot Size of Laser Beam.” Gentec-EO. 2018. https://www.gentec-eo.com/blog/spot-size-of-laser-beam.

Thorlabs Inc. 1999. “PID Tutorial.” 1999.

https://www.thorlabs.com/tutorials.cfm?tabID=5DFCA308-D07E-46C9-BAA0-4DEFC5C40C3E.

Vallen, Hartmut. 2006. “AE Testing: Fundamentals, Equipment, Applications.” Vallen-Systeme GmbH. http://www.vallen.de/zdownload/pdf/sea204E.pdf.

Wang, Di, Wenhao Dou, and Yongqiang Yang. 2018. “Research on Selective Laser Melting of Ti6Al4V: Surface Morphologies, Optimized Processing Zone, and Ductility Improvement Mechanism.” *Metals* 8 (7). https://doi.org/10.3390/met8070471.

Wasmer, K., T. Le-Quang, B. Meylan, F. Vakili-Farahani, M. P. Olbinado, A. Rack, and S. A. Shevchik. 2018. “Laser Processing Quality Monitoring by Combining Acoustic Emission and Machine Learning: A High-Speed X-Ray Imaging Approach.” *Procedia CIRP* 74: 654–58. https://doi.org/10.1016/j.procir.2018.08.054.

Yadroitsev, I., A. Gusarov, I. Yadroitsava, and I. Smurov. 2010. “Single Track Formation in Selective Laser Melting of Metal Powders.” *Journal of Materials Processing Technology* 210 (12): 1624–31. https://doi.org/10.1016/j.jmatprotec.2010.05.010.

Yeung, H., B. M. Lane, M. A. Donmez, J. C. Fox, and J. Neira. 2018. “Implementation of Advanced Laser Control Strategies for Powder Bed Fusion Systems.” *Procedia Manufacturing* 26: 871–79. https://doi.org/10.1016/j.promfg.2018.07.112.

Yu, J., M. Rombouts, and G. Maes. 2013. “Cracking Behavior and Mechanical Properties of Austenitic Stainless Steel Parts Produced by Laser Metal Deposition.” *Materials and Design* 45: 228–35. https://doi.org/10.1016/j.matdes.2012.08.078.

APPENDIX: ARDUINO BANG-BANG CONTROL CODE

```
/***************************************************
  This is a library for the Adafruit PT100/P1000 RTD Sensor w/MAX31865
  Designed specifically to work with the Adafruit RTD Sensor
  ----> https://www.adafruit.com/products/3328
  This sensor uses SPI to communicate, 4 pins are required to
  interface
  Adafruit invests time and resources providing this open source code,
  please support Adafruit and open-source hardware by purchasing
  products from Adafruit!
  Written by Limor Fried/Ladyada for Adafruit Industries.
  BSD license, all text above must be included in any redistribution

  Modified by Sam Ludwig
 ****************************************************/

#include <Adafruit_MAX31865.h>
// use hardware SPI, just pass in the CS pin
        Adafruit_MAX31865 max1 = Adafruit_MAX31865(10); //define CS pins
Adafruit_MAX31865 max2 = Adafruit_MAX31865(6);
Adafruit_MAX31865 max3 = Adafruit_MAX31865(7);
Adafruit_MAX31865 max4 = Adafruit_MAX31865(8);
Adafruit_MAX31865 max5 = Adafruit_MAX31865(9);

// The value of the Rref resistor. Use 430.0 for PT100 and 4300.0 for PT1000
#define RREF      430.0
// The 'nominal' 0-degrees-C resistance of the sensor
// 100.0 for PT100, 1000.0 for PT1000
#define RNOMINAL  100.0

//initialize variables
unsigned long target = 100;           //target temperature in deg C
float upper = 0;                    //hysteresis
float lower = 1;
        unsigned long period = 1000;          //time we need to wait in milliseconds,
        sampling period
        unsigned long interval = period - 756;  //adjust interval to account for time it takes
        to run code
unsigned long previousMillis = 0;       //initialize previousMillis
unsigned long relaypin = 2;           //set relay pin number
unsigned long state = 0;              //initialize to temp <= lower limit
uint16_t rtd;
float ratio;
float fb_rtd;
```

```
void setup() {
          Serial.begin(115200);        //sets data rate in baud rate for serial data transfer
  pinMode(relaypin, OUTPUT);    // set the selected digital pin as output
  max1.begin(MAX31865_3WIRE);   // initialize sensors
  max2.begin(MAX31865_3WIRE);
  max3.begin(MAX31865_3WIRE);
  max4.begin(MAX31865_3WIRE);
  max5.begin(MAX31865_3WIRE);
}

void loop() {
          unsigned long currentMillis = millis(); //gets the current time (ms) since program
         started
   //Check if "interval" time has passed (i.e. 1000 ms), if c-pMillis < interval,
   // then code will skip the following if statement and will continue counting
   if((unsigned long)(currentMillis - previousMillis) >= interval)
  {
   rtd = max1.readRTD();   //read RTD
   ratio = rtd;
   ratio /= 32768;        //ratio = ratio/32768
   fb_rtd = max1.temperature(RNOMINAL, RREF);
            Serial.print("Time, "); Serial.println((currentMillis-interval)/1000); //show time
         in seconds
   Serial.print("FB Temp, "); Serial.println(fb_rtd);

   currentMillis = millis(); //gets the current time (ms) since program started
   rtd = max2.readRTD();     //read RTD
   ratio = rtd;
   ratio /= 32768;          //ratio = ratio/32768
            Serial.print("Temp2, ");
         Serial.println(max2.temperature(RNOMINAL,RREF));
   //Serial.print("Time2, "); Serial.println(currentMillis);

   currentMillis = millis(); //gets the current time (ms) since program started
   rtd = max3.readRTD();     //read RTD
   ratio = rtd;
   ratio /= 32768;          //ratio = ratio/32768
            Serial.print("Temp3, ");
         Serial.println(max3.temperature(RNOMINAL,RREF));
   //Serial.print("Time3, "); Serial.println(currentMillis);

   currentMillis = millis(); //gets the current time (ms) since program started
   rtd = max4.readRTD();     //read RTD
   ratio = rtd;
   ratio /= 32768;          //ratio = ratio/32768
```

```
            Serial.print("Temp4, ");
          Serial.println(max4.temperature(RNOMINAL,RREF));
  //Serial.print("Time4, "); Serial.println(currentMillis);

  currentMillis = millis(); //gets the current time (ms) since program started
  rtd = max5.readRTD();     //read RTD
  ratio = rtd;
  ratio /= 32768;           //ratio = ratio/32768
            Serial.print("Temp5, ");
          Serial.println(max5.temperature(RNOMINAL,RREF));
  //Serial.print("Time5, "); Serial.println(currentMillis);

 //conditions for initial states
  if (fb_rtd <= target - lower && state == 0) {
    state = 0;    //temperature <= lower limit in the beginning
  }
  else if (state == 0) {
    state = 1;    //temperature > lower limit on first ramp up
  }
  //conditions for post-initial states
  if (fb_rtd > target + upper) {
    state = 2;    //temperature >= upper limit
  }
  else if (fb_rtd <= target + upper && state == 2) {
    state = 3;    //approaching target from the top
  }
  else if (fb_rtd < target - lower && state == 3) {
    state = 4;    //temperature <= lower limit
  }
  else if (fb_rtd >= target - lower && state == 4) {
    state = 5;    //approaching target from the bottom
  }

 //Bang bang controller
  if (state == 0 || state == 3 || state == 4) {
    digitalWrite(relaypin, HIGH); //turns heater ON
  }
  else {
    digitalWrite(relaypin, LOW);  //turns heater OFF
  }
  //Serial.print("State, "); Serial.println(state);
  previousMillis = millis();      //reset variable to current time (ms)
 }
}
```